Measurement of $\sigma(p\bar{p} \rightarrow Z^0) \times$ BF ($Z^0 \rightarrow \tau\bar{\tau}$) at $\sqrt{s}$ =1.96 TeV using the DØ Detector at the Tevatron

Een wetenschappelijke proeve op het gebied
van de Natuurwetenschappen, Wiskunde en Informatica.

Proefschrift

ter verkrijging van de graad van doctor
aan de Katholieke Universiteit Nijmegen,
op gezag van de Rector Magnificus Prof. dr. C.W.P.M. Blom,
volgens besluit van het College van Decanen
in het openbaar te verdedigen
op donderdag 8 april 2004,
des namiddags om 1.30 uur precies

door

Silke Duensing

geboren op 4 oktober 1973 te Bremen (Duitsland).

Promotor:	Prof. Dr. S.J. de Jong	
Manuscriptcommissie:	Prof. Dr. G. Brooijmans	Columbia Univ.
	Prof. Dr. J. Conway	Rutgers Univ.
	Prof. Dr. M. W. J. M. Demarteau	Univ. of Amsterdam
	Dr. S. Muijs	NIKHEF
	Dr. S. Protopopescu	Brookhaven NL

ISBN: 90-9017458-3

Contents

Introduction **1**

1 Theory **3**
1.1 The Standard Model . . . 3
1.1.1 Particles . . . 3
1.1.2 Forces . . . 4
1.1.3 Mass . . . 5
1.2 Z^0 Boson Production at the Tevatron . . . 6
1.2.1 The Proton . . . 6
1.2.2 The τ Lepton . . . 8
1.2.3 The Z^0 Boson . . . 8
1.3 The Higgs Boson . . . 9
1.3.1 Production and Decay at the Tevatron . . . 10
1.4 Beyond the Standard Model . . . 11
1.4.1 Problems of the Standard Model . . . 11
1.4.2 Supersymmetry . . . 12

2 The Tevatron and the DØ Detector **15**
2.1 The Tevatron Accelerator . . . 15
2.1.1 Producing and (Pre-)Accelerating the Protons . . . 15
2.1.2 Main Injector and Anti-proton Production . . . 16
2.1.3 The Tevatron . . . 16
2.1.4 Accelerator Operation . . . 17
2.2 The DØ Detector . . . 17
2.2.1 The DØ Co-ordinate System . . . 18
2.2.2 The Inner Tracking Detectors . . . 19
2.2.3 Preshower Detectors . . . 22
2.2.4 Calorimeter . . . 23
2.2.5 Muon System . . . 27
2.2.6 Luminosity Counters . . . 29
2.3 Data Aquisition . . . 29
2.3.1 Level 1 Triggers . . . 29
2.3.2 Level 2 Triggers . . . 31
2.3.3 Level 3 Triggers . . . 32
2.4 Luminosity . . . 34

2.5 Monte Carlo Simulation 35

3 Event Reconstruction **39**
3.1 Charged Track Reconstruction 39
3.1.1 Vertex Reconstruction 41
3.2 Calorimeter Clusters 41
3.3 Jet Reconstruction 42
3.4 Missing E_T 43
3.5 Electrons and Photons 43
3.6 Muon Reconstruction 44
3.6.1 Local Muons 44
3.6.2 Global Muons 45
3.6.3 Calorimeter Muons 45
3.6.4 Muon Candidates 46
3.7 Reconstruction of Hadronic Decays of τ leptons 46
3.7.1 Calorimeter 47
3.7.2 Tracks 48
3.7.3 Classification of τ Types 50
3.7.4 Energy Scale and Resolution 50
3.7.5 Tau Identification Variables 54

4 Event Selection **59**
4.1 Data Set 59
4.1.1 Run Quality 60
4.2 Trigger Selection 60
4.3 Muon Identification 61
4.3.1 Muon Acceptance 61
4.3.2 Local Muon Reconstruction Efficiency 63
4.3.3 Muon Track Match Efficiency 64
4.3.4 Muon Trigger Efficiency 66
4.3.5 Timing Requirement 68
4.3.6 Summary of Muon Tagging Efficiencies 69
4.4 Tau Identification 69
4.4.1 Tau Acceptance 70
4.4.2 Tau Reconstruction Efficiency 71
4.4.3 Tau Track Matching 72
4.4.4 Drell-Yan Correction 73
4.4.5 $\pi \leftrightarrow \rho$ Confusion 73
4.4.6 Offline Tau Selection Efficiency 74
4.4.7 Tau Trigger Efficiency 77
4.4.8 Tau Reconstruction and Selection Summary 78
4.5 L3 Track Trigger Efficiency 79
4.6 Muon Isolation 80
4.7 Di-Muon Rejection 81
4.8 Cut Optimization 82

5 The $Z^0 \to \tau\bar{\tau}$ Cross Section **93**
5.1 Electron Contamination 93
5.2 Charge Mis-measurement 94
5.3 Background Estimate 95
5.3.1 Di-muon Events 95
5.3.2 W-pair and $t\bar{t}$ Events 96
5.3.3 QCD Events 97
5.3.4 W$\to \mu\nu_\mu$ Events 98
5.3.5 Background Summary 100
5.4 Properties of the Selected Events 100
5.5 Cross Section Measurement 103
5.5.1 Luminosity 103
5.5.2 Summary of Efficiencies and Backgrounds 103
5.6 Comparison to the SM and the $Z^0 \to \mu^-\mu^+$ and $Z^0 \to e^-e^+$ channels 108
5.7 Conclusion and Outlook 109

References **111**

Summary **117**

Samenvatting **119**

Introduction

Particle physics is an attempt to understand what matter is made of and what holds it together. Our picture of these questions is deeply interconnected with our understanding of the evolution of the universe to its final fate. The current answer to the first two questions is given by the "Standard Model" (SM) of particle physics. Unluckily - or luckily, depending on point of view, new cosmological results from measurements of the Cosmic Microwave Background [1] and measurements of Supernovae [2] indicate that the universe is flat (only) at this specific point in time and that only ≈5% of the matter consists of particles that are included in the Standard Model. More than ≥20% of the energy content of the universe takes the form of so-called "Dark Matter" for which there are a number of candidates. The largest fraction (>70%) of all gravitationally interacting "material" needed to make the universe we live in does not even seem to be made of matter; this contribution is called "Dark Energy".

This thesis concerns the understanding of the "matter" part of the universe. The Standard Model organizes the particles found to date in a "periodic table" and describes the interactions by three fundamental forces (electro-magnetism, the weak and strong force) which are transmitted by carrier-particles. Gravity plays an outside role here. Even though the particles contained in the SM make up only ≈5% of all "matter" of the universe, the matter and force we experience in daily life and "beyond" are described remarkably well.

The Standard Model is generally considered to be a manifestation of a more general theory and there are reasons to expect that hints of this general theory will appear at energies on the order of 1 TeV. This is the energy range the LHC is designed to explore. Before it becomes operational in 2007, the upgraded Tevatron with a center-of-mass energy of 1.96 TeV has the best opportunities to discover physics beyond the standard model. Even within the SM, there is room for discovery at the Tevatron: the particle connected to the origin of masses, the Higgs boson, remains elusive to date.

Tau leptons play an important role in discovery strategies of both new physics and the Higgs boson. But before one can use these particles to explore new territory, the challenging process of tau identification must be understood. A measurement of the $p\bar{p} \rightarrow Z^0$ cross section times the branching fraction of $Z^0 \rightarrow \tau\bar{\tau}$, shorthanded to ($Z^0 \rightarrow \tau\bar{\tau}$) cross section in the following, where the result can be compared to the Standard Model expectation, serves this purpose.

This thesis will begin with a brief description of the elementary particles and forces described by the Standard Model, followed by the Higgs model of the generation of mass. The components of the title of this thesis will then be explored: The production of Z^0-bosons at the Tevatron will be described, including a short description of the effect of the initial state compositeness. The tau lepton and its decays are subsequently introduced. The experimental apparatus,

the upgraded DØ detector at the Tevatron, and Monte Carlo simulation of the data is presented in chapter 2. Chapter 3 discusses the path from the raw data collected with the DØ detector, to physics objects that correspond to the building blocks of matter as just introduced in this chapter. Chapter 4 describes the selection of $Z^0 \to \tau\overline{\tau}$ candidate events and discusses the efficiency of this selection. The measurement of the cross section of the Z boson decaying into tau leptons is discussed in chapter 5. These results will be compared to the prediction of the Standard Model and to recent measurements of the $Z^0 \to \mu^-\mu^+$ and $Z^0 \to e^-e^+$ cross sections at the same energy.

Chapter 1

Theory

The power and problems of the Standard Model (SM) have an analogy in chemistry: the periodic table ordered the known elements considering their properties. From "holes" in this table, elements with certain properties could be predicted. But it was only after the rise of quantum mechanics that the chemical properties of the elements could be predicted from their electronic orbitals, hence explaining the particular form of the periodic table. In particles physics, the zoo of known particles is explained by a small number of "elementary" particles that are ordered in generations by increasing mass. But how many generations exist and why the masses of the particles are what they are is not explained within the SM. To find a theory that explains everything is the final dream of particle physics.

The current picture of the building blocks of matter and their interactions will be presented first. This is followed by a discussion of the process measured in this thesis, the production of Z bosons at the Tevatron using its decay into tau leptons. In the next section, the search at the Tevatron for the only SM particle not yet experimentally observed, the Higgs boson, is presented with a brief discussion of the role tau leptons play. This chapter will conclude with a discussion of some remaining problems of the Standard Model and one possible solution that highlights the role of tau leptons for the discovery potential for "New Physics" at the Tevatron.

1.1 The Standard Model

1.1.1 Particles

The first discovery of a particle that is still considered elementary was Thomson's discovery of the electron about a century ago. Together with the nuclei, electrons form atoms. The nuclei are compound systems of protons and neutrons which in turn are made of quarks each. Quarks have a charge equal to $\pm 1/3$ or $\pm 2/3$ the elementary charge (the charge of a proton or 1.6×10^{-19} C), the system of uud in the ground state is a proton with a charge of +1, and the ground state of udd is a neutron with a charge of 0. The discovery of the composite nature of the proton and neutron was made only in the second half of the 20^{th} century. This is due to the fact that the quarks are subject to the strong force which prevents us from seeing individual free quarks at low energies. Results of deep inelastic scattering experiments at SLAC were explained using a picture of nucleons having a substructure, analogous to the discovery of nuclei by Rutherford.

The particle we now know as doublet partner of the electron, the electron-neutrino, was first introduced as a hypothetical particle to explain the energy spectrum of electrons in weak beta decay.
These four particles, the u and d quarks together with the electron and electron-neutrino are the building blocks of the matter that surrounds us. Elementary particles which are not among the usual constituents of that matter were first found in cosmic rays, notably the muon. Similarly, in the 1950's mesons (kaons) with unexpected ("strange") behavior, i.e. large production cross section but slow decay, were found. These mesons are now known to have a "strange (s)" quark as one of their constituents. The weak isospin partner of this quark, the charm (c), was discovered in the 1970's, only shortly before the first particle of the third generation, the tau-lepton was discovered by Perl *et.al.* at SLAC [3]. With the latest discoveries of the top-quark at the Tevatron [4, 5] in 1995 and the tau neutrino with the DONUT experiment [6] in 2001, also at Fermilab, all particles of the third generation have now been found.
All spin 1/2 fermions found to date are ordered in three families with repeating quantum numbers. This is shown in Table 1.1. The quantum numbers given in the last two columns are important for the understanding of the interactions of the elementary particles. There is evidence that there are only these three families which will be discussed later in section 1.1.2.

	family				
	1	2	3	Q	I_3
quarks	u	c	t	+ 2/3	+ 1/2
	d	s	b	- 1/3	- 1/2
leptons	ν_e	ν_μ	ν_τ	0	+ 1/2
	e	μ	τ	1	- 1/2

Table 1.1: The fermions of the Standard Model.

1.1.2 Forces

Particles can be viewed as excitations of relativistic quantum fields. Global symmetry transformations give rise to conserved quantities (Noether-theorem). Requiring that the theory be invariant under local symmetry transformations gives rise to fields corresponding to the fundamental forces of nature. This principle, called *local gauge invariance* can be used to describe forces, that have vastly different appearances (electromagnetic, weak, strong) in a mathematically consistent way. Each field identified with a force has carrier particles with spin 1. The bosons carrying the four fundamental interactions are: the photon for the electromagnetic force, the W and Z^0 bosons for the weak force, eight gluons carrying the strong force and gravitons transmitting gravity. The latter, gravitons, have spin 2 and have not been experimentally confirmed. Table 1.2 lists the particles carrying the fundamental interactions.

Gravity plays an outside role in the Standard Model since a relativistic quantum field theory of gravity remains an unsolved problem to date. On the scale of fundamental forces, the strength of gravity is many orders of magnitude weaker than any of the other three forces and can thus be neglected at the energies of current experiments. The scale where gravity would come into play is called the Planck scale and is about 10^{19} GeV.

force	boson
electroweak	γ, Z^0, $W^{\pm}$
strong	g^a, a=1...8
gravity	G

Table 1.2: Carrier particles of interactions.

Requiring the Lagrangian to be invariant under local transformations generated by the U(1) group leads to the need for a new interaction field. The force transmitted by this field is the electromagnetic force and the theory is called Quantum Electro Dynamics (QED). This theory is one of the most precisely tested and successful theories in physics. In order to explain the four fermion interaction (Fermi-interaction) in weak decays, a theory based on the groups SU(2)×U(1)$_Y$ was developed [7, 8, 9, 10, 11, 12]. The three bosons arising from the invariance under SU(2) transformations are the $W_{1,2,3}$ bosons. $W_{1,2}$ mix to form the charged W bosons that are responsible for weak decays. The remaining W_3 boson does not appear in nature as such. Its superpositions with the boson of the U(1)$_Y$ group are the physical photon and Z^0 boson. The weak interactions (exchange of W-bosons) violate parity maximally. Right handed fermions are only subject to the forces corresponding to the U(1)$_Y$ group, i.e. the physical fields of the photon and the Z^0-boson. As neutrinos have no electric charge, right handed (massless) neutrinos do not take part in any interactions.

The theory describing the strong force, called Quantum Chromodynamics (QCD), is based on the SU(3) group. Quarks have one more degree of freedom than leptons. This new degree of freedom is called *color* and can take three different values. The bosons of the SU(3) group, called gluons, are themselves carriers of color charge. In contrast to electroweak interactions, the strong force gets stronger on larger scales. As a consequence, free colored particles can never appear in nature. Quarks form color-neutral objects, either mesons consisting of a quark and an anti-quark (having a color and its anti-color, thus being color-neutral) or baryons made out of three quarks (red, blue and green, thus adding up to a color-neutral state). If a $q\bar{q}$ pair is pulled apart, the energy contained in the color-field between the two particles increases linearly with distance. At a given point, the energy of the field exceeds the energy needed to produce a new $q\bar{q}$ pair, and the "string" splits forming two new mesons. In the regime where the coupling parameter of the strong theory is large, perturbation theory cannot be used for calculations and phenomenological models must be used to describe processes like the hadronization of quarks produced in an $e\bar{e}$ or $q\bar{q}$ annihilation. In the limit of small scales or large energies, the strength of the strong force decreases (asymptotic freedom) and perturbative methods can be used to describe the effects of the strong interaction.

1.1.3 Mass

The bosons in the electroweak theory as presented above are massless. However, the experimentally observed W and Z^0 [13, 14, 15, 16] are rather heavy (O(100) GeV). If these bosons were massless, the electromagnetic and weak force would be of similar strength at low energy. The mechanism of breaking this symmetry (*electroweak symmetry breaking*) gives mass to the weak bosons. In the framework of the Standard Model this is achieved through the Higgs mechanism [17, 18]. A complex doublet of scalar fields with four degrees of freedom exhibiting SU(2)$_L$

symmetry is introduced. These scalar fields allow for a potential with a non-trivial minimum. Hence the ground state of this Higgs field has a non-zero expectation value and the choice of a ground state breaks the symmetry. The value of the vacuum expectation value v is 246 GeV and sets the scale for electroweak symmetry breaking. Two of the four degrees of freedom give masses to the two charged W bosons. Giving the Z^0 mass by absorbing a third degree of freedom while keeping the photon massless introduces a relation between the Z^0 and W masses which has been tested experimentally. The remaining degree of freedom is associated with a new particle, the Higgs boson. The masses of the fermions in the SM are introduced as couplings to the Higgs field. The only free parameters in the Standard Model is the mass of the Higgs boson which remains elusive but holds the key to experimental verification of the Higgs mechanism.

1.2 Z^0 Boson Production at the Tevatron

In a $p\bar{p}$ collider like the Tevatron the colliding particles are composite. If two of the constituents of the proton and anti-protons respectively undergo a *hard scattering* process, particles with high transverse momenta are produced. Most of these interactions involve only the strong interaction where leptons are produced scarcely. Thus, the appearance of leptons in an event signifies an interesting interaction. One of these processes can be the production of electroweak bosons which decay into leptons. At the energy of the upgraded Tevatron of 1.96 TeV, the main production mechanism of the Z^0 boson is the annihilation of a quark and an anti-quark. This process and Z^0 production processes of second order are illustrated in Fig.1.1. In Fig.1.1(c) the gluon in the initial state splits into a $q\bar{q}$ pair, one of which participates in the Z^0 production process and the remaining quark leads to a jet. The probability of the processes in Fig.1.1 depends on the momentum distribution of quarks and gluons in the proton. These distributions are given by the parton density functions (pdfs) which will be briefly discussed in the following section 1.2.1 after which short summaries of the Z^0 boson and τ lepton properties are given.

1.2.1 The Proton

The suggestion that the proton is a composite particle of three quarks was made in 1964 on spectroscopic grounds by Gell-Mann and Zweig [19, 20, 21]. In 1969, Feynman extended that idea to a picture of the proton as a collection of many quarks and anti-quarks (which he called partons), where the number of quarks exceeds the number of anti-quarks by three [22]. Gluons were introduced with quantum-chromo-dynamics (QCD) in 1972 [23, 24, 25, 26].
The quark-parton model assumes that non-interacting particles are confined inside the proton, and this idea was corroborated by the asymptotic freedom found in non-Abelian gauge theories such as QCD. The probability to find a quark q with a momentum fraction between x and $x+\mathrm{d}x$ is given by $\mathrm{q}(x)\mathrm{d}x$, where $\mathrm{q}(x)$ denotes the quark density function. The parton density functions for the quarks $\mathrm{q}(x)$ and gluons g(x) must fulfill two conditions: the total number of quarks must add up to the quantum number of the nucleon and the momenta of all partons must add up to the total momentum of the proton (*momentum sum rule*).

As mentioned in the introduction, the interactions of quarks and gluons are described by QCD. In this theory, the proton becomes a dynamic system rather than the static object of the

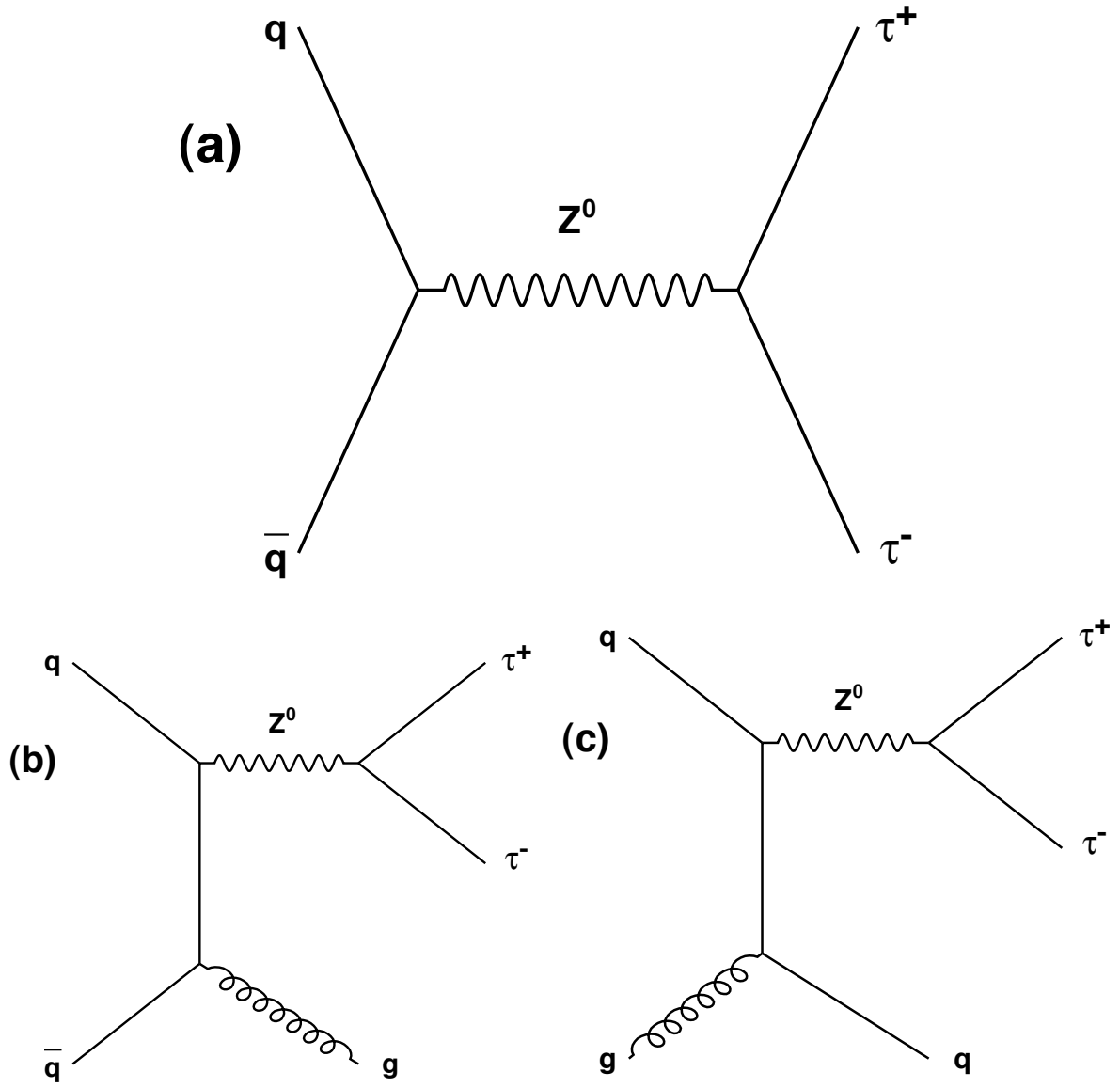

Figure 1.1: Feynman diagrams showing the leading order process (a) and two higher order processes in (b) and (c).

quark model. Depending on the energy scale of the probe, the number of quarks and gluons at a certain momentum fraction of the proton changes, e.g. the higher the wavelength of the probing photon, the more partons can be resolved. The probability of a quark to split into a gluon and a quark with the momentum fraction x and the similar contribution from gluon splitting can be calculated in QCD and are given by

$$P_{q\to q}(x) = \frac{4}{3}\frac{1+x^2}{1-x}, \qquad P_{g\to q}(x) = \frac{1}{2}\left(x^2 + (1-x)^2\right). \tag{1.1}$$

The necessary modifications to the quark-parton model introduce *scaling violations*, meaning that the parton distributions now depend on the momentum transfer of the interaction Q^2. The

set of coupled equations describing this dependence is called DGLAP (Dokschitzer Gribov-Lipatov Altarelli-Parisi) equations [27, 28, 29].

As pointed out above, the momentum distribution of the partons inside of the proton plays an important role in calculating the cross sections and kinematics of electroweak processes at hadron colliders. Different parton density functions result in varying kinematic properties and cross sections of the electroweak bosons produced [30]. For the precise measurement of electroweak processes at the Tevatron, the systematic uncertainty due to the error on the parton density function must be known. The most precise measurements of the parton density function are performed at the electron proton collider HERA at DESY. These measurements are explained in detail in [31]. The most frequently used pdf models are the CTEQ [32] and MRST [33] sets. At DØ, the CTEQ5 set is the current standard. For the analysis presented here, the systematic uncertainties introduced by the modeling of the detector response and the statistical error on the measurement will be much larger that the uncertainty due to the parton density functions.

1.2.2 The τ Lepton

The τ lepton has a relatively large mass of 1.77 GeV, allowing it to decay not only into the much lighter electron and muon but also into hadronic final states containing a small number of pions and kaons. The fact that taus can decay into both electrons and muons led to its discovery in 1975 by Perl *et.al.* at SLAC [3]. Events with both an electron and a muon were observed. The apparent lepton number violation led to the realization that a new particle had been produced.

The most important final states of the tau decay together with their branching fractions are given in Table 1.3. The branching fraction of the most important $Z^0 \to \tau\bar{\tau}$ final states can be found on the right hand side of Table 1.3.

τ decay channel	BF in %
ν_τ eν_e	17.8
ν_τ $\mu\nu_\mu$	17.4
ν_τ $\pi^\pm$	11.1
ν_τ $\pi^\pm + n\,\pi^0$	36.9
ν_τ $3\,\pi^\pm$	10.0
ν_τ $3\,\pi^\pm + n\,\pi^0$	5.2

$Z^0 \to \tau\bar{\tau}$ decay channel	BF in %
ee $\nu_\tau\bar{\nu}_\tau\nu_e\bar{\nu}_e$	3.2
$\mu\mu$ $\nu_\tau\bar{\nu}_\tau\nu_\mu\bar{\nu}_\mu$	3.0
eμ $\nu_\tau\bar{\nu}_\tau\nu_\mu\bar{\nu}_e$	6.2
had e $\nu_\tau\bar{\nu}_\tau$	23.0
had μ $\nu_\tau\bar{\nu}_\tau$	22.5
had had $\nu_\tau\bar{\nu}_\tau$	42

Table 1.3: The branching fractions of the most common τ decays (left) and the final state signatures of Z^0 production followed by Z^0 decay into a τ-pair (right). The abbreviation "had" stands for any combination of hadrons. The addition number of π^0's n is meant to be one or more in the relevant entries in the table.

1.2.3 The Z^0 Boson

The Z^0 boson has a mass of 91.188±0.002 GeV and a decay width of 2.495±0.002 GeV. This is the sum of all partial decays widths, which can be calculated from the vector and axial vector couplings of the fermions to the Z^0. The mass, width and partial decay widths of the Z^0 boson

have been measured with great precision at LEP [34]. The quoted values are taken from this reference. The invisible Z^0 decay width can be determined from the line shape of the Z^0-peak in the $q\bar{q}$ and the three lepton channels e^-e^+, $\mu^-\mu^+$and $\tau^-\tau^+$. Using the width of the decay into a given neutrino flavor as calculated from theory, the number of lepton families with neutrinos of a mass below half the Z^0-mass was measured to be 2.984±0.008 [34].

The production of a τ-pair from $q\bar{q}$ annihilation can go through an intermediate state of a photon or Z^0 boson. The total di-tau production cross section is the square of the matrix elements of both terms. The photon-term falls off with $1/s$, with s being the center of mass energy, while the Z^0 term gives a large resonant contribution at $\sqrt{s} \approx M_Z$. Figure 1.2(a) shows MC distributions of the full interference structure and the Z^0 boson exchange alone. The distribu-

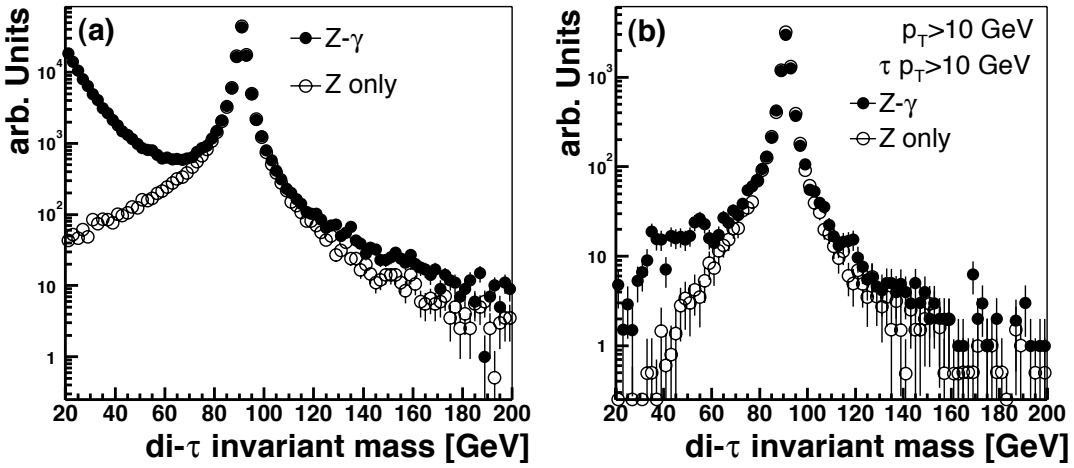

Figure 1.2: The di-tau invariant mass of the full γ-Z^0 interference structure and the Z^0 boson contribution alone from Monte Carlo simulation. (b) shows the same variable after requiring one of the tau decays products to be a muon above 10 GeV.

tions of the di-tau invariant mass is dominated by the Z^0 exchange in the region of the Z^0 peak. For low di-tau invariant masses, the photon exchange plays the most important role. Requiring the transverse momenta of the visible tau decay daughters to be above 10 GeV, the events are dominated by the Z^0exchange. This is shown in Fig.1.2(b).

1.3 The Higgs Boson

In the Standard Model, the only remaining unmeasured parameters are the mass, decays width and couplings of the Higgs boson, which to date remains elusive. Theoretical bounds from unitarity constraints in W scattering require that the Higgs boson has a mass below 1 TeV. This limit is not only true for the Standard Model Higgs, but also for the lightest Higgs in extensions of the Standard Model.

Indirect constraints on the mass of the Higgs boson can be inferred from measurements of the W and Z^0 boson masses, since the Higgs boson contributes to the effective boson masses through loop corrections. Fits to all electroweak measurements place an upper limit on the

Higgs mass of 193 GeV/c^2 at 95% confidence level [35]. Noticeable corrections due to top quark loops, that are quadratic in the top mass, make the improvement of the top mass measurement an important goal. In addition to the top mass, the W-mass measurement should also gain precision in current and new experiments. These improved W and top mass measurements will thus improve the indirect Higgs mass measurement. The physics program is not restricted to tightening the indirect constraints on the Higgs mass, direct searches of the Higgs will be performed as well. If the Higgs is experimentally observed, the comparison of the direct and indirect measurements of its mass provide an important consistency check of the SM. The current lower bound on the Higgs mass is set at 114.4 GeV/c^2 at 95% confidence level by the LEP experiments [36].

There are two mass ranges of particular interest, as discussed in [37]:

- $m_{h_{SM}} < 130$ GeV
- 150 GeV $< m_{h_{SM}} < 180$ GeV.

The second mass range is special in the sense that the Standard Model with a Higgs boson in this range would be consistent up to the Planck energy scale. The first mass range is preferred in the minimal supersymmetric model (see section 1.4.2).

1.3.1 Production and Decay at the Tevatron

The two main Higgs production mechanisms in $p\bar{p}$ collisions at 1.96 TeV are gluon-gluon fusion and associated production of Higgs with a Z^0 or W boson. The cross sections of these processes as a function of the Higgs mass are shown in Fig.1.3(a). Though the cross section for gluon fusion is higher than that for the associated production, the channels considered in the search strategies for Run II, that are laid out in detail in [37], use only associated production where the leptonic decays of the W and Z^0 facilitate background rejection and trigger acceptance.

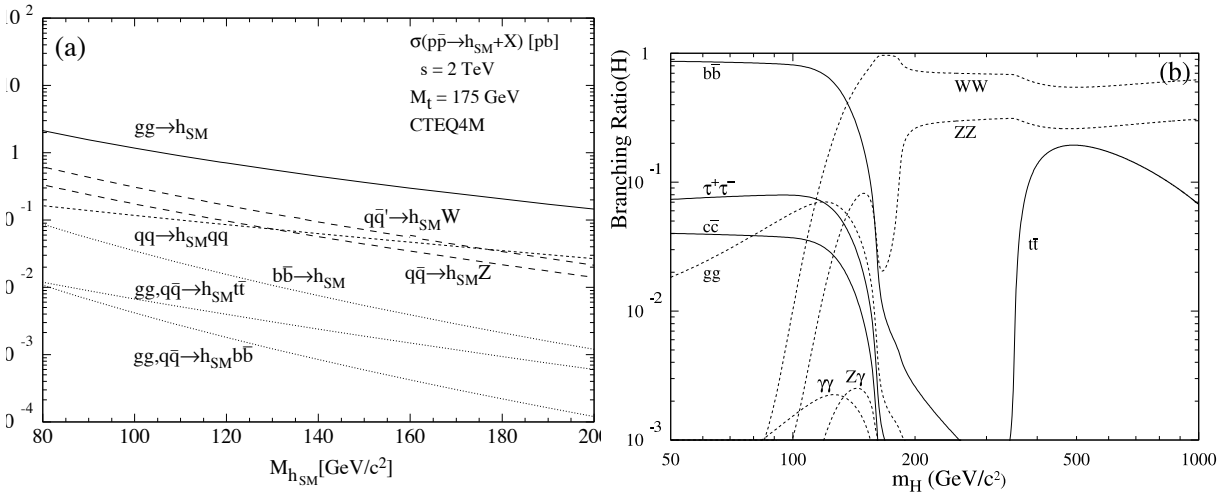

Figure 1.3: (a) shows the cross section of the main Higgs production processes versus the Higgs mass. (b) shows the branching fraction of the Standard Model Higgs boson as a function of the Higgs mass.

The branching ratios of the decay channels of the Standard Model Higgs are shown in Fig.1.3(b). For Higgs masses below the W-pair threshold, about 90% of all Higgs bosons decay into b quarks. The large background to $b\bar{b}$ production from QCD processes makes associated production the preferred channel, employing the events where the electroweak boson decays into leptons.
The background from QCD events is much lower in Higgs to di-tau events. In this case, the gluon-gluon fusion process can profitably be used for a Higgs search. The presence of a Higgs boson would appear as a higher rate of high invariant mass di-tau events than expected from γ/Z^0 production only. If the resolution of the reconstructed taus and the missing transverse mass (which corresponds to the momentum sum of the neutrinos) is sufficient, the Higgs events would create a second peak in the di-tau invariant mass spectrum in addition to the Z^0. Thus is further motivation to study $Z^0 \rightarrow \tau\bar{\tau}$ decays.

1.4 Beyond the Standard Model

The Standard Model of particle physics is a very successful theory that has survived each of the high precision tests it has been subjected to. However, it provides no explanation as to why there are three generations of fermions and several forces with different strengths. In addition, the particular masses of the fermions have no underlying explanation. This leads to the belief that the Standard Model is just a manifestation of a more fundamental theory which is only valid at low energies, in analogy to Newton's theory of gravity as a valid special case of general relativity. Here, we will discuss a number of the problems with the Standard Model and briefly describe Supersymmetry, one of the ideas that addresses some of the limitations of the SM model.

1.4.1 Problems of the Standard Model

Not only do the masses of the fermions have to be added to the Standard Model by hand, the Higgs mechanism for electroweak symmetry breaking (EWSB) is not predicted by the SM. The three forces in the SM correspond to three symmetry groups: SU(2) and U(1) for the electroweak interactions and SU(3) for the strong force. Each of these forces has a coupling parameter. Due to higher order effects, the coupling strength is not a constant, but depends on the energy scale. If this "running" of the coupling strength is extrapolated to high energies, the coupling strengths appear to unite at a scale of $M_{\mathrm{GUT}} \approx 10^{16}$ GeV, where GUT stands for "Grand Unified Theory". It should be noted that the three coupling parameters fail to converge in one point in the SM. The question why the scale of this convergence is so much higher than the W mass of 10^2 GeV is called the "hierarchy" problem.

A second serious problem is the fact that the Higgs boson, because it is massive, has a self-interaction. This diagram gives rise to non-renormalizable divergences when calculating the Higgs mass by integrating this diagram over all momenta. One possibility to deal with this divergence is a cut-off at some energy scale, M_X, where new physics appears. This scale is likely near the GUT scale M_{GUT}. The running of the Higgs mass from this scale M_X down to the weak scale M_{W} is given by:

$$M_{\mathrm{H}}^2(M_{\mathrm{W}}) = M_{\mathrm{H}}^2(M_X) - C_g^2 M_X^2, \tag{1.2}$$

where C_g is a dimensionless constant and $M_X >> M_{\mathrm{W}}$. In order for this approximate equality to hold, the terms on the right hand side must cancel to a very high precision at all orders of the perturbation series. This is very unnatural and is called the "fine tuning problem".

One possible solution to this problem is a theory in which the Higgs is a composite particle. This family of theories is called Technicolor. In order to accommodate fermion masses, new "techni" generations of fermions have to be postulated. None of the particles predicted by these theories have been found to date. Other serious constraints for this type of theory arise from the observed suppression of flavor changing neutral currents and electroweak precision data that are sensitive to virtual techni-particles. A similar idea is "compositeness" where all currently known particles are assumed to consist of smaller particles called preons. This theory is also constrained by the absence of expected deviations from hard scattering between preons.

The most promising model which addresses the fine tuning problem is Supersymmetry (SUSY) which will be briefly described below. For a more detailed introduction of SUSY, the reader is referred to the literature [38].

1.4.2 Supersymmetry

Let us return to the fine tuning problem stated in equation 1.2. The radiative corrections come from loops of all particles with strengths proportional to the mass of the particle in the loop. The largest contribution thus comes from the top loop. Since bosonic and fermionic loop contributions are of opposite sign, the one-loop correction takes the form

$$\delta M_{\mathrm{H}}^2(M_{\mathrm{W}}) \simeq O(\frac{\alpha}{\pi})(m_B^2 - m_F^2). \tag{1.3}$$

If one postulates bosonic partners B of about the same mass for each Fermion F, the total correction to the Higgs mass remains small naturally. This symmetry between fermions and bosonic particles is called "Supersymmetry" (SUSY).
In the relativistic limit, the spins of particles and their supersymmetric partners differ by half a unit. The superpartners of the SM leptons ℓ with spin 1/2 are "sleptons" $\tilde{\ell}$ with spin 0. The partners of the gluons g with spin 1 are "gluinos" $\tilde{\mathrm{g}}$ of spin 1/2. All quantum numbers with the exception of the spin are the same for particle and superpartner. Hence no pair of Standard Model particles can form such a multiplet: all partners are "new" particles. To cite from [38]: "Supersymmetry economizes on principle, not on particles".

One of the features of supersymmetric theories is the fact that the renormalization group equations for the running of the coupling strengths now lead to a unification in a single point as predicted by GUTs provided that the sparticle masses are of the order of 1 TeV.

If supersymmetry were not broken, a large number of sparticles would already have been observed. The LEP exclusion limit for sparticles mass clearly show that e.g. $m_{\mathrm{e}} \neq m_{\tilde{\mathrm{e}}}$. There is not a single model for SUSY breaking, but for a number of reasons, spontaneous local SUSY breaking is preferred over the introduction of explicit SUSY breaking terms on a global mechanism. Supergravity naturally appears in local SUSY breaking models [38], and using the renormalization group evolution of the SUSY breaking parameters one finds that the squark and slepton masses increase while the Higgs mass squared can become negative, which triggers electroweak

symmetry breaking. If 60 GeV< m_t <200 GeV, these equations predict a W mass of the order of 100 GeV.

Each fermion of spin 1/2 has both a left- and a right-handed chiral degree of freedom. Each of these components has a superpartner of spin 0 to create an equal number of fermionic and bosonic degrees of freedom. These two superpartners have different weak isospin and mix. The 2×2 mass matrix has off diagonal terms which lead to a mass splitting between the two sfermion states which is roughly proportional to the mass of the fermion and $\tan\beta$ for the charged leptons and down type quarks. Hence the $\tilde{\tau_1}$ is potentially a relatively light sparticle.

There are Supersymmetry scenarios with different SUSY breaking mechanisms, and for each scenario, there are a number of unknown parameters. The number of parameters can range from more than 100 in general models to five in "Minimal" SUSY models. This naturally results in a large number of different signatures for Supersymmetry at high energy colliders. Before the start of Run II, working groups have studied the SUSY discovery prospects with an extensive survey of the signatures at the Tevatron [39, 40].

Motivated by the definition of the Supersymmetry transformation, one can define a quantity called *R*-parity:

$$R \equiv (-1)^{3B+L+2S}, \tag{1.4}$$

where B is the baryon number of a particle, L its lepton numbers and S the spin. With this, R is +1 for all particles of the SM and -1 for all superpartners. Though SUSY terms that violate R parity can be added to the superpotential, in most models *R*-parity conservation is assumed. In this case, sparticles can only be produced in pairs and they decay to lighter supersymmetric particles and their SM partners. At the end of the decay chain, we have (two) lightest SUSY particles (LSP) and a number of SM particles. The LSPs cannot decay further and produces a signature with missing energy in the detector. These LSPs are candidates for cold dark matter in the universe.

In one of the simplest SUSY models that incorporates the SM, the minimal supergravity model (mSUGRA) [41], there are five parameters:

$$m_0, m_{1/2}, A_0, \tan\beta, sign(\mu),$$

where $m_0/m_{1/2}$ are the GUT unification values of the soft SUSY breaking fermionic/bosonic mass parameters, A_0 is the GUT unification value of the soft SUSY breaking trilinear scalar coupling parameters, $\tan\beta$ is the ration of the Higgs field vacuum expectation values and $sign(\mu)$ is the Higgs superfield parameter.

It has been noted that cosmological measurements put constraints on SUSY models [42]. One region in the mSUGRA parameter space that is compatible with the recent WMAP measurements of the cosmic background radiation, LEP measurements and the $b \to s\gamma$ branching fraction measured by CLEO[43] predicts signatures that can be observed at the upgraded Tevatron. In this region, the so-called "hyperbolic branch/focus point" region, charginos $\tilde{\chi^{\pm}}$ and neutralios $\tilde{\chi^0}$, which are superpositions of the supersymmetric partners of the bosons, are expected to be light, and an important process for discovery is:

$$p\bar{p} \to \tilde{\chi_1^{\pm}}\tilde{\chi_2^0} X, \tag{1.5}$$

The cleanest sample of events result when the partners of the $\tilde{\chi}_1^{\pm}$ and $\tilde{\chi}_2^0$ decay into leptons. These events have three leptons in the final state and hence are called “tri-lepton” events. For scenarios with large tanβ, the decay into tau leptons is favored over electrons and muons, stressing the importance of tau leptons as tools for search for this type of physics “beyond the Standard Model”.

Chapter 2

The Tevatron and the DØ Detector

The Tevatron, situated at the Fermi National Accelerator Laboratory, is currently the world's highest energy accelerator, with a center of mass energy of 1.96 TeV. It is a storage ring in which protons and anti-protons circulate in opposite directions and are brought into collision at two points, the B0 and D0 experimental areas. In these areas, two general purpose detectors, CDF and DØ respectively, measure the collision products.
During the years 1989-1996, collisions took place at a center-of-mass (CMS) energy of 1.8 TeV, and the analysis of this data led to the discovery of the top-quark. This data taking period is referred to as Run I. The construction of the DØ detector followed the CDF detector in time and was optimized for the measurements of jets, electrons, photons and muons over a large range in pseudo-rapidity, $\eta = -\ln(\tan\frac{\theta}{2})$. To minimize showering and multiple scattering in front of the calorimeter, the Run I DØ detector did not have a magnet inside the calorimeter and thus lacked a momentum measurement by the inner tracker. In the current DØ detector, a solenoid has been added along with upgrades to many other parts of the detector. The data taking period that started in 2001 with the upgraded Tevatron is referred to as Tevatron Run II.

2.1 The Tevatron Accelerator

The Tevatron is filled with beams of high energy protons and anti-protons in a series of steps shown schematically in Fig.2.1. This process, and the chain of accelerators required are outlined below.

2.1.1 Producing and (Pre-)Accelerating the Protons

In the pre-accelerator, negatively charged hydrogen atoms are brought up to an energy of 750 keV using a Cockroft-Walton accelerator. From there, the ions are bunched and further accelerated by the LINAC until they reach an energy of 400 MeV. The H^- ions are led into the booster, a circular accelerator which raises the proton energy to 8 GeV. In the booster the H^- ions are stripped off their electrons and protons (p^+) remain.

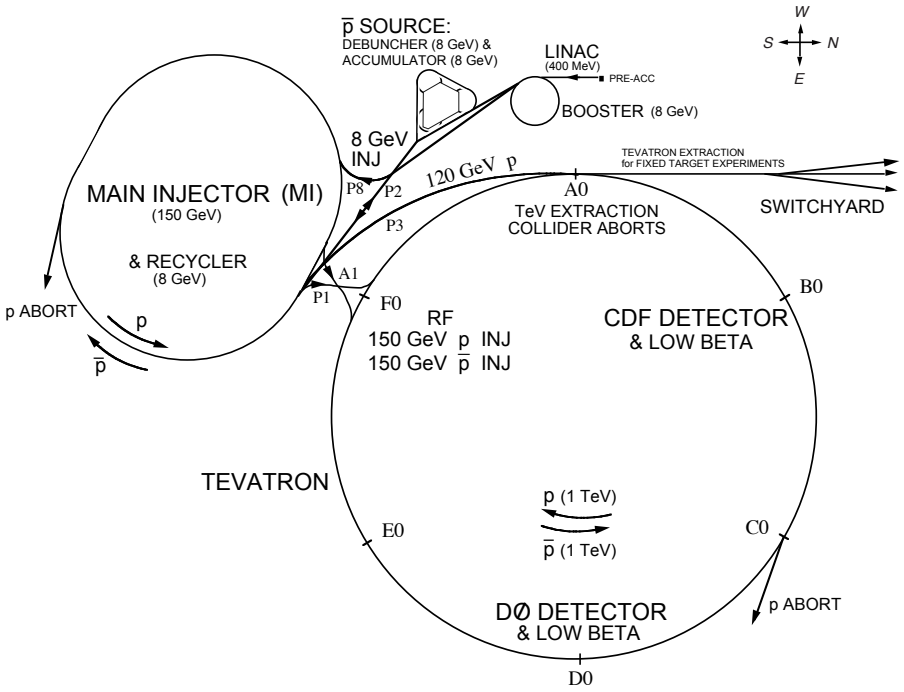

Figure 2.1: Layout of the Fermilab accelerator chain.

2.1.2 Main Injector and Anti-proton Production

The main injector receives the 8 GeV protons from the booster and subjects them to two possible fates: the protons are either accelerated up to an energy of 150 GeV for transfer to the Tevatron, or their energy is increased to 120 GeV and they are transferred to the $\overline{\text{p}}$-source. The 120 GeV protons collide with a nickel target, and in these events many secondary particles are produced. In approximately one out of every 10^5 collisions, an anti-proton is produced. The anti-protons are temporarily stored in the accumulator until enough ($\approx 10^{11}$) have been collected to fill the Tevatron. The accumulator uses stochastic cooling [44] to reduce the emittance of the beam. Stochastic cooling is based on the principle of sampling a particle's motion with a pickup and correcting the motion with a kicker. These anti-protons are then bunched and inserted into the Main Injector. There they are accelerated to an energy of 150 GeV for insertion into the Tevatron.

2.1.3 The Tevatron

The Tevatron receives proton and anti-proton bunches at an energy of 150 GeV from the Main Injector and accelerates them to their final energy of 0.98 TeV. To keep the particles on their circular path of radius $\approx$1 km, superconducting magnets with a strength of 4.2 Tesla are used. The protons travel clockwise, and the anti-protons counter-clockwise. These beams are brought into collision at two interaction points: B0, where the CDF detector was built and D0, the location of the other multi purpose detector DØ, named after its interaction point.

2.1.4 Accelerator Operation

Store preparation for the Tevatron typically takes an hour. The luminosity then slowly decays over the course of a store which usually lasts 12-20 hours. During this time, the anti-protons for the next store are accumulated. The instantaneous and integrated luminosity for a typical good day of running, showing the end of a store, preparation for a new store and data taking with the new store, are displayed in Fig. 2.2.

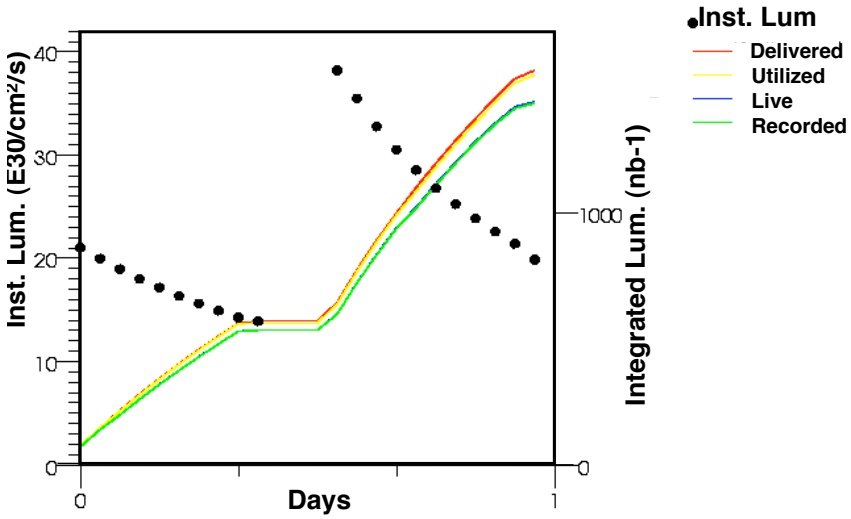

Figure 2.2: The instantaneous and integrated luminosity of a typical day (May, 8th 2003).

2.2 The DØ Detector

Designs of multi purpose detectors like the DØ detector have a common blueprint illustrated in Fig.2.3. Following a particle (e.g. a muon) on its path after production in the primary interaction, the first detectors encountered are devices making precise measurements of the particle position along its path, using the least possible material to keep multiple scattering and energy loss to a minimum. In most modern detectors, the innermost detectors are made of the semiconducting material silicon. Still being relatively expensive, these devices are usually followed by another large-volume tracking system. In the case of the DØ detector, the available space is dictated by the calorimeter and the newly added solenoid magnet. The chosen technology uses scintillating fibers read out by visible light photon counters, VLPCs. This entire tracking volume is immersed in a 2 Tesla magnetic field in the direction of the beam line, allowing for measurement of the momentum. The particle crosses the magnet upon leaving the tracking volume. To precisely measure the particle's position after the multiple scattering caused by passage through the solenoid, so-called "preshower" detectors have been added. These detectors also provide an energy measurement that helps correct for early showering particles in the preceding material. The calorimeter that follows stops the particle with an absorber and measures its energy. Only muons and neutrinos can completely penetrate this detector and the muons are measured with another tracking detector outside of the calorimeter, for that reason called muon chambers.

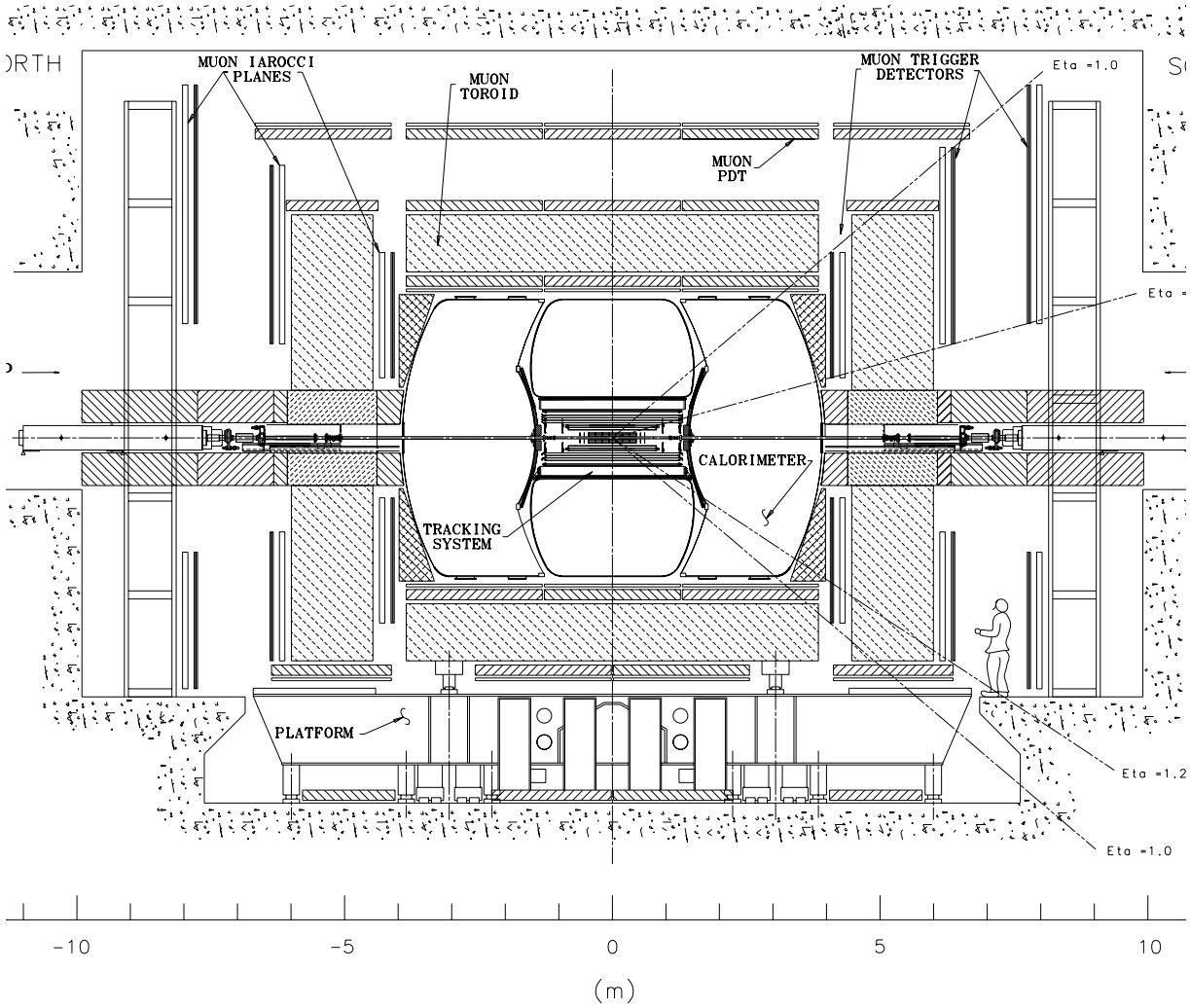

Figure 2.3: A cross section view in the *y*-*z* plane of the DØ detector.

The different sub-detectors of the DØ experiment will be described hereafter, following an introduction of the DØ co-ordinate system and some important kinematic variables in collider physics.

2.2.1 The DØ Co-ordinate System

In the DØ detector, a right handed co-ordinate system is used. The direction of the proton beam is defined as the positive *z*-axis, with the *y*-axis pointing upwards. The polar angle $\theta = 0$ coincides with the positive *z*-axis, and the azimuthal angle $\phi = 0$ with the positive *x*-axis, pointing away from the center of the Tevatron ring.
In $p\bar{p}$ machines, one can use the image that two "bags" of elementary particles (quarks, anti-quarks and gluons) collide. One is usually interested in events where two of these elementary particles undergo a so-called "hard-scattering" interaction, where their annihilation produces new particles at high transverse momentum. The center-of-mass system (CMS) of this hard interaction usually has a boost along the *z*-axis. Many of the particles produced in the collision,

i.e the remnants of the proton not participating in the hard-scattering interaction, escape down the beam pipe. Hence the longitudinal boost of the CMS of the hard scattering partons cannot be measured. The transverse momentum p_T of the particles that escape down the beam pipe is negligible, making it possible to apply the conservation of energy and momentum in the transverse plane. This makes the transverse energy/momentum E_T/p_T ($E\sin\theta/p\sin\theta$) and the missing transverse energy $\not\!\!E_T$, defined as the transverse energy imbalance, extensively used variables for hadron collider physics. It is natural to use the rapidity y at hadron colliders as the multiplicity of high energy particles (dN/dy) is covariant under Lorentz transformation along the z axis. The rapidity is defined as:

$$y = \frac{1}{2}\ln\left(\frac{E + p_z}{E - p_z}\right). \tag{2.1}$$

For highly boosted particles, where $m/E \rightarrow 0$, this can be approximated by

$$\eta = -\ln\left(\tan\frac{\theta}{2}\right). \tag{2.2}$$

Differences in rapidity are invariant under Lorentz boosts in the z-direction. The pseudorapidity η calculated using the origin (0,0,0) and a z-position at the relevant detector (e.g. muon A-layer) is referred to as η_{det}, in contrast to η_{phys} which uses the θ angle of the particle. Unless stated otherwise, η is to be understood as η_{phys}.

2.2.2 The Inner Tracking Detectors

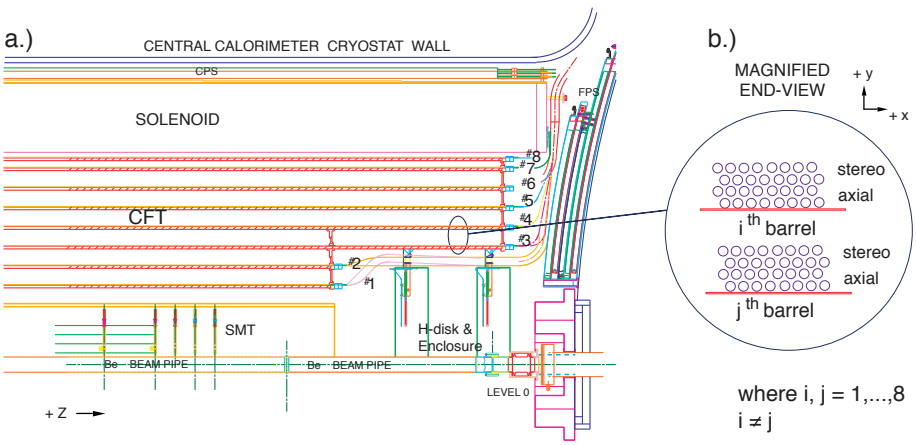

Figure 2.4: a) shows a quarter view of the inner tracking detectors. A close up of the CFT layer structure is shown in b).

A one-quarter view of the upgraded DØ inner tracking detector is shown in Fig.2.4. The Run II central tracker is built inside a 2 T solenoid magnet with a mean radius of 60 cm, which enables the measurement of the transverse momenta of the charged particles. The magnet is a two layer coil, made of superconducting material, and has a thickness corresponding to approximately one radiation length. Lead shimming on the solenoid provides for a uniform thickness

in radiation lengths over the rapidity coverage of the solenoid. The current density is higher at the ends of the solenoid to ensure good field uniformity. The tracking detectors inside of the solenoid are a silicon microstrip detector (SMT) enclosed in turn by the central scintillating fiber tracker (CFT).

The Silicon Microstrip Detector

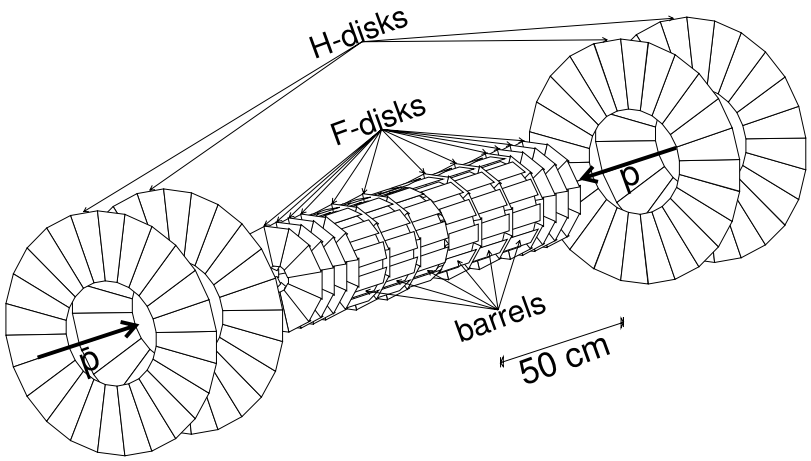

Figure 2.5: The SMT tracker, showing the outer barrel layers as well as the F-disks and H-disks.

The design of the DØ Silicon Microstrip Tracker (SMT) with a barrel and disk structure as shown in Fig. 2.5 was chosen to optimize the tracking efficiency of particles over a large range in η and over a large spread in vertex position z.
The six barrels consist of eight layers, which are organized in doublet layers as four super-layers. The layers have equal spacing with an inner radius of 2.5 cm and an outer radius of 10 cm. The silicon wafers used in the SMT are of n-type and 300 μm thick. All wafers have strips with 50 μm pitch along the beam direction for a measurement of the $r-\phi$ co-ordinate. Except for the sensors of layer 1 and 3 of the outermost barrels, all sensors are doublesided. That is, they have both axial and stereo readout. In super-layers 1 and 3, the pitch of the 90°stereo readout is 156 μm. The remaining super-layers 2 and 4 have a stereo angle of 2° with a pitch of 62.5 μm.

The second major structure of the SMT are the F-disks. There are 12 F-disks, made of 12 wedges each. Each wedge has strips at a pitch of 50 μm, parallel to one edge of the detector and on the other side strips at 62.5 μm pitch, parallel to the other edge. Hence, these strips have a stereo angle of 30°. The combination of strips allows for a measurement of both $r-\phi$ and $r-z$ co-ordinates. An F-disk is associated with each barrel and three more disks are placed beyond each end of the barrel detector. Furthest out are the H disks, which are made of two single sided layers of silicon glued back-to-back with a ± 7.5° stereo angle and a strip pitch of 80 μm. The active region of the H disks extends from 9.6 cm $< r <$ 23.6 cm, at z positions of ±92.5 and ±128.5 cm from the detector center.

The silicon detector modules attach to bulkheads made of beryllium which servesvia both as support and provide cooling via flow of a water ethylene-glycol mixture through integrated tubes. Beryllium was chosen as material as it combines a long radiation length with rigidity. In

total, the SMT detector comprises 793,000 read-out channels. To control radiation damage to the detectors, they are actively cooled with a coolant at -8° C at the inlet to the detector.

Radiation Monitoring

The double sided silicon detectors used for most of the SMT are rather susceptible to radiation damage that effectively changes the doping concentration [45]. To measure the radiation level and integrated dose of radiation received by the silicon detectors, the silicon radiation monitoring system was added to the design of the DØ detector. It consists of two subsystems, one using Beam Loss Monitors (BLMs) [46], as are also being used at CDF and the Tevatron, and a system using silicon diodes on small modules, called 'fingers', located on the outermost F and H disks [47].

- the BLM
  The Beam Loss Monitors (BLMs) are ion chambers with two cylindrical, concentric electrodes with an active volume of 100 cm^3 filled with argon. They are located immediately outside of the calorimeter, inside the muon shielding, at 160 cm away from the interaction point. On each side of the detector, four BLMs are located at a radius of 12 cm from the beam center at 0°, 90°, 180° and 270° in ϕ. The electrodes are supplied with a high voltage of 2000 V for a fast response. The sensitivity of the BLMs is 70 nC/rad.
  They are read out using logarithmic amplifier cards to provide sensitivity to a wide dynamic range of currents. This signal is sent to CAMAC modules where the signal is digitized at about 10 times the beam revolution frequency. The data are read out in real time and compared to the alarm and abort levels, and are also stored for 2000 events in a FIFO buffer. In case the FIFO receives a beam abort signal, it stops downloading new data 10 ms after the abort was received and the data is written out to a file. In addition to the radiation rate, modules in the CAMAC crate also calculate the radiation dose as a rolling sum. The dose is read out at a rate of 5 kHz and is scaled using a look-up table. The radiation sum is also linked to an alarm in the DØ control room indicating excessive exposure to radiation. The logarithmic amplifiers are optimal calibrated for medium to high signals. Because the ratiation level is rather low during normal running, the information obtained by the BLM is not very accurate. In addition, the system is located far away from the silicon detector, the detector most sensitive to radiation. These shortcomings are addressed by the Silicon Diode Radiation Monitoring System.

- Silicon Diode Radiation Monitoring System
  To acquire information about the radiation dose the silicon detectors have received, it is best to measure it near the detectors due to difficulties in incorporating non-linear effects caused e.g. at injection of the beams or scraping. For the DØ silicon detector, a system consisting of silicon diodes has been designed to conduct this measurement [47]. The silicon diodes with an active area of 8×8 mm^2 are from test structures from the H-disk wafers with guard rings that allow depletion voltages above 400 V before breakdown, and thus guarantee that these diodes will survive longer than the silicon strip detectors. Two diodes each are placed on 24 so-called "fingers". Six of these "fingers" are placed on each of the four outermost F- and H-disks. The radii of the two diodes are similar to the radii of the innermost and outermost barrel layer. Hence the diode system provides the full ϕ and r coverage of the SMT. The diodes are fully depleted, and particles crossing

the active volume create an electric signal which is proportional to the number of crossing particles, e.g. to the received radiation dose. The finger are mounted on beryllium plates to ensure good thermal contact to the SMT cooling ring. A flat flex cable provides the necessary inputs to the diodes on each finger and also contains the pre-amplifying electronics. To ensure a large dynamic range, the pre-amplification is performed in two channels with different gains. The signal is sent to receiver cards in a custom made crate via low mass cables followed by heavily shielded special made cables. The receiver cards contain amplifiers and shapers that prepare the signal for the readout by the ADCs. Subsequent electronic differentiation and integration provides a baseline correction for slowly varying currents. The ADC data is unreliable at lower doses due to electronics noise, but sensitivity to doses as low as single minimum ionizing particles is provided by a system using VME scalers and counters.

The data acquisition program runs on a Motorola Power PC [48] under the VxWorks [49] operating system. The use of interrupts ensures the correct timing of the readout. The fast readout, that can later be used to make abort decisions, is sampled at 5 kHz and written to a circular buffer. The slow readouts are sent to the EPICS system [50] at 10 Hz, which makes them available to the online control system and to the Tevatron. The scalars are read out at 1 Hz. The actual dose is calculated by the data acquisition program which uses the data from high and low gain ADC channels as well as the scalars. The gain channel most sensitive to the measured radiation level is used, in the overlap ranges the two readings are averaged. The radiation dose information is made available to a graphical user interface (GUI) in the DØ control room. The integrated dose, calculated from the instantaneous dose and the time difference between successive readings, as well as data received from the BLM system are displayed in the same GUI [51]. The system is designed to provide abort information based on the fast readout of the silicon diodes. In the case of an abort, a 10 s history of the fast readout radiation doses will be written out as a file. The abort feature has as of yet not been used.

Central Fiber Tracker

The Central Fiber Tracker (CFT) [52] consists of 32 concentric layers of scintillating fibers. The layers are arranged in eight barrels, each consisting of two doublet layers, one with *zu* and one with *zv* configuration (z is an axial layer, u, v have a stereo angle of $\pm 3^\circ$). This can be seen in the close-up of two barrels shown in Fig. 2.4 b). In total, the CFT comprises 76800 fibers. Each fiber has a diameter of 835 μm and is double clad to improve light yield. A wave guide is matched to every channel to transport the signal to the Visible Light Photon Counters (VLPCs) which are solid state photon detectors based on silicon diodes with an operating temperature of 9 K. Their fast rise time, high gain of 50,000 electrons per converted photon and high quantum efficiency of 85% make them ideally suited for this application, for which they were specifically developed [53].

2.2.3 Preshower Detectors

The main purpose of the preshower detector is to enhance electron and photon identification and to improve the calorimetric measurement by sampling the shower multiplicity after the material

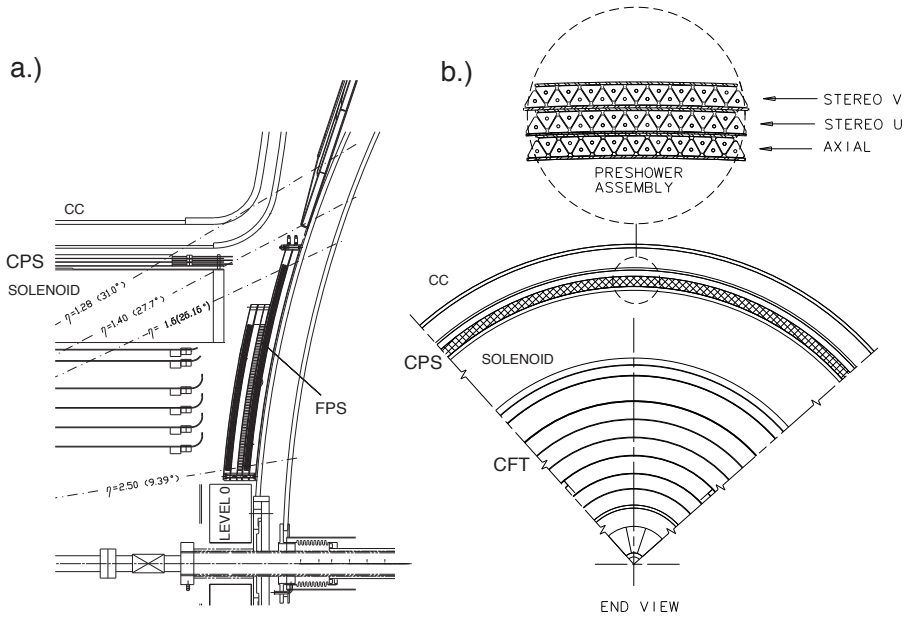

Figure 2.6: a) The location of the preshower detectors CPS and FPS with their coverage in η in $r-z$ view. b) An $r-\phi$ view of the CPS with a close-up showing the three layers of triangular shaped scintillating fibers.

of the solenoid. Both the central preshower detector (CPS) [54] with a coverage of $|\eta|$ <1.3 and the forward detector (FPS) [55], covering 1.5< $|\eta|$ <2.5, are made of layers of triangular shaped scintillators. Wavelength shifting fibers embedded in the center of the triangles pass the signal to VLPCs, following the same readout chain as the central fiber tracker. The coverage of both preshower detectors and the layer structure of the central preshower detector are shown in Fig. 2.6. The central preshower detector consists of three layers of scintillators: an inner axial layer and two layers at a stereo angle of ±22.5°. The forward preshower detector has two stereo layers over the full coverage, and an additional inner doublet layer following a $2X_0$ lead absorber for $|\eta|$ >1.65. The u and v layers have an angle of 22.5°. The inner layer acts as detector for minimum ionizing particles. For rapidity values between 1.5 and 1.65, the particles shower in the solenoid, upstream of the preshower detectors.
Due to the triangular shape of the fibers, the distance traversed in a strip has a linear dependence to the incident position. This is convenient for the calculation of the cluster position using a charge weighted mean of the strip centers. The position resolution of a doublet (two layers are hit) for minimum ionizing particles has been measured in a cosmic ray setup to be 550 μm [56].

2.2.4 Calorimeter

The DØ calorimeter uses liquid argon as active medium and has a hermetic coverage to $|\eta| < 4$. It consists of three cryostats of nearly equal size, the central calorimeter (CC) and the two endcap calorimeters (EC). The innermost four layers of the calorimeter form the electromagnetic (EM) section. The absorber in this section is depleted uranium with a thickness of 3-4 mm per layer. Hence the total radiation length of the EM calorimeter is 20 X_0. The following layers form the

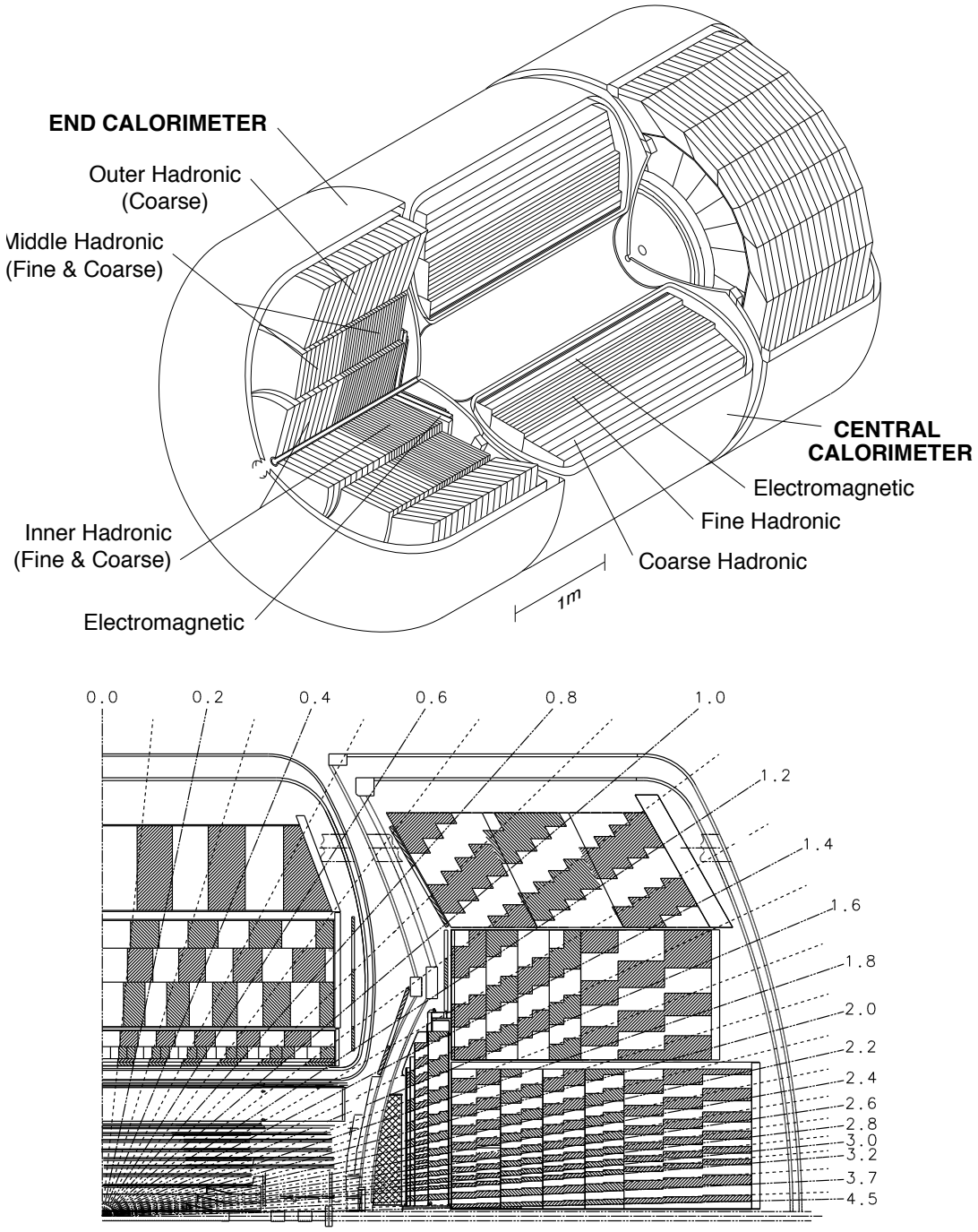

Figure 2.7: Top: a cut-away view of the DØ calorimeter, bottom: Quarter view in $r - z$ of the detector, showing its geometry in more detail.

Fine Hadronic (FH) calorimeter. It consists of three layers of depleted uranium in the central cryostat and four in the endcaps. The outermost layers use stainless steel and copper as absorber and are called the Coarse Hadronic (CH) calorimeter. While the central calorimeter has only one CH layer, there are up to three layers in the endcap calorimeters. The layer structure of the

calorimeter is depicted in Fig.2.7 (top). The material of the calorimeter corresponds to 2 nuclear interaction lengths (λ) in the Fine Hadronic section, and 5-7 λ for the CH calorimeter. Figure 2.7(bottom) shows the segmentation into single readout cells. The size of these cells determines the position resolution that can be achieved with the calorimeter. Most layers are segmented into readout cells of 0.1 in η and ϕ. The third EM layer is at the expected shower maximum for electrons and photons and has a segmentation four times as fine (0.05×0.05 in $\eta \times \phi$). For $|\eta|$ values above 2.7, these cells have a size of 0.1×0.1. For all layers at $|\eta|$ >3.2, the cell size increases to 0.2×0.2.

Calorimeter Readout and Calibration

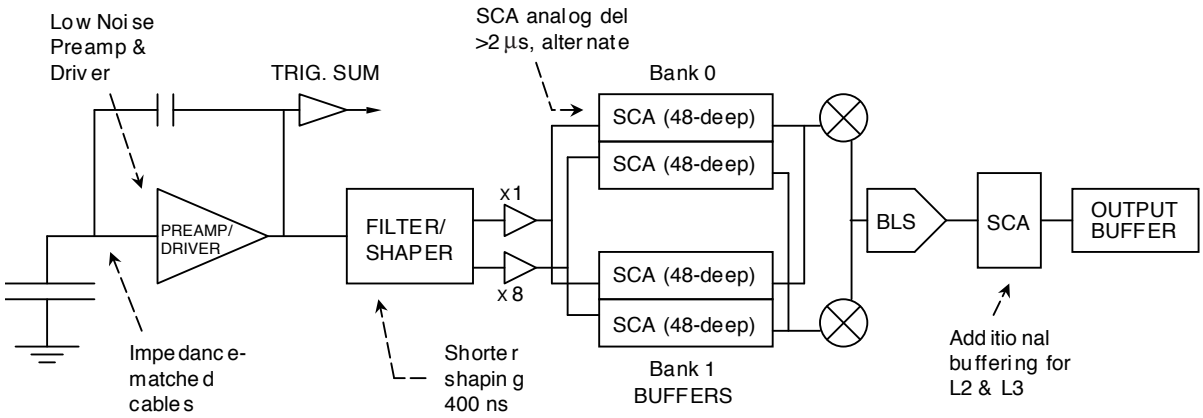

Figure 2.8: A schematic illustration of the calorimeter readout.

The calorimeter readout electronics is sketched in Fig.2.8. A charge, proportional to the energy loss of particles when traversing the calorimeter readout cell is sent to the readout electronics via coaxial cables. The charge is integrated in the preamplifier, producing a signal proportional to the charge flowing into the preamplifier loop. Here, a fast trigger signal is produced, while the signal for the precise energy measurement is shaped with 400 ns. The shaped signal is readout every 132 ns and the samples are stored in Switched Capacitor Arrays (SCA) for about 4 μs until the L1 trigger decision is received. Upon a positive decision, the Base Line Subtracter (BLS) sends the signal of the event in question to a second SCA buffer where it is stored until the trigger decision of level 2 is received. Finally, the signal is sent to an ADC. The SCA chips store two gain paths (×1 and ×8) separately. The two paths are needed to achieve 15 bit resolution with the use of 12 bit ADCs. This precision is matched to the precision of the SCAs. The BLS boards are used to subtract the signal from interactions before the event of interest. The BLS subtracts the sample from 3x132 ns ago from the sample at nominal peak time.
For detail of the calorimeter readout electronics, consider references [57] for an overview of the Run II calorimeter upgrades and [58] for details of the calorimeter electronics.

Non-linearities

For the purpose of calibrating the read-out, a pulser system has been built. A 18-bit DCA applies a DC current to an inductance, and this signal is injected into the calorimeter readout just outside of the cryostat. To first approximation, the ADC response to the DCA calibration is linear, as shown on the left plot of Fig.2.9. The right figure shows the residuals of the readout to the linear fit. In both plots you can see the saturation for large signal and a non-linear response for low signals. The measurements of the non-linearities in the response of the DØ calorimeter are described in detail in reference [59]. To correct for the non-linearities, the following parametrizaton is used

$$u_8(v) = gav + \epsilon(gav), \qquad u_1(v) = av + 8\epsilon(av/8),$$

where ϵ is a universal function fitted to all channels. v is the DCA signal injected into the readout channel, which is assumed to be linear with an offset. The real numbers g and a may be different for each readout channel.
Not taking the non-linearities of the energy response for low signals into account leads to measureable effects. Applying the correction to the $Z^0 \rightarrow ee$ peak shifts the peak from 83.7±0.6 GeV to 89.4±0.6. Another effect is that jets appear narrower than expected without taking the non-linearities into account. The jet width, calculated using a formula where the distances to the jet center are weighted by the transverse energy, will underestimate the contribution of the low-energy cells at the edge of the jet cone as their energy is underestimated.
The calorimeter is read out in "zero-suppressed" mode. This means that only channels above a threshold value are read out. For most of the data taken, the online threshold has been set at the pedestal value plus 1.5 the pedestal widths ("1.5σ"). This raised the amount of noisy cells to a value that could not be tolerated by currently used jet finding algorithms. Hence a higher threshold of the pedestal value plus 2.5σ was used to select the calorimeter cells used in offline reconstruction. The combined effect of the non-linearities of the electronics response, stemming from the SCAs, and the zero suppression enhances the effect of "narrow" jets. As the ADC response of a low energy cell is lower than expected for linear behaviour, these cells are suppressed more often than predicted in models not accounting for the non-linearities. Hence, jets look narrower than expected. Implementing the true response of the electronics combined with a realistic model of the noise is crucial for Monte Carlo Simulations if one is interested in calorimeter based objects.

Intercryostat Detector

The regions in between the central and endcap cryostats from $0.8 < |\eta| < 1.4$ contain a large amount of uninstrumented material, such as the cryostat walls and support structures. This leads to a degradation of the energy measurement in this region. The Intercryostat Detector (ICD)[60] partly restores the energy resolution by providing an additional sampling in this region. It consists of a single layer of 384 scintillating tiles with a size of 0.1×0.1 in $\eta \times \phi$, matching the cell size of the calorimeter. The signal is collected by wavelength shifting fibers imbedded in the tiles and transmitted using clear fiber waveguides to the photomultiplier tubes located outside of the magnetic field.

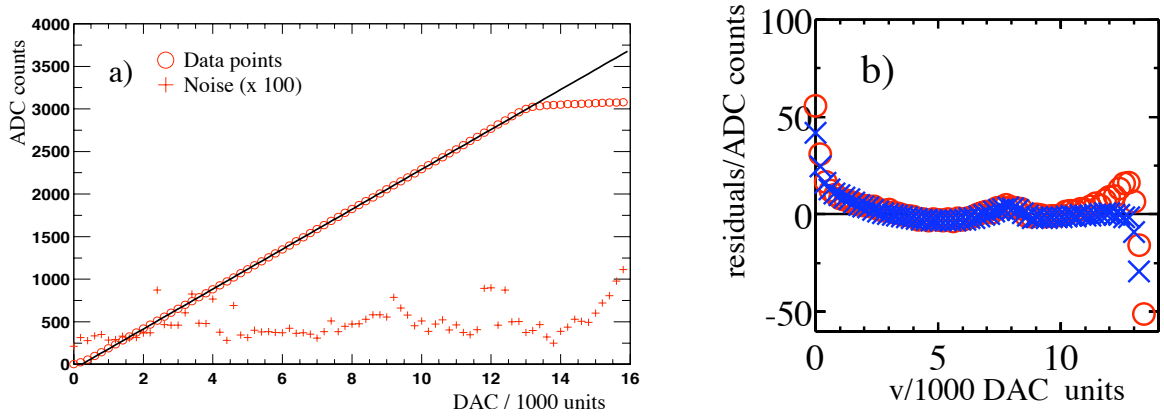

Figure 2.9: a) ADC response to the calibration signal (DAC). The noise multiplied by 100 is indicated by crosses. Left: Residual of data with respect to a straight line fit for a cell in the electromagnetic calorimeter, circles are ×1 gain, crosses the ×8 gain channel.

2.2.5 Muon System

The only easily observable particles produced in the primary interactions that traverse large amounts of material are muons. At multi-GeV energies their main interaction with material is via ionization. They behave as minimum ionizing particles, leaving a typical signature in the calorimeter. To reach the muon detector outside of the DØ calorimeter, particles must traverse 7-9 interaction lengths, with the toroid adding another 1-2 interaction lengths before the outermost muon chambers. This reduces the leakage of very high energetic jets into the muon system to a negligible level.

The muon system consists of three layers made of drift tubes (called A, B and C, from the inside out). The coverage of the system extends to a pseudo-rapidity $|\eta|$ of 2, split into three regions at $|\eta|$=1 called north, central and south. The layer structure and separation into the forward and central system is illustrated on the left of Fig. 2.10.
The drift chambers are filled with gas that is ionized by the passage of a charged particle. The charge is collected on high voltage sense-wires running through the volume. The central system uses Proportional Drift Tubes (PDTs). An example of such a cell is shown on the right of Fig.2.10. The sense wires run parallel to the magnetic field lines of the toriod. Two neighboring wires are joined at one end and read out at the others. The drift distance in the cells, corresponding to the z co-ordinate, can be measured with an accuracy of 0.5 mm. Relative timing information at both ends allows the determination of the hit co-ordinate along the wire (corresponding to ϕ). The resolution degrades for hits close to the readout electronics and ranges from 10 cm in the center to about 50 cm at the edges of the detector. The coverage of the central muon system in the A layer has a hole from ϕ from 225° to 310° to allow for the calorimeter support structure.

The forward muon systems suffers from higher radiation than the central system, due to its proximity to the beam. As detectors from the type used in the central system would not survive the expected background of Run II in the forward direction, another technique, the so called

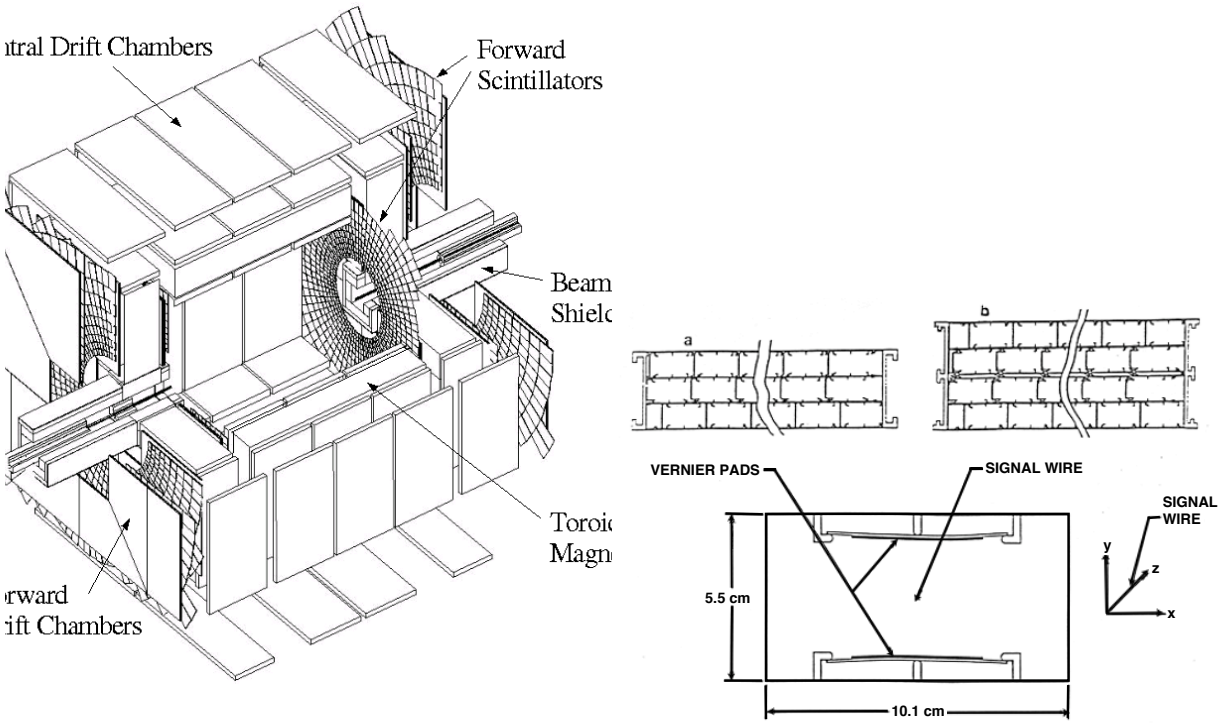

Figure 2.10: Left: Cut-away view of the DØ muon detector. Right: Drift cell of the central muon system.

mini-drift tube (MDT), was chosen. These drift tubes have a cross section of one by one cm, each holding a sense wire. The tubes run perpendicular to the beam, along the edge of the forward muon chambers. The drift distance measurements have a precision of 0.7 mm. As the drift tubes are only read out on one side, a measurement of the hit position along the wire is not possible. Shielding between the beam pipe and the forward muon chambers was added to reduce noise caused by muons accompanying the beam, beam remnants and hadrons escaping the calorimeter.

Both the forward and central system have four layers of drift detectors in the innermost (A) layer, and three layers for the B and C layer. Muons with enough energy to cross the whole muon system leave three track segments, one inside and two outside of the toroid. The trajectory of the charged particle is bent in the magnetic field produced by the toroidal magnet which averages 16.55 and 16.02 kG in the central and forward muon system, respectively [61]. The measurement of the track's curvature provides a measurement of its momentum.

Two layers of scintillator are added inside the A-layer (A-Phi layer) and outside of the C-layer (cosmic cap). In the forward region, all three layers of muon chambers are covered with a layer of scintillator pixels that cover a surface of 4.5 °in ϕ and 0.1 in η. For the forward system, this is the only measurement of the hit co-ordinate along the sense wire. The fast signal from the scintillator carries timing information and is read out in gates of 15 ns for trigger information

and 80-100 ns for the signal readout.

2.2.6 Luminosity Counters

The luminosity counters situated between the end-cap calorimeters and the forward preshower detectors (see Fig.2.6) at $z \approx \pm 140$ cm consist of 24 wedges of scintillator read out by photo-multipliers . The coverage extends from 2.7 to 4.4 in $|\eta|$. The crossing time of charged particles is measured with a resolution of $\approx$ 0.3 ns or 9 cm in z on both the proton and anti-proton side [62]. The FastZ modules use these inputs for a crude estimate of the z-position of the interaction vertex ("fast-z") with an uncertainty of 6.25 cm [63]. The modules measuring the z-position of the interaction set gates to distinguish luminosity and halos from the proton or anti-proton beam. The luminosity and two halo numbers numbers and the "fast-z" position are passed to the level 1 trigger framework (see the following section 2.3.1). The calculation of the luminosity will be explained in section 2.4.

2.3 Data Aquisition

The interaction rate at the Tevatron is 1.7 MHz, which is orders of magnitude higher than events can be readout, reconstructed and stored. The task of the trigger system is to reduce this rate by evaluating events and deciding whether they are interesting or if they can be discarded. The DØ trigger system consists of three levels, at which decisions based on increasingly complex information about the interaction can be made. Level 1 (L1) and Level 2 (L2) are hardware based systems while the Level 3 filters (L3) are faster and less precise versions of the offline reconstruction code. In total, the rate of 1.7 MHz is reduced to 50 Hz. If a trigger does not reject a high enough fraction of events and would lead to an unacceptable rate of events being written to tape, it gets "pre-scaled". This means it is only allowed to accept a fraction of passing events, where this fraction is determined by the prescale factor. In general, the prescale factors are adapted to the instanteneous luminosity to keep as many interesting events as possible while keeping the total rate to tape approximately constant.
A schematic view of the trigger system at L1 and L2 is shown in Fig.2.11. All three trigger levels will be briefly discussed in the following subsections, with special emphasis on the triggers of importance for the analysis presented in this thesis.

2.3.1 Level 1 Triggers

L1 decisions are based on the fast readout of the muon system, the calorimeter and, in a later period, the fiber tracker and preshower detectors which are combined in the central track trigger (CTT). Calorimeter towers and tracks in the muon system or central tracker, which are consistent with coming from electrons, muon, taus or jets and combinations thereof are so-called L1 And/Or terms. Based on the presence of the L1 And/Or terms, the event is discarded or sent for further evaluation to Level 2.

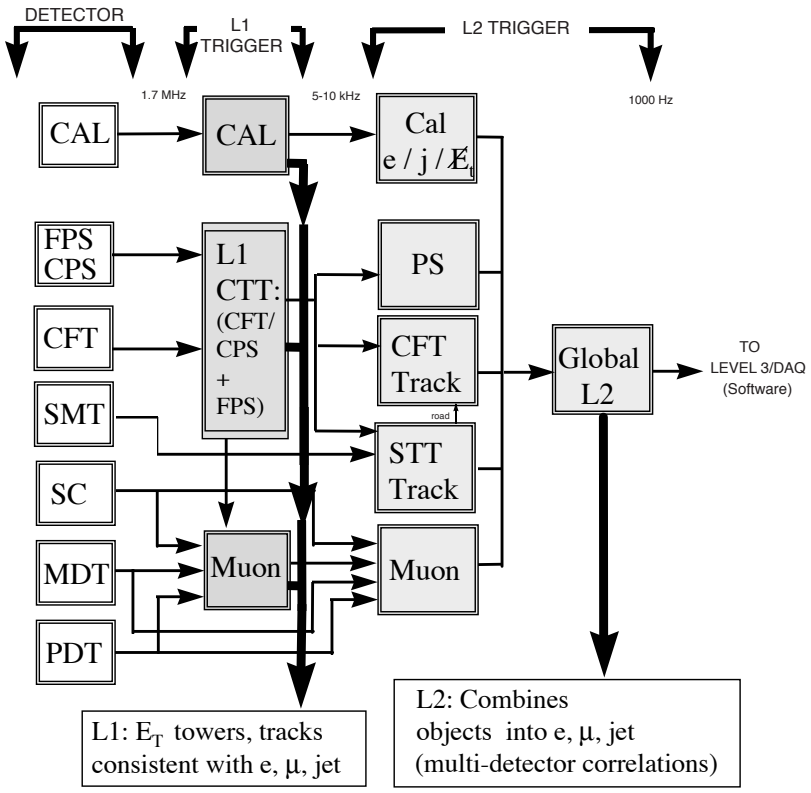

Figure 2.11: Structure of the first two trigger levels at DØ

.

The Trigger Framework

The trigger framework is a hardware trigger system that filters the 1.7 MHz beam crossing rate with a design output rate of 10 kHz. L1 trigger subsystems process detector specific information and deliver input terms, called L1 And/Or terms, to the trigger framework. Both "And" and "Or" combinations of these hardware And/Or terms, called "pseudo" And/Or terms, are added to the list of And/Or terms. Taking the readiness of the data acquisition system into account, the decision is taken to reject the event or keep it for evaluation at the L2 trigger. The pipelined trigger decision is made with a fixed latency of 3.3 μs. The number of specific trigger subsystem terms at L1 is 128, which can be combined to 256 And/Or terms [64]. The event is accepted if any of the 256 And/Or terms fire. As Fig.2.11 shows, all detectors except for the SMT deliver information to the L1 trigger framework. For the data period considered here, only the muon and calorimeter triggers were active.

L1 Muon Triggers

The L1 muon trigger combines wire hits with scintillator readout to build muon trigger objects that are sent to the L1 trigger framework. Muon trigger objects at L1 are based on a co-incidence of hits in scintillating pixels in two layers of the muon system. The muon system is divided into the central and forward region and eight octants in ϕ. Two scintillator hits have to come from

the same region and octant to fire the L1 muon trigger. To reduce the number of cosmic muons, hits are used only if their time is consistent with the hypothesis that the muon was from a $p\bar{p}$ interaction. This trigger gate is set at 15 ns. In later data taking periods L1 muon triggers were activated, where wire hits were added to the scintillator only terms.
Upon availability of the L1 track trigger, scintillator hits will be matched to central tracks to form trigger muons. The track match will reduce the fake rate and four different p_T thresholds will be used to further reduce accept rates of muon triggers, thereby avoiding the use of prescale factors.

L1 Calorimeter Trigger

At L1, four calorimeter towers are combined into a trigger tower of size 0.2×0.2 in $\eta \times \phi$. The energy is readout for two depth sections: the electromagnetic layers are combined, as are the fine hadronic layers. The coarse hadronic layers typicaly generate too much noise at L1 to be included in the trigger. The calorimeter L1 trigger terms are of the form CEM(x,y) and CJT(x,y) where x is the number of tower above a transverse energy threshold of y GeV. CEM is the readout of the energy deposited in the electromagnetic section, CJT is the total transverse energy of the electromagnetic and fine hadronic layers combined in the tower. The energy readout at L1 is lower than the energy of the precision readout used offline. This effect is enhanced for the hadronic energy, leading to the so-called EM-bias in the trigger efficiencies.

Tau triggers

Due to the non-availability of the track trigger at L1 for the data taking period considered, a dedicated trigger for hadronic taus at that level is impossible. Non-tau objects in events with tau leptons have to satisfy trigger requirements at L1 and L2, and only at L3 taus become trigger objects. In the case of a Z^0 decay into tau leptons, this necessitates a final state where at least one of the taus decays into a lepton. For events passing electron or muon triggers at the first two trigger levels, the tau tool is run and used for decision making at Level 3.

L1 Track Trigger

The L1 track trigger (CTT)[65] has inputs from the axial fibers of the central fiber tracker and the central preshower as well as the forward preshower fibers. The trigger is divided into 4.5° wedges in ϕ. Hit fibers within a wedge are compared to pre-programmed hit patterns that correspond to tracks in four p_T bins: 1-3 GeV, 3-5 GeV, 5-10 GeV and >10 GeV. The number of hits per sector is also determined to give information about the isolation of a given track. The number of tracks in each p_T bin is reported to the trigger framework, along with the number of tracks with preshower matches. For the data considered in this analysis, the CTT was commissioned but not used extensively in the trigger list. In the analysis this trigger will be ignored.

2.3.2 Level 2 Triggers

The L2 system processes data with hardware based on Field Programmable Gate Arrays (FPGAs) and microprocessors, which are separated into modules assigned to specific subsystems.

The information of the subsystems is combined into a global L2 processor [66]. On a time scale of 100 μs, it reduces the events rate by a factor of 10. At this level, muon tracks can be reconstructed in the muon chambers and simple clustering algorithms are used to reconstruct jets and electromagnetic clusters in the calorimeter.

L2 Muon Triggers

The wire hits at L2 have complete timing information including calibration. Therefore scintillator hits from a wider timing gate can be used. The L1 correlations between scintillator and wire hits, as well as A and BC layers muon segments are improved. In a first step the roughly calibrated data and L1 information is received and segments are formed, which are combined into muon candidates with p_T and track quality information. The L2 global muons are collected and sent to the L2 global processor where the trigger decision is made. The level 2 muon trigger and its performance during the early runs is described in [67].

L2 Calorimeter Trigger

The L2 calorimeter trigger consists of three processors which are designated for jet finding, electron/photon and $\not\!\!E_T$ calculation, respectively. Each processor has all 1280 trigger towers as input. The energy of each tower is packed into one byte, and has a maximum of 62 GeV for the energy sum of the electromagnetic layers or 124 GeV for the total tower energy. For a more detailed description of the level 2 calorimeter trigger, the reader is referred to [68].

- **Jet triggers**
  Jets are built from 5×5 towers centered on the seed tower. All towers passing a low p_T threshold are used as seed tower. The vertex is assumed to be at z=0 for the calculation of the transverse energy. If two jets share more than 4 towers, the jet with the maximum energy is kept.

2.3.3 Level 3 Triggers

At L3 an input rate from L2 of 1 kHz is reduced to 50 Hz. L3 is a computer farm that reconstructs events using faster and simpler versions of offline code. The triggers used in the analysis are described below.

L3 Muon Triggers

The code running on the L3 farms is a simpler and faster version of the offline muon reconstruction code. The L2 muon trigger defines regions in which the data is unpacked and where muon reconstruction is attempted. Candidates in the overlap region of the central and forward muon system which are reconstructed as two muons at lower trigger levels can be cleaned up. L3 has vertexing information, better momentum resolution from inner tracker tracks (L3 tracks) and timing information. This allows for a requirement that multiple muons share the same vertex and the timing information can separate the muon candidates into prompt, slow and out-of-time muons, where the latter are rejected as cosmic muons. The L3 muon tool was not used by triggers used for the measurement presented here.

L3 Calorimeter Triggers

- **Electron triggers**
  At L3 a fast version of the offline code for electron identification is used. The trigger decision is based on a combination of an energy threshold, a cut on the energy fraction in the electromagnetic calorimeter, requirements on shape of the cluster, and a match to a L3 track. The trigger strategy is to lower the requirements on the electron candidate for more energetic candidates.

- **Tau triggers**
  The L3 tau identification algorithm [69] is similar to the algorithm in the offline software that will be discussed later, but uses different cuts (e.g. for the track matching). L3 tau objects are built from simple cone jets with a 0.7 cone in $\eta \times \phi$. The towers inside that cone are used to calculate variables describing the transverse shape of the calorimeter cluster, using the parameters *profile* and cluster width *rms*. The profile is defined as the transverse energy in the two hottest towers divided by the total transverse energy. The cluster width is calculated using the formula: $rms = \sqrt{(\frac{\sum_i \Delta\phi * E_T^i}{\sum_i E_T^i})^2 + (\frac{\sum_i \Delta\eta * E_T^i}{\sum_i E_T^i})^2}$. Scatter-plots of these variables, calculated for signal and background from offline information, are shown in Fig. 4.10. Very loose shape cuts of a *profile* value above 0.3 and an *rms* below 0.25 are applied, while no track matched is required. For the data used in this thesis the tau filter selects events based on the transverse energy of the cluster. The cut chosen in the filters that selected tau-muon and tau-electron events was a tau object with transverse energy above 10 GeV.

L3 Track Trigger

The data from the CFT and SMT are unpacked and clustered with specific, fast L3 algorithms. The track finding, as described in detail in reference [70], starts from outside in, as the occupancy in the outer layer on the CFT is lowest. The outer two layers of the CFT are used to define track candidates using pairs of axial hits that satisfy an equation describing a straight track of a certain minimal p_T. These hits predict the region in which the next possible hits should lie in. Each of these hits is making a new track candidate, and the possibility of a 'miss' (no hit in this layer) is accounted for as well. A set number of the best track candidates is then propagated to the next layer where again, hits within the new prediction are considered. To build a three dimensional track, a histogramming method is used. To make the algorithm fast while allowing for a reasonable resolution, it is done in two steps. The first step defines coarsly the interesting region in the *z*-polar angle space for which a finer binned histogram is filled in the second step. The hits found this way are then used to perform a straight line fit to the track candidate. The found track candidates with 3D information are then propagated into the SMT where hits are added if they fulfill the extrapolation prediction. The track with SMT hits is kept if its χ^2 is better than that of the CFT-only track.
For the data used here, a minimum number of 10 *xy*-hits is required. L3 tracks are used by higher level L3 tools and as standalone trigger objects.

2.4 Luminosity

In order to convert a measured rate of events into a cross section using the formula

$$\sigma = \frac{\mathrm{d}N/\mathrm{d}t}{\mathcal{L}}, \tag{2.3}$$

the luminosity $\mathcal{L}$ has to be determined.
The luminosity can be calculated from the beam characteristics. In the absence of a crossing angle, it is given by the expression:

$$\mathcal{L} = \frac{f_{rev} B N_{\mathrm{p}} N_{\overline{\mathrm{p}}}}{2\pi(\sigma_{\mathrm{p}}^2 + \sigma_{\overline{\mathrm{p}}}^2)} F(\sigma_l/\beta^*), \tag{2.4}$$

where f_{rev} is the revolution frequency, B the number of bunches in each beam, $N_{\mathrm{p}/\overline{\mathrm{p}}}$ the number of (anti-)protons in each bunch and $\sigma_{\mathrm{p}/\overline{\mathrm{p}}}$ are the transverse beam sizes of the (anti-)proton beam. F is a form factor that depends on the bunch length σ_l and the beta function at the interaction point β^*. This method of determining the delivered luminosity is used by the beams division.
Both CDF and DØ make use of equation 2.3 by measuring the rate of events from a process with a known cross section. In the case of DØ, the total cross section of the hard (non-diffractive) processes is used. The effective luminosity is calculated taking into account the acceptance of the detector for these hard processes. The cross section and acceptance of the luminosity detector for single and double diffractive processes are taken into account as well, requiring a 5% correction to the hard process outcome.
A hard scattering cross section value for the effective luminosity of 43.26±2.07 mb was adopted at the end of Run Ib by DØ. This value is currently used in Run II as well. The change of the cross section due to the higher center of mass energy in Run II and the different efficiencies and acceptances of the upgraded luminosity detector are taken into account by quoting a 10% systematic uncertainty on the luminosity measurement. Once these effects have been studied, the measurements done prior to that will be corrected with the new luminosity value.

The rate of coincidences in the north and south luminosity counters is measured by a set of 159 scalers. Each scaler counts the rate for one of the 159 possible crossings. The number of interactions per crossing follows a Poisson distribution: $P(n) = \frac{\mu^n}{n!}e^{-\mu}$ with μ being the mean number of interactions per crossing. The rate of the processes monitored by the luminosity counters is given by $\mathrm{d}N/\mathrm{d}t = \mu f = \mathcal{L}\sigma_{\mathrm{eff}}$ with f being the crossing rate of approximately 1.7 MHz. The beam consists of many bunches and the properties are not necessarily uniform for all possible crossings of a proton and an anti-proton bunch. Hence, the rate is counted for every possible crossing separately and then averaged:

$$\mathcal{L} = \frac{f/159}{\sigma_{\mathrm{eff}}} \sum_{i=1}^{159} \ln(1 - P_i(n > 0)) = \frac{f/159}{\sigma_{\mathrm{eff}}} \sum_{i=1}^{159} \ln\left(1 - \frac{N_{LMi}}{N_{\mathrm{crossing}}/159}\right). \tag{2.5}$$

As the Tevatron operates at 53.4 MHz, able to fill every 7th wavetrain with a bunch of (anti-) protons, and has a circumference of 4 miles, there can be up to 159 different proton bunches and of course the same number of anti-proton bunches.
The calculation of the luminosity for a given trigger is similar. Here, effects where the trigger

was disabled are taken into account. Sources of trigger disables include incidences of Front-End busy and the disable of the first tick after a L1 accept as well as global disables, L2 and L3 disables. The prescales, defining the fraction of crossing where a given L1 trigger is masked, are taken into account as well. Events can be lost at every stage of the readout process [71], e.g. events missing parts of the readout are rejected. Correcting for this is difficult, given the large rejection factor of the trigger at each trigger level. Hence every exposure group contains a trigger that fires based only on a tick pattern, a so-called *zero bias* trigger. Similarly, every exposure group has to contain a *minimum bias* trigger which is defined as the *zero bias* trigger with the additional requirement of a fast-*z* signal.
The luminosity detector and measurement are described in detail in Refs.[72] and [63].

Data Taking Efficiency

The data taking efficiency is the ratio of all crossings where the detector was able to receive, trigger and readout events to all bunch crossings provided by the Tevatron. Its measurement is provided by the luminosity system which calculates both rates. In the early phases of Run II, when the detectors and the data acquisition system were still in commissioning stage, this data taking efficiency was rather low, but for the last year (as of time of this work) the efficiency averaged at ≈90%. The data taking efficiency versus time is plotted in Fig.2.12 for the data used in this analysis which were taken between May 2002 and May 2003. Figure 2.2 shows the instantaneous and integrated luminosity of a typical day (May, 8th 2003).

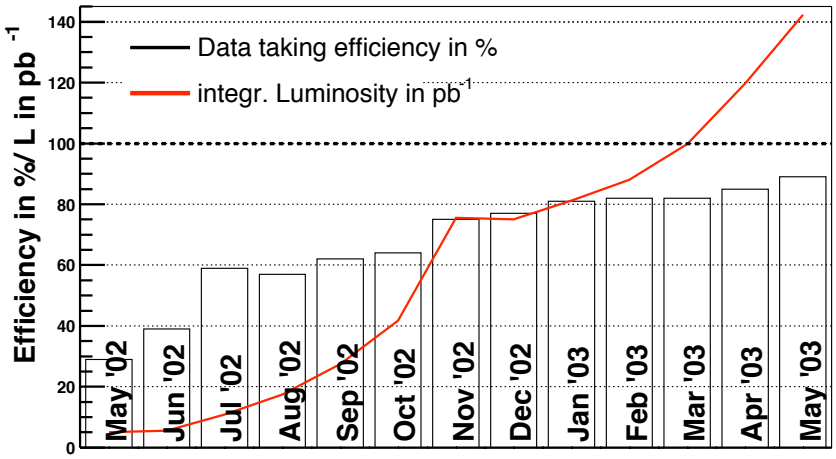

Figure 2.12: Data taking efficiency and integrated recorded luminosity for the data taking period considered in this thesis.

2.5 Monte Carlo Simulation

The Monte Carlo (MC) Simulation is done is three distinct steps:

- event generation,
- simulation of the detector response, and

- reconstruction and trigger simulation.

These steps will be discussed briefly in the following.

Event Generation

In the first step, the $p\bar{p}$ interaction is simulated using event generators such as Pythia [73] or Herwig [74]. Short-lived particles are allowed to decay in the event generator. Tau leptons are treated as stable particles in both Pythia and Herwig and are subsequently decayed using TAUOLA [75], which takes the polarization in tau decays properly into account. In the next step, the resulting quarks and gluons are hadronized by Pythia or Herwig. The different generators use different models and parameterizations of the hadronization stage, and comparisons of these generators are used to estimate systematic effects due to this modeling.

Detector Simulation

A model of the DØ detector is constructed using the GEANT3 package. This package calculates the effects of the material and magnetic field on the particles produced in the event generation while tracing them through the detector set-up. When appropriate, ionization and secondary particles due to interactions are produced. The response of the DØ detector is in turn simulated using a program called DØSIM. This program performs the following functions:

- merging the hard scatter event and minimum bias events,
- adding calorimeter noise,
- adding noise and inefficiencies for the SMT, CFT and muon system, and
- digitizing the simulated ionization and shower response.

The output of DØSIM is of the same form as the raw data from the detector and is input to the last step of the simulation chain, the reconstruction and trigger simulation.
It is of crucial importance that the detector geometry, the noise and inefficiencies are described well enough so that the reconstruction efficiencies in data are reproduced. For the calorimeter, the noise is simulated by adding a random number drawn from a Gaussian distribution with a width that is measured from data. At colliders where bunches of particles collide, the number of interactions per crossing is Poisson distributed. This means that the hard scattering interactions can be accompanied by a second, usually soft, interaction where the mean number of interactions per crossing depends on the luminosity. To simulate this, additional minimum bias events are added to the simulated events which can either be taken from simulation or from data taken with a special minimum bias trigger. The number of the minimum bias events to be added to each event is drawn from a Poisson distribution with a mean of the average instantaneous luminosity of the data that is to be simulated. The transverse shape of jets in the calorimeter is currently well described (see section 3.7). However, the tracking efficiencies and resolutions are currently considerably worse in data than in simulation, resulting from imperfect knowledge of the true detector geometry and detector efficiencies.

Reconstruction and Trigger Simulation

After the generated events have been processed by DØSIM, they can be reconstructed with the same reconstruction program as the real data. This program, DØRECO, will be described in chapter 3. In addition, the response of the trigger system can be simulated. This enables the evaluation of trigger efficiencies and development of specific triggers for a given physics process. For this analysis, the trigger efficiencies will be measured using data, but the design of the trigger is a product of studies using the trigger simulation.

Chapter 3

Event Reconstruction

The reconstruction of physics objects from raw detector data can be divided into three major steps:

- Hit finding where the raw digitized data is unpacked and converted into "hits" of definite energy and spatial location. The hits can concern e.g calorimeter cells, CFT fibers, silicon strips, etc.
- Clustering and tracking where the hits are combined into lower level physics objects like calorimeter clusters and tracks.
- Particle identification where the clusters and tracks are combined to form physics objects like electrons, muons, taus and jets. Loose cuts are applied in the reconstruction to achieve a high efficiency.

The reconstruction steps are described below, starting from finding tracks to identifying particles. The physics objects are defined to have the best efficiency in the reconstruction. This does not warrant the identification or reconstruction with the highest purity. For the analysis, tighter cuts to the physics objects are applied, which will be described in the event selection in chapter 4.

3.1 Charged Track Reconstruction

The first step in track finding is the hit reconstruction. There are two classes of hits corresponding to the two inner tracking detector systems. The first are the CFT hits, which are of two types: axial hits and stereo hits (hits of the axial fibers or the 3° stereo fibers, respectively), which can be combined into 3D-clusters. Hits are fibers with an ADC count above 20 for the version of the reconstruction software used for this analysis. More recent versions require ADC readout above 1 photo-electron, which corresponds to a variable number of counts depending on the different channel to channel response.
In the case of the SMT, only strips above a threshold of $2\sigma_{\text{noise}}$ above the pedestal and their neighbors are read out (sparse mode). For the SMT, all hits are combined into 3D-hits, before they are used in the tracking. Combinations of hits from two different tracks may form so-called "ghost-hits". These ambiguities can be reduced for double-sided silicon detectors by using the

correlation between the charge collected in the two views. While this works in the MC, it is not yet implemented for data.

In the reconstruction program versions used in this analysis, p13.05.00, p13.06.01 and r13.06.01, the central tracks stem from a combination of the output of two different algorithms:

- a road approach (GTR), and
- a Hough transform based histogramming technique (HTF)

The GTR tracking algorithm is described in detail in [76]. It consists of five components: surfaces, paths, propagators, fitters and filters. GTR builds a model of the detector using "surfaces", which can be cylinders or planes. The track parameters and errors can be calculated for each such surface. Lists of these surfaces that a particle originating in a $p\overline{p}$ interaction would cross are the so-called "paths". "Propagators" are used to extrapolate track parameters and their error matrix from one surface to another, taking the magnetic field and the encountered material into account.
The hits of the first few surfaces are used to define "seed tracks", which are then extrapolated further to the remaining surfaces they may have left a hit on. The task of the "fitters" is to match a new cluster to a track, once it reaches a new surface. A match χ^2 is calculated and, if it is too high, the cluster is rejected. The final step of track finding with GTR is the clean-up of all candidate tracks found using a certain path. This is done by the remaining GTR component, the "filter", which rejects tracks on the basis of their overall χ^2 and the number of traversed surfaces without matched cluster. The final list of track candidates can then either be put through another "path" (or detector) or comprise the final list of tracks.
Following the geometrical acceptance of the two tracking systems, there are four different regions with dedicated "paths":

- in the central region with full CFT coverage, track finding starts using the CFT. First, the axial hits are used and track candidates in $r-\phi$ are found. After removing duplicate tracks, the stereo hits are added to the tracks. The resulting 3D track candidates are extrapolated into the SMT, requiring a minimum of 16 CFT hits.
- in the overlap region with partial CFT coverage, track finding starts with the CFT. Here, axial and stereo hits are combined first to speed up the process. Only tracks consistent with passing at the edge of the fiber tracker are allowed.
- in the gap and forward regions, with very little fiber tracker coverage, track finding starts in the outer layers of the SMT and the F-disks. Tracks are required to have at least 4 SMT hits.
- Sub-optimal calibration and alignment of the detector for early data necessitated the inclusion of an addition "path" for tracks to reduce the inefficiency introduced by the requirement of 16 CFT hits in the central part of the detector: tracks seeded in SMT and extended into the CFT are allowed to miss one axial CFT layer and all stereo layers.

The HTF algorithm is based on the Hough transform mechanism and is described in Ref. [77]. First, only $r-\phi$ information is used. A pair of $x-y$ co-ordinates corresponds to a line or a region,

with measurement uncertainty, in the (ρ, ϕ) plane, where $\rho = qB/p_T$. For each pair of hits, the content of a bin of a 2D histogram in the (ρ, ϕ) plane is incremented, if it intersects the region corresponding to a pair of hits. Bins corresponding to a track will have $n(n-1)/2$ entries, where n is the number of hits on the track. Combinations of hits from two different tracks contribute to a randomly distributed background. After the histogram is filled, cells with too few hits are discarded. If two cells share all their entries, the candidate with the lower number of entries is disregarded. The cells remaining are forming a track template that is subjected to Kalman filtering, where the three parameters of the $r - \phi$ trajectory are fitted and the material effects are properly taken into account. In order to use the z information, another histogram in the parameter space (z_o, C) plane is filled, where $C = \mathrm{d}r/\mathrm{d}z$. The (r, z) measurements of the hits is used and again, all hits combinations are considered. Finally a Kalman filtering step discards fake templates, wrong hits and determines the track parameters accurately. The method is valid as long as only tracks with modest impact parameters are considered.
At present, the algorithm uses two complementary strategies:

- find track templates with SMT hits only, then extrapolate the tracks into the CFT,
- find tracks using CFT hits, then extrapolate them into the SMT.

Tracks found by both algorithms are combined.

3.1.1 Vertex Reconstruction

After the tracks are found, a reconstruction of primary and secondary vertices is performed. The reconstruction and selection of primary vertices is described in detail in [78], a short description of the algorithm follows. Primary vertex reconstruction starts with a list of all reconstructed tracks. Of these, only tracks with an impact parameter significance with respect to the beam line of less than three are kept, since tracks with high impact parameters can come from decays of particles with a lifetime and not from the primary vertex. All remaining tracks are fitted to a single vertex and the track with the highest χ^2 is dropped. This procedure is repeated until the χ^2 of the fit for each track drops below ten. The entire procedure is then repeated with the remaining tracks. All vertices reconstructed this way are kept in a list of primary vertices. Currently, the vertex with the highest p_T sum of the associated tracks is picked as main primary vertex. The track and calorimeter quantities η, θ, E_T, etc. are defined with respect to this main primary vertex.

After the primary vertices are defined, secondary vertex finding tries to reconstruct the decay position of long lived particles. For this analysis, the reconstruction of secondary vertices will not be used .

3.2 Calorimeter Clusters

The DØ calorimeter consists of 55000 readout cells. The readout is “zero-suppressed” which means that only energies with a value above pedestal and noise are read out. “Above noise” is quantified as the ratio of the measured energy above pedestal and the mean width of the noise measured in the particular channel: one refers to a suppression of “$x\ \sigma$”. The thresholds used

for the run period considered in this thesis were 1.5 σ online with an additional "offline" suppression of 2.5 σ.

Due to electronic or uranium noise or liquid Argon contamination, calorimeter cells with unusually high incidence of spurious energy can appear. To flag these hot cells and prevent them from distorting further reconstruction, a hot-cell killer algorithm is used, called NADA [79]. This algorithm considers the energies in a 3×3 window in $\eta \times \phi$ around the cell in question, and the same region in the layers below and above. Cells in the third EM layer with a segmentation of 0.05 in $\eta \times \phi$ are combined into groups of four to have the same effective granularity in all layers. Neighboring cells below 100 MeV are disregarded. If the sum of energies in the neighboring cells (cube energy) around the potential hot cell is below the given threshold, the cell is flagged as a hot cell. This threshold can be static or dynamic. Cells with negative energies below -1 GeV or with unphysical high energies above 500 GeV are all flagged. Cells of medium E_T between 1 and 5 GeV are flagged using a static threshold of 100 MeV. The same is true for all cells in the first electromagnetic, fine hadronic and coarse hadronic layers as well as the fourth electromagnetic layer and the layers corresponding to the intercryostat detectors. For the remainder, a dynamic threshold is used: all cells with a cube energy below 0.02*E_{cell} are flagged.

3.3 Jet Reconstruction

Jet reconstruction at $p\bar{p}$ colliders is historically done with cone-based algorithms. Algorithms using k_T ordering, as used at electron-positron colliders like LEP, will not be discussed here, but information on the use of this algorithm at hadron colliders can be found in the literature [80, 81, 82]. The jet finding algorithm used for data analysis in Run II is based on the joint theoretical and experimental recommendation for the reconstruction of jets at hadron colliders [83].
All "seed towers" (towers above the seed E_T threshold) are first selected. If two seed towers are closer than twice the jet radius R in (η, ϕ), the midpoint between them is added to the list of seeds. Jets are formed using a 4-vector recombination scheme, summing up the components of the individual towers within the jet. Towers are part of a jet if they are within a distance R in (η, ϕ) space. The recalculated centroid of the newly formed cluster is energy weighted:

$$\phi_{wt} = \frac{\sum E_T * \phi}{\sum E_T}, \qquad \eta_{wt} = \frac{\sum E_T * \eta}{\sum E_T}.$$

This new centroid position is then used instead of the seed (η, ϕ) and the jet formation step is repeated until the centroid direction is stable. After all jets are formed from the seeds, splitting and merging is performed. If the shared energy between two jets is above 50% of the transverse energy of the lower E_T jet, the lower E_T jet is killed. For a smaller shared-energy fraction, the towers are uniquely assigned to the jet closer in $\eta - \phi$ space.
A variation of this jet finding algorithm is the "Simple Cone Algorithm". Towers inside a cone of a fixed radius from the starting tower are added to the cluster if they are above the clustering threshold and then deleted from the list of available towers. The resulting cluster is added to the list of jets if the transverse momentum is above threshold. These steps are then repeated until all towers above the seed threshold have been used.

All of these algorithms can be initiated either directly from all calorimeter towers or from pre-clusters ("seeds") which are found using simple algorithms. This pre-clustering is done to save computing time but is undesirable from a theoretical point of view. The main motivation for the midpoint seeding used by the Run II algorithm is to approach a seedless algorithm.

3.4 Missing E_T

As explained in section 2.2.1, the conservation of energy in proton anti-proton collisions cannot be used as a constraint to measure the longitudinal energy of particles which escape detection. However, to first approximation, the total momentum in the transverse plane is conserved. Hence missing energy in the plane normal to the beam-line is caused only by particles that have very small interactions with matter such as neutrinos or by mis-measurement of the "visible" final state.
The missing transverse energy ($\not\!\!E_T$) is calculated by summing the transverse energies of all calorimeter cells above 200 MeV using the following equation

$$\not\!\!E_X = -\Sigma E_T \cos\phi, \quad \not\!\!E_Y = -\Sigma E_T \sin\phi, \tag{3.1}$$

$$\not\!\!E_T = \sqrt{\not\!\!E_X{}^2 + \not\!\!E_Y{}^2}.$$

The cell-threshold is optimized to use most of the measured information while keeping the contribution from noise in the calorimeter readout small. To calculate the transverse energy from the scalar energy measured in each cell, the interaction vertex calculated using tracks as discussed in section 3.1.1 is used.
The noise level in the coarse hadronic part is higher than for other layers due to a higher conversion factor of ADC counts to measured energy for these cells, leading to many noisy cells passing the 200 MeV cut. To keep the influence of the noise on the measurement of the $\not\!\!E_T$ small, cells in the coarse hadronic layers are only used if they are part of a reconstructed jet.

3.5 Electrons and Photons

Electrons and photons are reconstructed in DØ using three different algorithms: one based on a simple cone method [84], a second one using a clustering algorithm specifically designed to resolve single particles in the DØ calorimeter [85] and an algorithm seeded by tracks which is used to reconstruct non-isolated electrons [86]. For this analysis only the first algorithm is used and will be described briefly.
The electromagnetic clusters are seeded by towers with a transverse energy above 1.5 GeV and an electromagnetic energy fraction higher than 0.9. Towers in a 10×10 tower window around the seed tower are used to calculate the isolation variable defined as the energy between cone-radii of 0.2 and 0.4 divided by the core energy contained in the 0.2 cone. For isolated electrons, this ratio should be below 0.2.
The track match for an electron uses a χ^2 match calculated using the ϕ direction, z position at the shower maximum (EM3) layer and, if desired, the transverse momentum. The energy scale for

electromagnetic objects is calibrated using $Z^0 \rightarrow e^+e^-$events from data. The correction depends on the η and energy of the EM object.
In addition to the electromagnetic energy fraction and isolation, the so-called H-matrix [87, 88], is used. The H-matrix is the inverse of a covariance matrix of N variables, there is one for signal and one for background. The χ^2, calculated with the H-matrix, of any candidate to be background is subtracted from its χ^2 to be signal. The H-matrix currently in use for electrons utilizes eight correlated variables: the four EM energy fractions, the logarithm of the total EM energy, the vertex z-position and the transverse shower width in the third electromagnetic layer in ϕ and z. The 8×8 covariance matrix is a measure of how similar the shower is to an electron shower or to a non-electron background shower.

3.6 Muon Reconstruction

Three detector components are used in reconstructing muons: tracks in the muon system to reconstruct a so-called local muon, the central tracker to measure the muon track parameters more precisely and the calorimeter where the muon deposits energy consistent with a minimum-ionizing particle.

3.6.1 Local Muons

The reconstruction of a muon track in the muon system is performed in three steps: hit finding, segment reconstruction, track finding and fitting.

Corresponding to the three types of muon detectors, there are three different types of hits: scintillator hits where the hit position is taken to be the center of the scintillator slab, and MDT and PDT hits. As the MDTs are only read out on one side, the drift-time and axial time cannot be disentangled unless information from scintillator pixels or a track candidate is used. The PDTs of the central muon system are read out on both sides allowing the drift time and distance both to be measured.
Segments are the result from a straight line fit through two or more wire hits within a layer. They have both position and direction and can be combined with scintillator hits if present.
The muon segments are then combined to form tracks. The A-layer segments must be consistent with a muon coming from the primary interaction in z, and are combined with outer segments if they have an opening angle of less than 0.6 radian. This is illustrated in Fig. 3.1a). In addition, single hits are allowed to be combined with a segment in another layer. The deflection angle θ between segments in the toroidal field, which is illustrated in Fig.3.1 b), is used to estimate the muon momentum, which is given by formula:

$$p = \frac{0.3Bs}{|\tan\theta|}, \tag{3.2}$$

where s is the distance traveled in the toroidal field and B the toroidal field strength of ≈1.6 T. The hits are updated with the track information and the fit is performed again to obtain the most accurate information possible. This entire procedure is iterative: if the fit does not converge after ten iterations, the first estimate of the muon momentum is used.

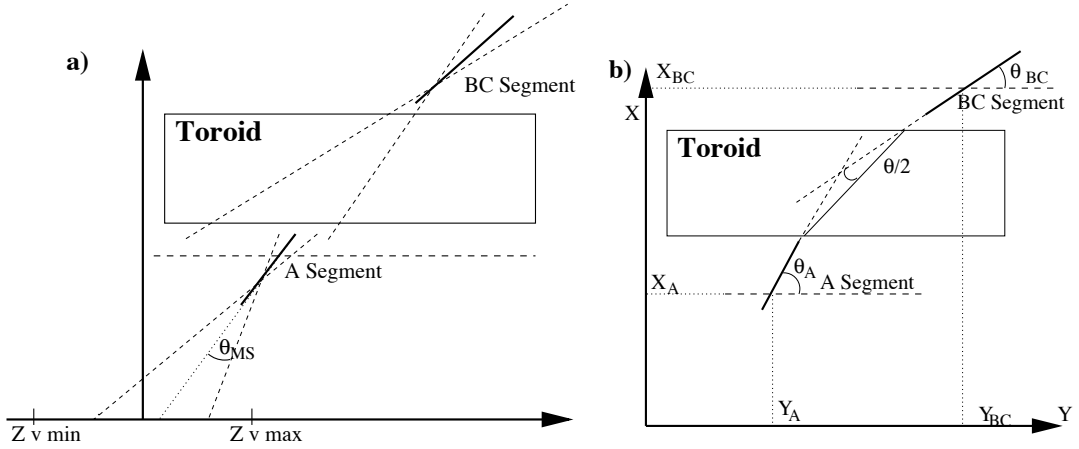

Figure 3.1: a) Illustrates the selection of muon segments to form a local muon track. b) The momentum measurement of the local track.

3.6.2 Global Muons

The algorithm used for local muon track finding is also used to define global muons, this is in DØ usually referred to as the "Saclay"-algorithm. The inputs are muon segments and central tracks, the reconstruction of which is detailed above. The scattering of the muon inside the calorimeter and the toroid is approximated by using two thin scattering planes.

The fit requires at least a line on one side and a point on the other side of the scattering plane as input, corresponding to three points measured in the local muon system. Thus the fit can only be used for local muons that are energetic enough to traverse the toroid. In addition, the acceptance has a hole corresponding to the region in ϕ without A-ϕ counters. If a central track is present, it can be extended into the BC layer, thus allowing for matches in that region. Similarly, the fit can still be performed when a central track and an A layer segment are present.

3.6.3 Calorimeter Muons

For typical muon energies at the Tevatron collider, muons are minimum ionizing particles. As such, they loose a small and fixed amount of energy per distance and thus leave a distinct signature in the calorimeter. As the hadronic layers of the calorimeter are thicker, the energy deposited there is larger and only these cells will be used in MIP-finding. For EM-cells the MIP signal is close to noise level. The algorithm to find calorimeter muons is described in [89] and is based on a 2D histogram in $\eta - \phi$, in which every cell with an energy above 100 MeV has an entry. The η value is calculated with respect to the reconstructed primary vertex: if none is found z=0 is used.

In the central region, three layers of Fine Hadronic calorimeter are followed by a Coarse Hadronic layer, hence a calorimeter muon would have 4 hits. An additional Fine Hadronic layer is added in the forward cryostats for $|\eta| > 1.4$. Up to two Coarse Hadronic layers follow, thus muons can leave up to six hits in the forward region. Candidates of calorimeter muons (Muon Track in the Calorimeter or MTC) are formed if a histogram entry is above three or four hits for the central and forward cryostats, respectively. To find muons which cross towers as

well, a second histogram is filled which allows 2×2 squares to contribute hits. To reduce the number of hot regions contributing to MTC candidates, the number of hits must be less than the number of layers plus one.
A variable quantifying the similarity of the energy deposits to a muon track is employed to reduce the number of fake MTC candidates. The energy deposit in each layer from muons from Z^0 decays is fitted with a Landau-distribution. The same distribution is made for background candidates that have a matching track but no matching muon segment. These parametrized functions $S(E_l)/B(E_l)$ are used to define a measure of the consistency of a set of energy deposits E_l with the expectation for a muon:

$$P(E) = \frac{\Pi\, S_l(E_l)}{\Pi\, S_l(E_l) + \Pi\, B_l(E_l)}. \tag{3.3}$$

For a good muon candidate, $P(E)$ >0.5 is required.

3.6.4 Muon Candidates

Muon candidates contain information from all three parts of muon reconstruction. In addition isolation variables are calculated using the multiplicity and transverse momenta of tracks as well as the calorimetric energy in cones around the muon direction.

Based upon the local muon information, three different muon qualities are defined in accordance with [90]. These are summarized in Table 3.1.

muon quality	tight	medium	loose
A layer wire hits	≥2	≥2	≥2
BC layer wire hits	≥3	≥2	≥2
A layer scintillator hits	≥1	≥1	≥1
BC layer scintillator hits	≥1	≥1	≥1
	local track fit converged		two of the above, A layer conditions treated as one

Table 3.1: Muon quality definition as in [90].

As additional requirement it may be imposed that muons failing timing cuts on the scintillator hits are rejected. The time window to reject a muon candidate as a cosmic muon is ±10 ns for A-layer scintillator hits and −15 to 10 ns for the outer layers.

3.7 Reconstruction of Hadronic Decays of τ leptons

Tau reconstruction is performed in four steps. First, the tau calorimeter cluster is built. Second, the candidate's π^0 decay products are resolved into calorimeter clusters. Third, tracks are matched to the tau candidate. Finally, the information gathered in steps two and three is used to assign a type to the candidate. The so-called "tau types" correspond to the different tau hadronic final states.

3.7.1 Calorimeter

Calorimeter Cluster

Calorimeter clusters for tau candidates are seeded in two ways. The first begins with jets reconstructed using the simple cone algorithm, starting from seed towers above 1 GeV and using a cone size of 0.3 in $\eta - \phi$. The E_T-threshold for these clusters is 4 GeV. In addition, all tracks with a transverse momentum above 5 GeV are used as seeds. If the calorimetric energy in an 0.3 cone around the track exceeds 2 GeV, the cluster is also added to the list of tau candidates. An outer cone of 0.5 in $\eta - \phi$ is used for the calculation of variables describing the transverse shape of the cluster. The isolation is defined as the energy between the 0.3 and 0.5 cones divided by the core (0.3 cone) energy and is required to be smaller than 1.

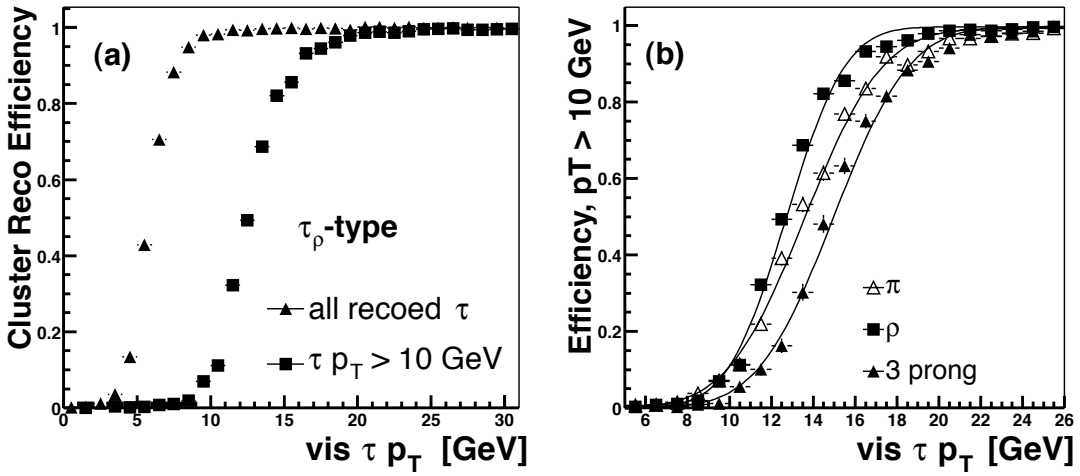

Figure 3.2: Reconstruction efficiency for tau clusters as a function of the true visible transverse momentum of the τ: a) shows the overall efficiency for a cluster to be reconstructed (triangles) and to have a reconstructed, uncorrected E_T above 10 GeV (squares); b) the turn-on behavior of the three tau final states τ_π (open triangles), τ_ρ (squares) and τ_{3pr} (solid triangles). These tau types are defined in the text. The curves are fits with an error function intended to guide the eye.

The energy and momentum of all the tau daughters that are not neutrinos are referred to as the "visible" tau energy and momentum. The efficiency of this algorithm versus the true p_T of the visible τ decay products is plotted in Fig. 3.2a). The effect of a cut on the transverse energy of the cluster at 10 GeV is also shown. The 50% point of the turn-on curve is above 10 GeV since the cut is applied to the uncorrected reconstructed tau momentum. The energy-scale correction is described in section 3.7.4. Figure 3.2b) shows the turn-on of the cluster reconstruction efficiency separated into the three main tau final states $\tau \to \pi^\pm \nu_\tau$ (τ_π), $\tau \to \rho$ (nπ^0) (τ_ρ) and $\tau \to$ 3-prong (τ_{3pr}). The classification is further explained in section 3.7.3.

Reconstruction of π^0 in the τ Decay

The fine segmentation of the DØ calorimeter enables the reconstruction of the π^0 clusters distinct from the charged pions in tau decays. A nearest-neighbor algorithm is used for the cells in the third EM layer of the calorimeter. This layer is at the shower maximum of electromagnetic

showers and has segmentation four times as fine (0.05×0.05 in $\eta\phi$) as the other layers. The cell with the highest E_T is used as a seed, and the neighbor with the highest E_T is added to the cluster. These two cells and all their neighbors sharing a common boundary are combined to an EM3 sub-cluster. The energy of cells in the other EM layers overlapping with the cluster are then added to this object. All unused cells are used to search for more sub-clusters. Sub-clusters are kept if their transverse energy in the third EM layer exceeds 0.8 GeV and constitute the π^0-candidates.

3.7.2 Tracks

To conserve charge, τ final states include an odd number of charged particles with a charge sum of ±1. Due to the τ boost, the τ daughters are nearly collinear with the original τ direction and their invariant mass must be smaller than m_τ. Since the τ releases significant energy in low-multiplicity decays, the transverse momentum of the charged daughters tends to be higher than for charged particles produced in the formation of jets from quarks and gluons (QCD background). The primary task in τ track selection is to find the real τ daughters and reject tracks from the underlying event or other interactions. Measurements in the tracking system in combination with the calorimeter can be used to distinguish real τ-leptons from fake candidates produced by QCD jets.

Tracks are first sorted in decreasing transverse momentum. Assignment of an incorrect z-vertex to the calorimeter cluster results in the wrong η value and leads to track-matching failures. To correct for this, the track η used in the matching is re-calculated using the reconstructed primary vertex for the event (see section 3.1.1). The track direction at the preshower detector radius is used to account for the multiple scattering caused by the material in front of the calorimeter and the deflection of the track in the magnetic field.
The track-matching requirements for tau candidates are:

- the track $p_T > 1.5$ GeV,
- the track is inside an $\eta - \phi$ cone of 0.5 around the calorimeter tau cluster,
- 2^{nd} and 3^{rd} track within 2 cm of the z position of the distance of closest approach to the beam line (DCA) of the first track,
- $m(1^{\text{st}}$ track, 2^{nd} track) < 1.1 GeV,
- $m(1^{\text{st}}$ track, 2^{nd} track, 3^{rd} track) < 2. GeV,
- $|\sum_{\text{tracks}} q| = 1$.

The efficiencies of the p_T and angular requirement are shown in Fig.3.3 (a) and (b), using Monte Carlo $Z^0/\gamma \rightarrow \tau\tau$ decays with $\tau\tau$ invariant masses between 60 and 130 GeV. The 1.5 GeV cut is nearly 100% efficient for 1-prong decays above 10 GeV and the leading three-prong track. About 5% of ρ daughter tracks are lost. The cut leads to a loss of 17% of the softest track of a three-prong. Real tau daughters are essentially contained in a 0.5 cone, only 0.1±0.01% are

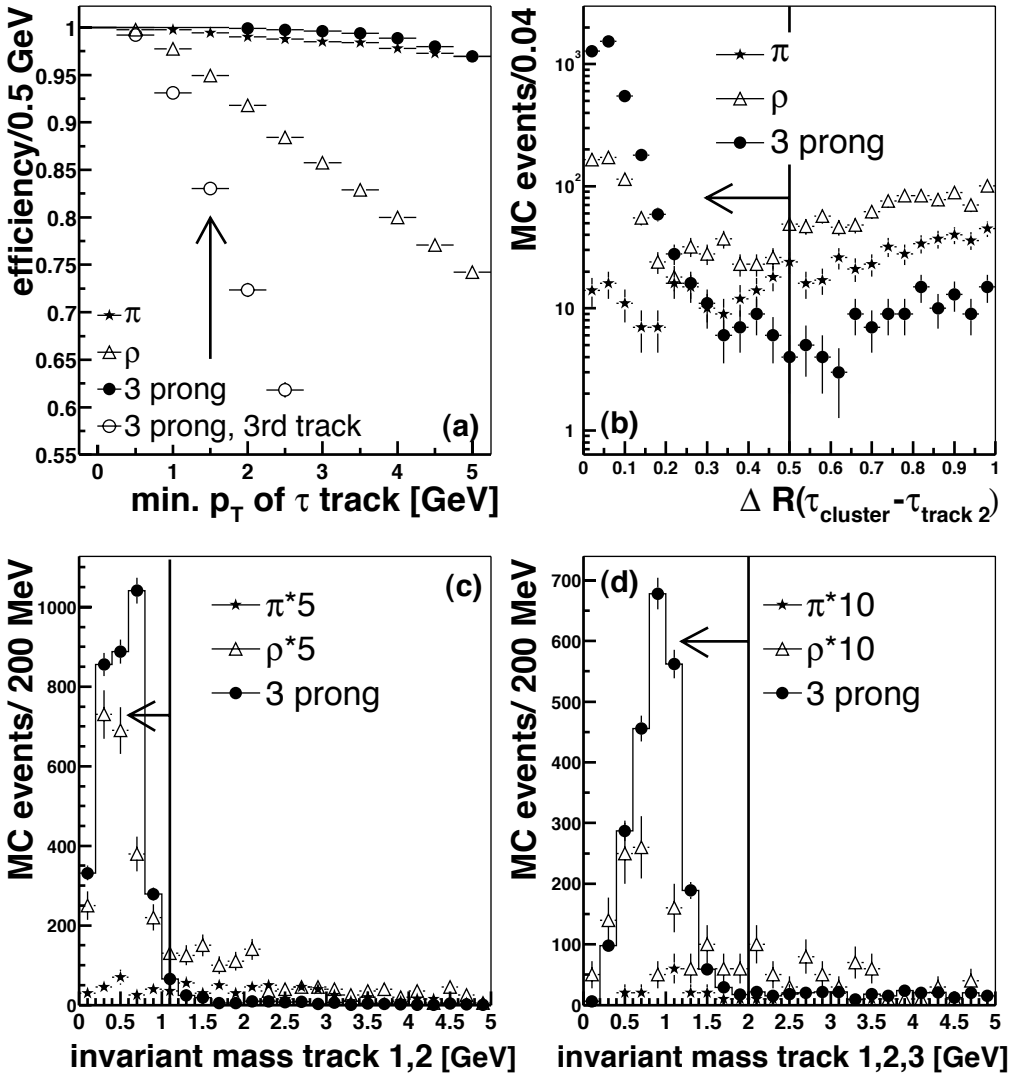

Figure 3.3: (a) the efficiency as a function of the track p_T cut; (b) the distance in $\eta - \phi$ between the tau cluster and the second track; (c) and (d) the invariant mass of the leading two and three track combinations, respectively. The cuts are indicated by lines and arrows.

rejected due to the matching requirement. Figure 3.3(b) shows the ΔR of the tau cluster and the track with the second highest transverse momentum.

The candidate track with the highest p_T is chosen as leading tau-track. Its DCA to the beam line is used as z-position of the tau production. Additional track candidates have to have a DCA z-value within 2 cm of this position to reject tracks from other interactions occurring in the same beam crossing.

A second track is only added if its invariant mass with the first track is below 1.1 GeV. This requirement does not cut on three prong decays, but for one prong decays the addition of underlying event tracks is minimized. Background tracks around the pion are essentially distributed flat in $\eta - \phi$ space. For ρ, there is in addition a contribution most likely caused by photon conversions following $\pi^0 \rightarrow 2\gamma$. This contribution appears in the distributions of the cluster-track

angle as a peak at low angles of the leading and second track and as an excess of events with low values of the invariant mass of the first two or three tau-tracks above the expectation from random tracks of the underlying event. For the third track the sum of the charges has to have an absolute value of 1 and the invariant mass of the three tracks is required to be less than 2 GeV. The invariant mass distributions for Monte Carlo three prong decays and for background tracks in one prong events are shown in Fig.3.3 (c) and (d).

3.7.3 Classification of τ Types

After the previous two reconstruction steps, the τ candidates are classified into types corresponding to the different τ decay modes. These types are called τ_π , τ_ρ and τ_{3pr}. Classification in these types is inpired by the dominant hadronic decay modes $\tau \to \pi^\pm \nu_\tau$ (τ_π), $\tau \to \pi^\pm (n\pi^0)\nu_\tau$ (τ_ρ) and $\tau \to$3-prong (τ_{3pr}). The classification is performed using the number of tracks and reconstructed EM clusters with a transverse energy in the third EM layer above 0.8 GeV as summarized in Table 3.2. In addition, tau candidates without a track match are referred to as "type 0" decays.

	τ_π	τ_ρ	τ_{3pr}
# tracks	1	1	>1
EM cluster >0.8 GeV	0	1	≥ 0

Table 3.2: Classification of the τ candidates into the three types.

The relevance of this type-classification has been studied with Monte Carlo and is shown in Fig. 3.4 (a), (b) and (c).

More than half of the $\tau \to \pi^\pm \nu_\tau$ are reconstructed with an additional EM cluster, and hence are classified as τ_ρ. In the ICD region (1.1< $|\eta_{det}|$ < 1.5), about half of all $\tau \to \pi^\pm (n\pi^0)\nu_\tau$ are classified as τ_π due to lack of coverage of the electromagnetic calorimeter in the inter-cryostat region. The number of τ in the ICD region reconstructed as τ_π and τ_ρ type are roughly equal as well as the number of correct and wrong assignments. Thus, in this region only separation of one and three prong decays is possible.
For the region outside of the ICD region, the plots (e) and (f) in Fig. 3.4 illustrate the separation between τ_ρ-types from $\tau \to \pi^\pm \nu_\tau$ pions and true $\tau \to \pi^\pm (n\pi^0)\nu_\tau$ events using the angle between the track and the electromagnetic subcluster, in combination with the energy fraction in the first two layers of the calorimeter. Events with an angle between track and neutral cluster of less than 0.03 rad and an EM-fraction in calorimeter layers 1 and 2 of less than 0.03 are reclassified as τ_π types. Using these cuts, 15% of the early showering pions, reconstructed as τ_ρ are re-assigned the correct type.

3.7.4 Energy Scale and Resolution

The measured energy of reconstructed calorimeter clusters has to be calibrated to represent the correct value. The first step in determining the energy scale of the DØ calorimeter is calibration of electromagnetic clusters. For electrons, the correction functions for energies lost in the cracks between towers is determined using MC events. In addition, the energies of electrons in the $Z^0 \to$

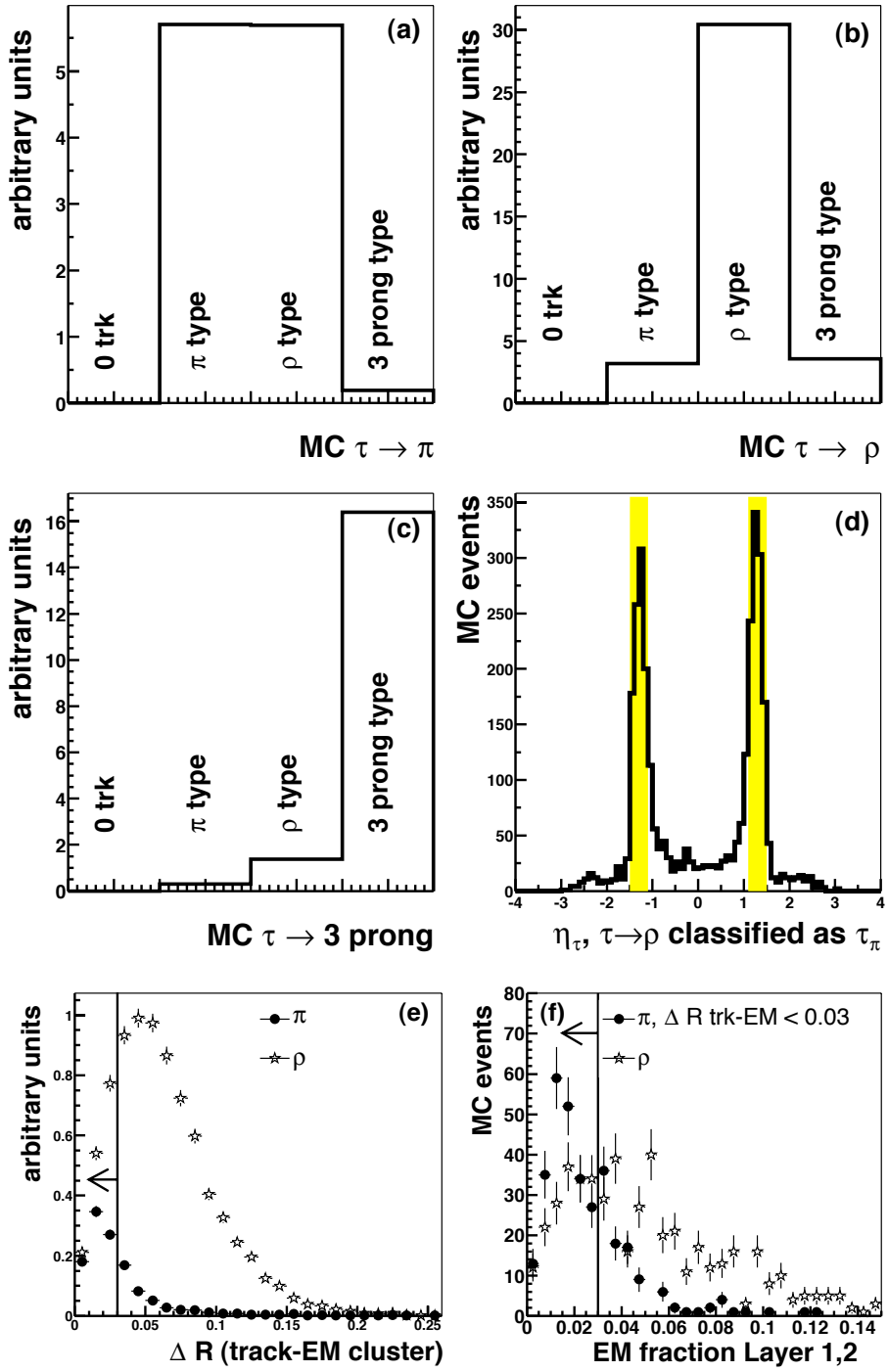

Figure 3.4: (a), (b) and (c) the reconstructed tau type for each MC tau type; (d) η distribution for $\tau \to \pi^{\pm}(n\pi^0)\nu_\tau$ decays reconstructed as π-types. The ICD region is indicated by gray bands. For candidates outside of the ICD region, the track-EM subcluster angle (e) and the energy fraction in the first two EM layers (f) are shown.

e^-e^+ peak in data are corrected to have the measured mass to agree with the Z^0 mass from the Particle Data Group [91].

The method used to determine the energy scale for jets utilizes events where a photon recoils against a jet and is described in detail in references [92, 93]. The energy of the photon is corrected as described before for electrons and this measurement is used to correct the jet energy measurement. The jet energy scale can be written in the following form:

$$E^{\text{jet}}_{\text{particle}} = \frac{E^{\text{calo}}_{\text{jet}} - E_{\text{offset}}(R, \eta_{\text{phys}}, \mathcal{L})}{R_{\text{jet}}(R, \eta_{\text{det}}, E) F_s(R, \eta_{\text{phys}}, E)},$$

where E_{offset} is the offset correction, R_{jet} is the jet response and F_s is the showering correction. The collider environment can add additional energy deposits in the calorimeter. This is corrected with the *offset* factor E_{offset},which naturally depends on the luminosity $\mathcal{L}$. The showering correction F_s is due to the fixed cones size and corrects for particles which, due to physics and detector resolution deposit their energy outside of the jet cone. The *response* R_{jet} is the largest correction to the jet energy. Due to dead material in the detector, uninstrumented regions and an e/π response ratio larger than one, the response is usually lower than one. Due to module to module variation and the influence of uninstrumented regions, this correction is a function of the detector η. In addition, it is parameterized as a function of the jet energy. A summary of the jet energy scale correction at DØ in early Run II data can be found in [94].
Since taus appear as narrow jets where the energy is in general contained in a few towers, these factors will be different than for QCD jets. Thus, the energy scale must be determined separately.
The energy scale for hadronic taus is important for the reconstruction of the di-τ invariant mass. Good resolution of this peak is essential in disentangling the Z^0 contribution from a neutral Higgs boson which would appear as a second peak at higher mass with much smaller cross-section. In the general case of searches for new particles which decay into taus, precise determination of the tau momentum helps to reduce backgrounds and enables one to draw conclusions regarding the properties of such unknown particles.

There are two independent sub-detectors providing information about the momentum of the reconstructed τ's, the tracking system and the calorimeter. The most precise information about the true τ momentum should be obtained by an appropriate combination of this information, which naturally depends on the τ-type. In the following we will refer to the reconstructed tau type when discussing the best determination of the energy scale for visible tau energy.

For pion-type taus, the total visible energy is carried by the charged pion and both the track and calorimetric cluster should give the same result. Turning this around, the scale for the calorimetric energy can be determined using the track measurement. The energy resolution and scale for τ_π taus can be seen in Fig. 3.5 (a). The calorimeter energy response is lower than the one of the tracking and its resolution is broader. The best estimate of the tau momentum for τ_π candidates is the track measurement.

In ρ-decays, the energy deposition in the calorimeter is due to two or more particles, the charged pion as in the single pion case and one or more neutral pions. The π^0 decays into two photons and the energy scale of these electromagnetic shower is determined using the $Z^0 \rightarrow e^- e^+$ peak. The energy of the charged $\pi^\pm$ can be taken from the track measurement. The resolution of the calorimetric cluster, taking into account the electromagnetic energy scale, and the energy determined using the track and the corrected EM cluster energy are plotted in Fig. 3.5 (b). The

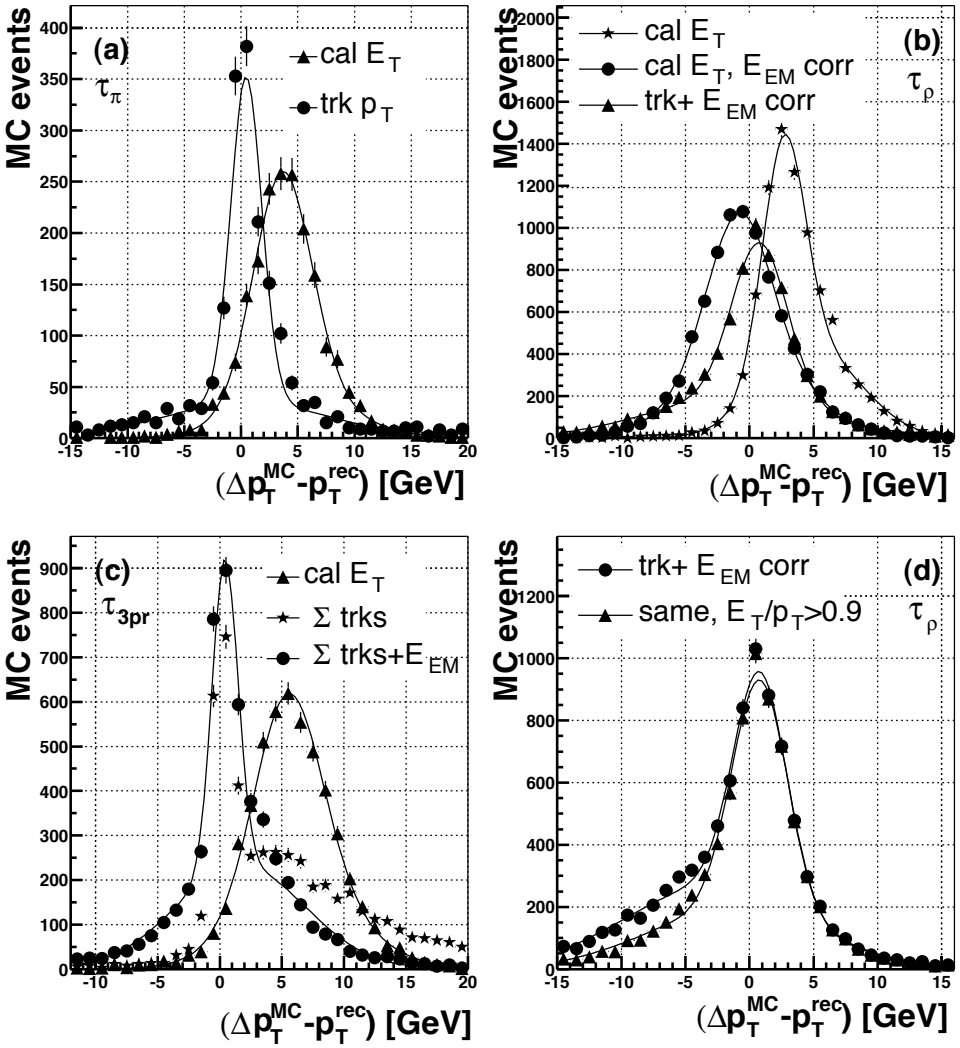

Figure 3.5: Energy resolution using different methods to calculate the tau energy. (a) shows the resolution of τ_π taus for the calorimeter measurement (triangles) and the track (solid dots). (b) shows the same variable for τ_ρ taus, using the calorimeter measurement after (solid dots) and before (stars) correcting the electromagnetic energy. The triangles show the resolution achieved using the track momentum and the corrected electromagnetic energy. This variable is shown in (d) as well, for all τ_ρ taus (dots) and for those with E_T/p_T >0.9. (c) the momentum resolution for three prongs taus using the calorimeter measurement (triangles), the tracks (stars) and using the sum of the track momenta and adding the EM cluster energy in cases where E_T/p_T is larger than one (solid dots).

best resolution is obtained using the track and corrected EM cluster energy. The distribution peaks at zero, indicating that the scale is correct. For pions, E_T/p_T is supposed to be one. If the energy scale is not corrected it will therefore be lower. In ρ decays, the true energy in the calorimeter must be larger than the track energy since the cluster is caused by two or more particles. Requiring E_T/p_T to be above 0.9 cleans the ρ-sample from misidentified $\tau \rightarrow \pi^\pm \nu_\tau$ without significantly cutting into the efficiency. This is illustrated in Fig.3.5(d).

In tau decays with more than one track, the energy can be taken from the calorimetric energy or the sum of the reconstructed, matched tracks. Figure 3.5 (c) shows the difference of MC and measured energy for these variables. When tracks are used, a narrow peak at zero appears. The upper tail is caused by events where the tau decays into charged particles and neutral pions. Using the sum of the track momenta and the electromagnetic energy to candidates when E_T/p_T is larger than one reduces this tail without enhancing the tail on the negative side.

3.7.5 Tau Identification Variables

Hadronically decaying tau leptons appear in the detector as narrow jets. The most important variables used to separate tau leptons from QCD background quantify the tau shape using tracking or calorimeter information.
The first variable used is the "profile", used previously by DØ in Run I. The profile is defined as $(E_T^1 + E_T^2)/\Sigma E_T$, where $E_T^{1,2}$ are the transverse energies of the first and second most energetic calorimeter tower and ΣE_T is the total calorimeter transverse energy of the tau-cluster. For taus, the energy is usually contained within a few towers while more towers hold similar amounts of energy in QCD jets. Another variable describing the shower shape is the "isolation", defined as $(E_T^{0.5} - E_T^{0.3})/E_T^{0.3}$, where $E_T^{0.5}, E_T^{0.3}$ are the transverse calorimeter energy contained in the 0.5 or 0.3 cone, respectively. A similar definition is used for charged tracks: "track isolation", defined as the sum of the transverse momenta of all tracks satisfying $|\Delta z_{\mathrm{DCA}}(\mathrm{track, tau})|$ <2 cm in an 0.5 $\eta - \phi$-cone around the tau cluster, which are not matched to the tau . These three variables are used in the selection of taus of all three types.
Additional variables that help discriminate τ_π-type taus are the angle between the track and the cluster and the transverse energy measured by the calorimeter divided by the transverse momentum of the track (E_T/p_T). These variables are plotted in Fig.3.6 for τ_π-type taus in signal ($Z^0 \rightarrow \tau\bar{\tau}$) and background (QCD) MC events and data with non-isolated muons, which consists primarily of background from $b\bar{b}$ -production.
For τ_ρ-type taus, two other variables can be used in addition. The first describes the isolation of the π^0 in the third layer of the EM calorimeter ("em3iso") and is defined as $E_T(EM_3)^{\mathrm{cluster}}/E_T(EM_3)^{\mathrm{tot}}$. The second is the invariant mass of the track and the (neutral) EM3-subcluster, which should be below the tau-mass of about 1.7 GeV. Figure 3.7 shows these variables for signal and background MC and for the background-dominated data of the sample with the non-isolated muon. For τ_ρ type taus E_T/p_T looses its discriminating power, hence, this variable is not considered for this tau type.
In three prong-type taus, the angle of the hadronic part of the cluster and the second track, as well as the number of tracks in a 30°-10°annular cone are used. In addition, the cluster energy divided by the track energy is considered. These variables are plotted for signal and background MC and non-isolated muon data in Fig.3.8. The tau identification variables for τ_π that distinguish background from data are well described by QCD MC. The description for τ_ρ is generally good, except for the distance of the leading track from the tau calorimeter cluster. This variable has a much larger tail in data than in background MC. This can result from the lower tracking efficiency in data compared to MC. In a number of cases in data the relevant $\pi^\pm$ track is not reconstructed and another random track is used to calculate Δ(track,cluster). This effect is reflected in the mass of the track and the EM cluster, since a larger ΔR between the track and cluster leads to larger invariant masses. For τ_{3pr} taus, the QCD Monte Carlo describes

the data well. As expected, one observes the tail at high values of ΔR here also.

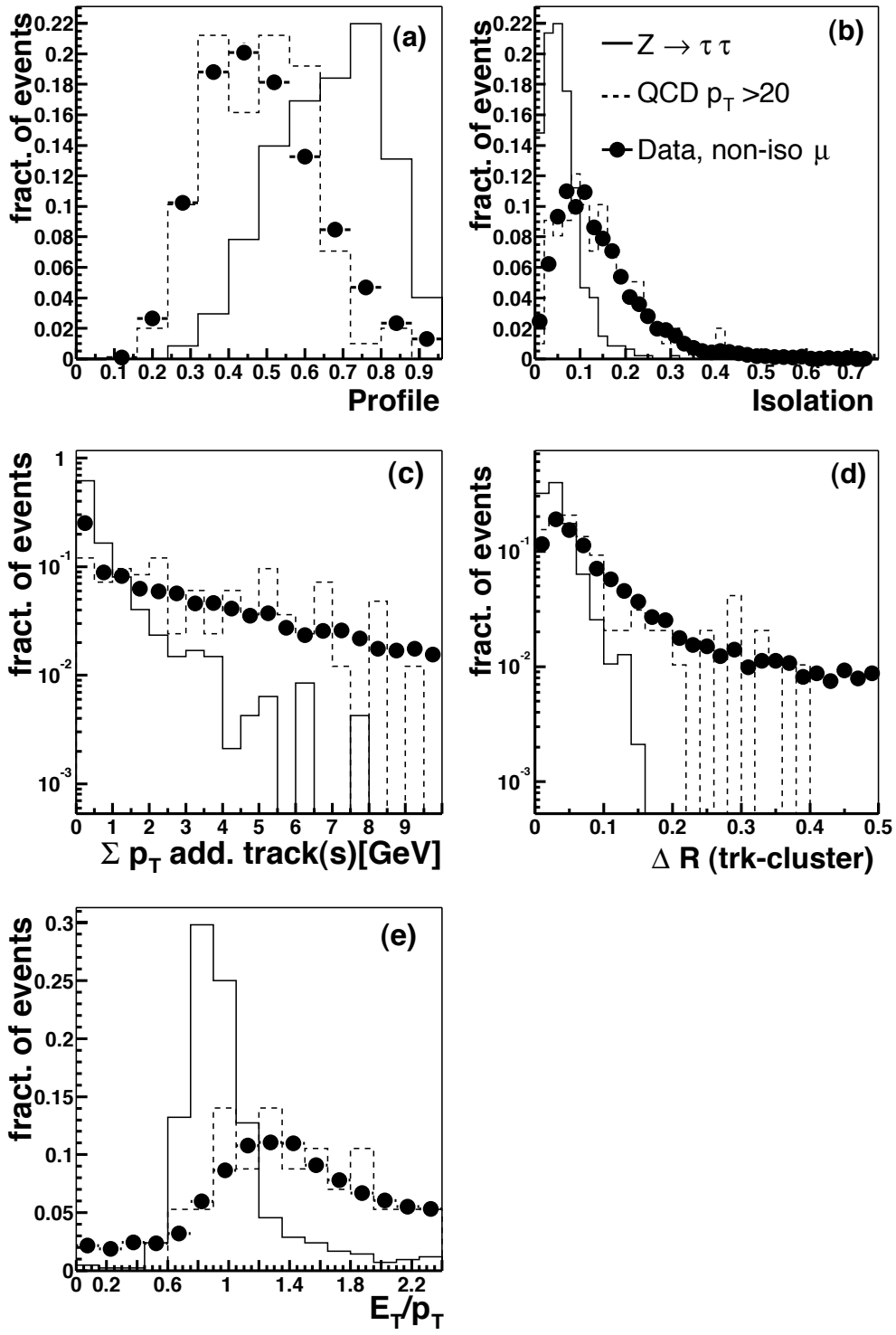

Figure 3.6: The distributions are for τ_π with 10< E_T^{rec} <20 GeV. Normalized distributions of $Z^0 \rightarrow \tau\overline{\tau}$ signal MC (full line), simulated QCD-jets (dashed line) and jets from non-isolated muon data (solid points) for the profile (a), isolation (b), track isolation (c), ΔR between track and cluster (d) and E_T/p_T (e). The curves are normalized to the same area.

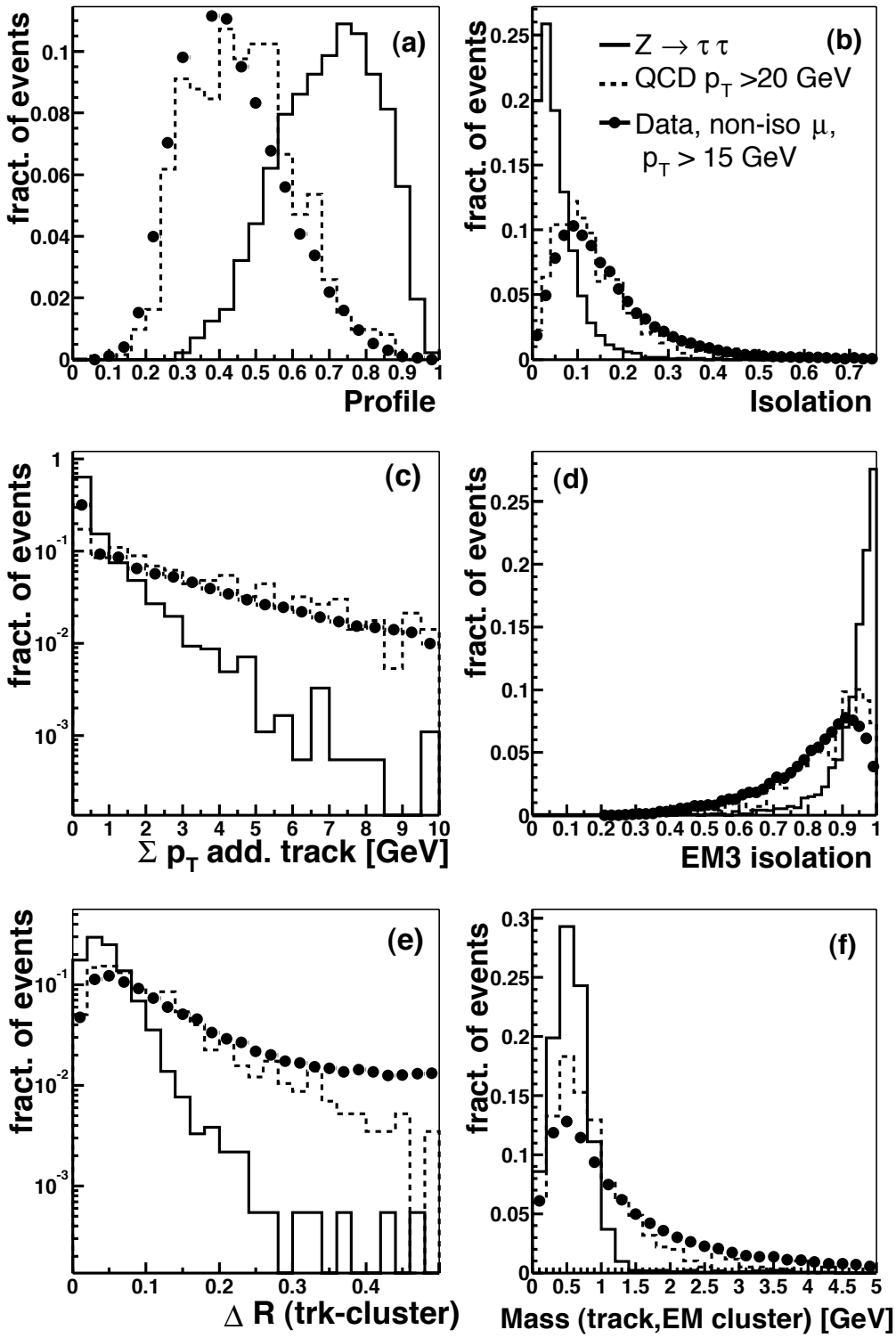

Figure 3.7: The distributions are for τ_ρ with reconstructed transverse energies between 10 and 20 GeV. Normalized distributions of $Z^0 \rightarrow \tau\bar{\tau}$ signal MC (full line), simulated QCD-jets (dashed line) and jets from non-isolated muon data (solid points) for the profile (a), calorimeter isolation (b), track isolation (c) as well as the isolation in the EM3 layer (d), ΔR of track and hadronic part of the cluster (e) and the invariant mass of the track and the EM-subcluster (f).

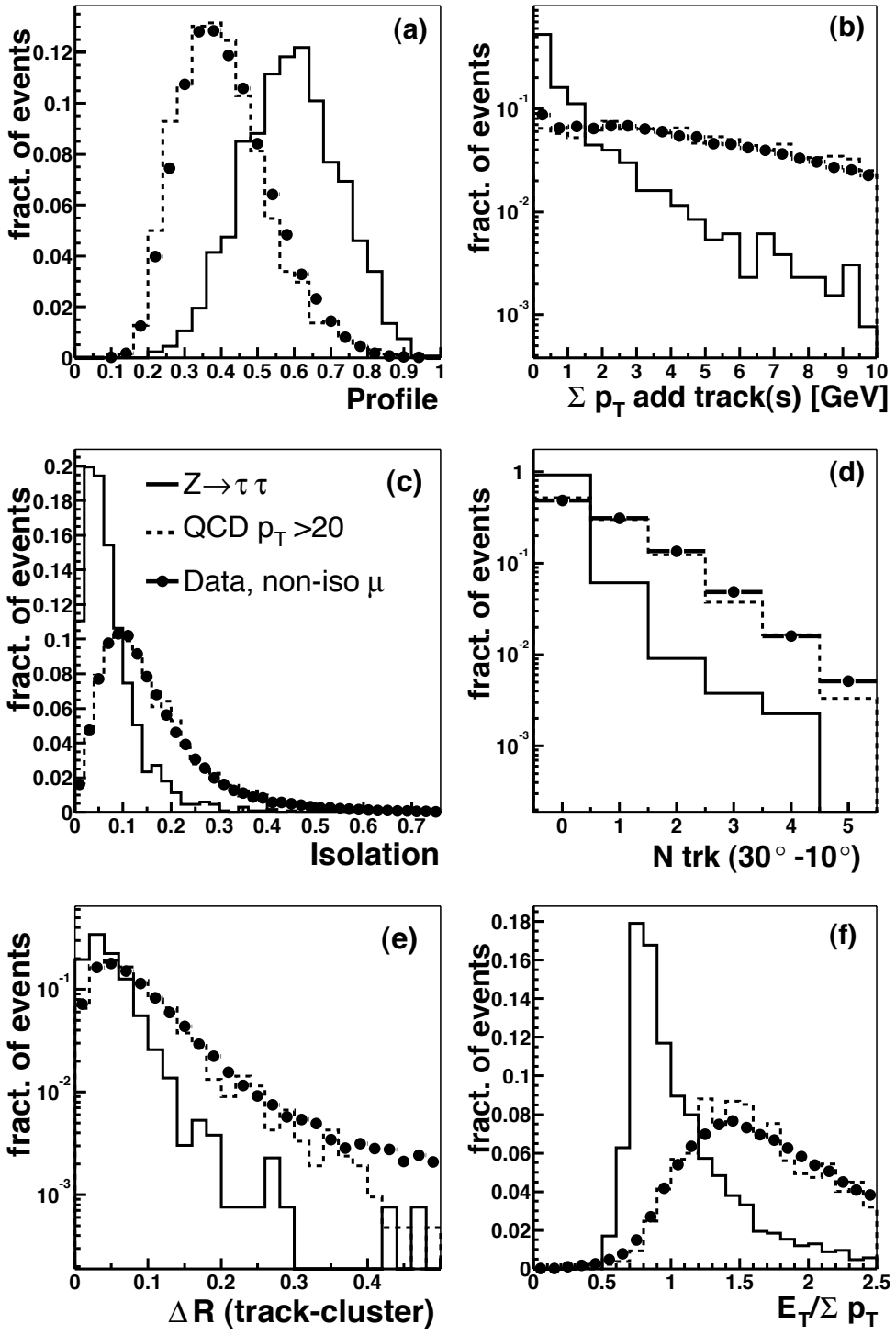

Figure 3.8: The distributions are for τ_{3pr} with 10< E_T^{rec} <20 GeV. Normalized distributions of $Z^0 \rightarrow \tau\bar{\tau}$ signal MC (full lines), simulated QCD-jets (dashed line) and jets from non-isolated muon data (solid points) for the profile (a), track isolation (b), calorimeter isolation (c) as well as the number of tracks in a hollow cone between 10° and 30° (d), ΔR of track and hadronic part of the cluster (e) and the ratio of the transverse cluster energy divided by the sum of the track momenta (f).

Chapter 4

Event Selection

The cleanest samples of tau leptons at the Tevatron are produced by the decay of the W and Z^0 vector bosons into $\tau\overline{\tau}$ and $\tau\overline{\nu}_\tau$, respectively. In contrast to the lighter leptons, the tau has a short lifetime, so only its decay products are measured by the detector. The tau branching fractions and $Z^0 \rightarrow \tau\overline{\tau}$ final states are summarized in Table 1.3.

Muons and electrons are experimentally well understood objects which can be identified with high efficiencies and low fakes rates. Hence, the leptonic tau decay is experimentally relatively easily accessible. In contrast, taus that decay hadronically appear as narrow jets and are thus more difficult to distinguish from background. This fact and the lack of a L1 track trigger for the data considered here, results in an absence of triggers suitable for hadronic taus. This necessitates the use of the mixed hadronic-leptonic final states to measure Z^0 bosons decaying into taus. In addition to a measurement of lepton universality, study of these tau decays results in an understanding of hadronic tau reconstruction with the DØ detector that will enable the use of tau leptons for a large number of analyses.

This chapter will treat the selection of $Z^0 \rightarrow \tau\overline{\tau}$ candidate events in the final states $Z^0 \rightarrow \tau\overline{\tau} \rightarrow \mu^-\overline{\nu}_\mu\nu_\tau\tau_{had}\overline{\nu}_\tau$ or $Z^0 \rightarrow \tau\overline{\tau} \rightarrow \mu^+\nu_\mu\overline{\nu}_\tau\tau_{had}\nu_\tau$, where τ_{had} is a hadronic final state of the τ. First the data quality criteria for runs used in this analysis are described, followed by the selection of muons and the hadronic final states. The trigger that is employed will be discussed and the optimization of the final selection cuts will be following a short discussion of the background for this step.

4.1 Data Set

The data used for this analysis were collected between September 2002 and May 2003 and have been reconstructed with `DØRECO` versions p13.05.00, r13.06.01 and p13.06.01. The integrated luminosity used for the $Z^0 \rightarrow \tau\overline{\tau}$ cross section measurement is 58 ± 6 pb^{-1}. For a dataset this size, the error on the measurement of the $Z^0 \rightarrow \tau\overline{\tau}$ cross section is dominated by the statistical error. For this reasons the treatment of the systematic errors in this analysis will be at a level commensurate with the statistical error.

4.1.1 Run Quality

Data quality information for offline analysis is available through a database, the "Offline Run Quality Database". There are seven quality categories: the quality of each large subdetector system (silicon tracker, central fiber tracker, calorimeter and muon system), where the quality of the L1 track trigger system was added from run 174426. In addition, the Jet/Met identification group defines criteria on which runs are rated for analysis using jets or the $\not\!\!E_T$ measurement. Currently, both of these ratings are the same.
The rating of the subdetector performance in a given run is based on the log-book entries. A run is called bad for a subdetector if e.g. crates are missing in the readout or if the data is compromised. Missing crates in the SMT readout can be caused by power supply problems or waterleaks, the data can be compromised if the detectors were not biased or the thresholds for the readout were downloaded incorrectly. For the calorimeter, runs are declared as "bad" if electronics was turned off by accident. In addition, from June 30 until mid August 2002, there were various levels of "mixed events", that means events where the readout of parts of the calorimeter crates originated in a different crossing. This effect cannot be corrected for yet, thus runs showing this problems are declared "bad". The run quality selection for the muon system is explained in detail in Ref. [95]. Runs are called "bad" for the muon system if crates are missing, if muon triggers are disabled or if the high voltage is off.
The quality assessment of the Jet/Met group is based on distributions of the reconstructed $\not\!\!E_T$. The three criteria used in the run selection from [96] are:

- the average scalar E_T of the run is > 80 GeV (in the range 100-120 GeV is normal),
- the mean shift of the $\not\!\!E_T$ $(= \sqrt{< \not\!\!E_{Tx} >^2 + < \not\!\!E_{Ty} >^2})$ is lower than 4 GeV where a clean run has a mean shift below 0.5 GeV, and
- the RMS of the $\not\!\!E_T$ distribution ($\sqrt{\sigma^2(\not\!\!E_{Tx}) + \sigma^2(\not\!\!E_{Ty})}$) has to be below 16 GeV (10 GeV is typical).

4.2 Trigger Selection

Events for the $Z^0 \rightarrow \tau\overline{\tau}$ cross section measurement in the $\mu\tau_{had}$ channel are selected by the MU_TAU10_L2M0 trigger. The L1 trigger (mu1ptxatxx) requires a muon anywhere in the detector, where only scintillator hits are required and no p_T threshold is applied. A medium muon at L2, as required by this trigger, has to have at least three PDT hits in both the A and BC layer for central muons. Muons in the forward region must have at least two MDT hits in the A layer with an additional pixel hit in the case of only two MDT hits and at least two MDT hits in the B or C layer. For the hadronically decaying τ, this trigger requires a L1 trigger tower with E_T above 5 GeV and a L3 τ with E_T above 10 GeV. In addition, a L3 track with p_T above 5 GeV is required. These requirements have been discussed before in sections 4.3, 4.4 and 4.5.
Here, matches of both a L1 calorimeter tower with E_T above 5 GeV and a L3 tau with E_T above 10 GeV to the tau candidate are required. This simplifies application of the trigger efficiencies for the calorimeter-based trigger terms, which are measured by matching an offline tau to

the trigger object, to obtain the trigger probability for the complete event. In addition, these requirements reduce the likelihood of noise faking a tau in the calorimeter.

4.3 Muon Identification

To obtain a clean sample of muons with as little background as possible, the requirements for the muon from the tau decays are a local muon of medium quality with a matched central track. Cosmic muons are rejected using the scintillator timing. The details of the muon reconstruction and quality requirements have been discussed in section 3.6.
Of importance for this analysis is the fraction of muons from τ decays that pass the trigger requirements and are subsequently reconstructed with the required quality. This muon efficiency can be separated into the following factors:

- ϵ(geom,p_T): the fraction within the geometrical acceptance of the detector, passing the p_T threshold,
- ϵ(reco): the fraction reconstructed in the local muon system of at least medium quality,
- ϵ(match): the fraction with a central track match,
- ϵ(L1), ϵ(L2): the fraction passing the requirements of the trigger at L1 and L2, and
- ϵ(timing): the fraction within the scintillator time window.

These efficiencies are not independent, so for the determination of the total efficiency the equation $\epsilon(A, B) = \epsilon(A|B) \times \epsilon(B)$ is used, stating that the efficiency for the requirement A and B is the efficiency for requirement B times the efficiency for A once B has been required. The efficiency can thus be written as:

$$\begin{aligned} \epsilon = \epsilon(\text{timing}|\text{L2}, \text{L1}, \text{match}, \text{reco}, \text{geom}, p_T) \\ \times \epsilon(\text{L2}|\text{L1}, \text{match}, \text{reco}, \text{geom}, p_T) \\ \times \epsilon(\text{L1}|\text{match}, \text{reco}, \text{geom}, p_T) \\ \times \epsilon(\text{match}|\text{reco}, \text{geom}, p_T) \\ \times \epsilon(\text{reco}|\text{geom}, p_T) \\ \times \epsilon(\text{geom}, p_T). \end{aligned} \tag{4.1}$$

The following subsections describe the determination of the efficiencies listed above.

4.3.1 Muon Acceptance

The coverage of the muon system extends to $|\eta_{det}|$ <2 and the support for the calorimeter necessitates a hole in the A-layer coverage for ϕ values from 225° to 310°. The reconstruction efficiency in a $Z^0 \to \mu^- \mu^+$ MC simulation is shown in Fig.4.1, with the chosen fiducial region indicated by thick lines.
Of the muons from the $Z^0 \to \tau\bar{\tau}$ decay (65.0 ± 0.2(stat) ± 0.25(sys))% are within the fiducial region of the DØ muon detector. Systematic studies for the geometrical acceptance as shifting

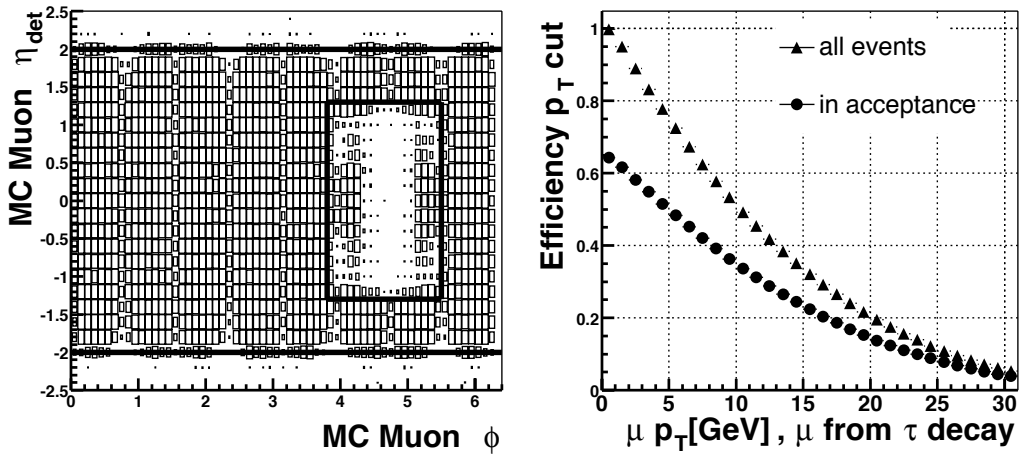

Figure 4.1: Muon acceptance from $Z^0 \to \mu^- \mu^+$ MC events: on the right a box-plot of the muon reconstruction efficiency, the lines indicating the fiducial region. A plot of the fraction of muons from $Z^0 \to \tau\overline{\tau}$ decays inside of the fiducial region versus the minimal p_T is shown on the left.

the positions of detector elements within errors have been performed for the cross section times branching fraction measurement of the W-boson decaying into muons and are described in [97]. The systematic uncertainty of the acceptance of 0.25% for that process and the decay of the Z^0 where only one "leg" of the Z^0 is subject to the muon acceptance is assumed to be the same.
The fraction of muons passing the p_T threshold is determined using MC. In order to take the momentum resolution of the tracking system into account, the p_T is smeared using the equation:

$$\frac{1}{p_T^{\text{gen}}} \to \frac{1}{p_T^{\text{gen}}}(1 + G\sqrt{A^2 P_t^2 + \frac{B^2}{\sin\theta}}), \tag{4.2}$$

where θ is the polar angle, G the width of a Gaussian distribution, B the multiple scattering term taken to be B=0.014584 and A the resolution term as expected from MC simulation. If f denotes the adjustment necessary to reproduce the measured Z^0 width in data, $A = 0.00162 * f$ with $f = 2.20 \pm 0.17$. The determination of the smearing function as well as the systematic error on the p_T cut can be found in ref. [97]. The function (4.2) used for the smearing changes the p_T distribution mostly at high p_T, no significant change of the acceptance due to the change in smearing parameters was observed. As a second cross check, the parametrization

$$\sigma\left(\frac{1}{p}\right) = \frac{\sqrt{(S\sqrt{\cosh\eta})^2 + (Cp)^2}}{p}, \tag{4.3}$$

with S=0.0146 and C=0.0029 from reference [98] was used. The nominal value for C is 0.00162. The value of the systematic uncertainty due to the p_T cut on the muon is estimated using the change in the acceptance value when varying the values for f within the errors in addition to half the difference of the two muon smearing parametrizations. The efficiencies for the acceptance and p_T cuts are summarized in Table 4.1.

An additional source of systematic uncertainty on the acceptance results from the ignorance about the parton distribution description. This uncertainty as estimated using two different descriptions: CTEQ5L which is used as default structure function for this analysis is compared to

p_T cut (GeV)	0	10	15
efficiency	0.650 ± .002 ± .002	0.340 ± .002 ± .002	0.225 ± .002 ± 0.003

Table 4.1: Efficiencies of the geometrical acceptance and the transverse momentum cuts.

events generated with Pythia using the MRST set of parton distribution functions. The resulting error is 0.06% The total systematic uncertainty on the $Z^0 \to \tau\overline{\tau}$ cross section measurement due to the acceptance and p_T cut at 10 GeV is 0.002.

4.3.2 Local Muon Reconstruction Efficiency

The L1 and L2 triggers for muons require scintillator and wire hits. These are used for the reconstruction of offline muons as well. Thus we must ensure that the measurement of the offline reconstruction efficiency is not biased by trigger requirements.

The method used to determine the reconstruction efficiency employs di-muon events from J/ψ and Z^0 decays. The first (tagging) muon is required to be of medium quality with a matched track. The events must pass a single muon trigger with a L2 muon requirement. The tagging muon has to match the L2 muon, leaving the other (test) muon unbiased. The candidate for the other muon is defined by a central track. Two different selections for central track candidates have been applied:

- the track has a muon like signature as confirmation in the calorimeter [89], or
- the track is of opposite charge and has a p_T above 6 GeV in the J/ψ peak region and above 10 GeV for the Z^0 and is isolated in the latter case.

The invariant mass distribution of the two central tracks, using the tagging muon and the second muon candidate, is fitted with a Gaussian for the signal plus a background function. The fitted number of signal events for the different event classes are used to extract the efficiency. The systematic error is estimated varying the shape of the background fit-function. The background in the J/ψ region with any requirement on the local muon is fitted with an exponential or a polynomial of fourth order. With medium, loose or tight quality requirement on the local muon track, polynomials of first or second order are sufficient to describe the background shape. The prescription for the background in the Z^0 region is a polynomial of first order in the range from 40 to 160 GeV. To estimate the systematic uncertainty introduced by this background description, an exponential function is used to fit the distribution in addition to the Gaussian for the signal. Figure 4.2 shows the J/ψ and Z^0 peaks for events with a medium muon having a track match and an oppositely charged track for the test muon. The reconstruction efficiency for local muons of loose, medium and tight quality are summarized in Table 4.2.

The reconstruction efficiencies in both samples agree within their statistical error. Dividing the sample in bins of p_T and η shows that the reconstruction efficiency is independent of both variables within errors.

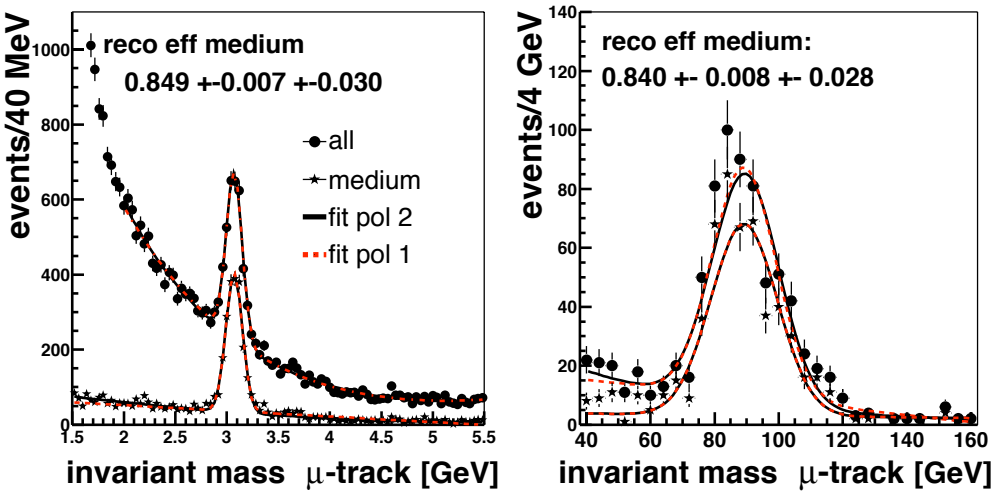

Figure 4.2: Invariant mass of the central muon tracks, for all events and events where the test muon passed the medium quality requirements for local muons. The left side shows the J/ψ-peak, where the track has to have a p_T above 6 GeV, the right plot the Z^0-peak with a 10 GeV cut and isolation requirement for the central track.

Sample	loose	medium	tight
calorimeter confirmed			
J/ψ	0.946 ± 0.007 ± 0.018	0.894 ± 0.010 ± 0.020	0.866 ± 0.011 ± 0.020
Z^0	0.961 ± 0.005 ± 0.023	0.848 ± 0.010 ± 0.020	0.827 ± 0.011 ± 0.020
charge and p_T selected			
J/ψ	0.929 ± 0.005 ± 0.035	0.849 ± 0.007 ± 0.030	0.821 ± 0.008 ± 0.030
Z^0	0.933 ± 0.006 ± 0.031	0.840 ± 0.008 ± 0.028	0.821 ± 0.008 ± 0.028

Table 4.2: Local muon reconstruction efficiencies, the first section is using the sample with a calorimeter confirmation for the muon track, the other section refers to the selection requiring oppositely charged tracks above 6 GeV for the J/ψ and 10 GeV for the Z^0 candidate events.

4.3.3 Muon Track Match Efficiency

The track match efficiency for central muon tracks is measured using a sample with two offline muons of medium quality. The events are required to have fired at least one trigger without a track requirement and to be of good quality for the muon and tracking systems. The sample is divided into events with zero, one or two track matches and the number of J/ψ and Z^0 events is extracted by fitting the fractions of two template histograms to the invariant mass distributions. The templates are derived from data using the sample with two track matches. The invariant mass of the two central tracks is used to divide the events into a signal and a background sample. The efficiency is calculated according to the formula:

$$\epsilon_{\text{trackmatch}} = \frac{2 * N_{2trk} + N_{1trk}}{2 * (N_{2trk} + N_{1trk} + N_{0trk})}. \tag{4.4}$$

The statistical error is deduced by varying the number of events in each class by the error on the signal fraction resulting from the fit. The systematic uncertainty is estimated by chang-

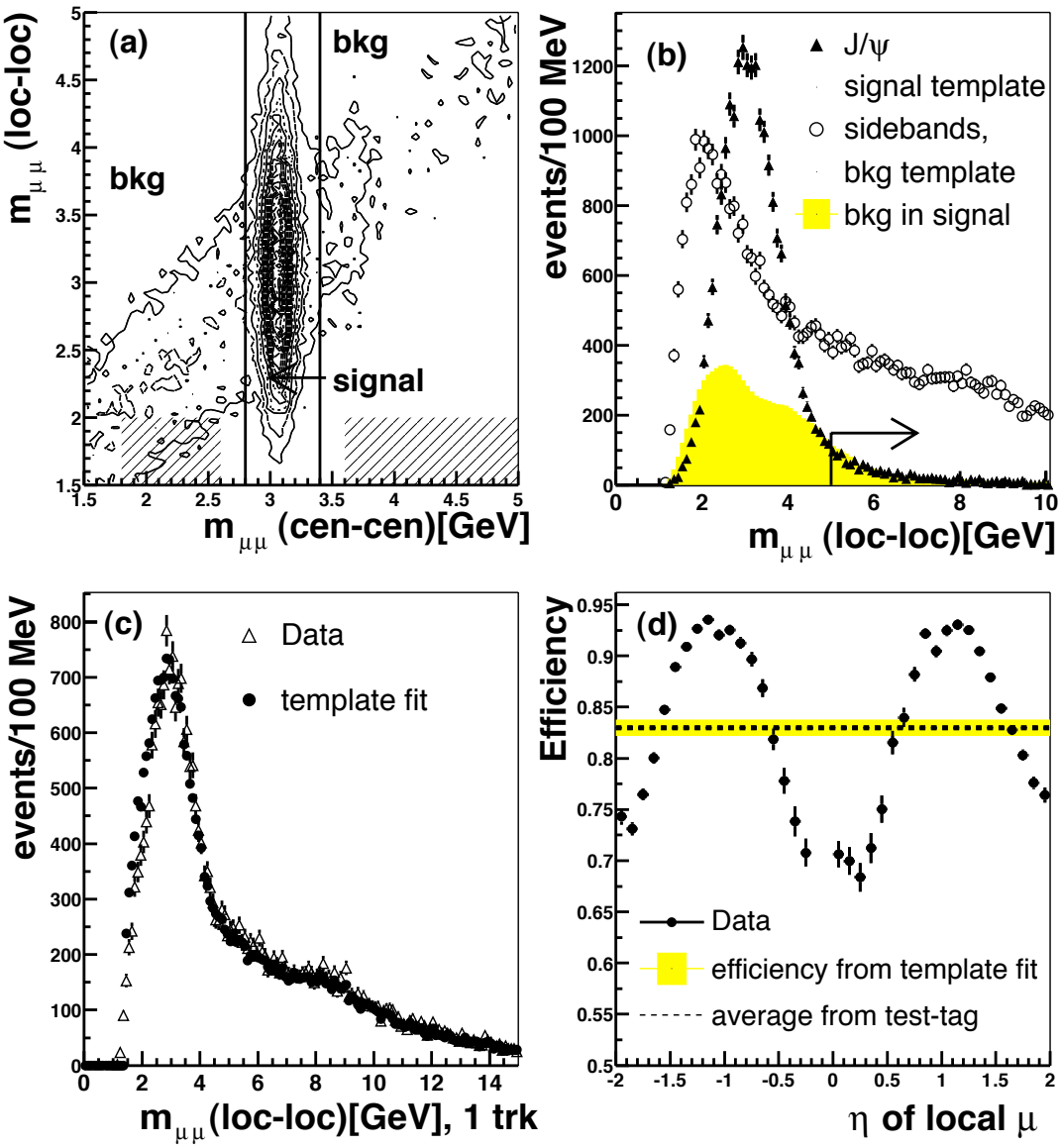

Figure 4.3: a) The invariant mass of the two central tracks versus the local-local mass. The central-central mass is used to separate the events with two tracks matched into b) a signal (peak events) and background (sideband events) template. The side bands are indicated in a) by the hashed area in the central-central invariant mass. The local-local invariant mass for exactly one track match is fitted with these templates, the fit is shown in c). In d) the efficiency as a function of η is shown, using events with a track matched muon, using the second one to measure the efficiency.

ing the signal template. The division into signal and background templates is shown for the J/ψ peak in Fig. 4.3 a). The templates are shown in Fig. 4.3 b). As indicated by the tail towards large invariant mass values for the signal template, the continuum contributes to events in the signal region. A template for the continuum background is obtained using events from sidebands in the muon-muon invariant mass in the ranges 1.8 GeV < $m(\mu\mu)$ < 2.5 GeV and

3.6 GeV < $m(\mu\mu)$ < 5. GeV. This template is scaled to have the same integral of events beyond 5 GeV as the signal template. This fit to the background is indicated by the gray shaded area in figure 4.3 b). The value of 5 GeV for the tail normalisation is chosen as the contribution of the central Gaussian to events with higher invariant masses is very small compared to the background. The corrected templates are then formed by subtracting the fitted background contribution from the signal template, and adding it to the background template. The normalizations of these two templates are then fitted to the invariant mass distributions of the two local muon in events with two, one or zero track matches. As an example, the distribution for one track match with the template fit is shown in Fig. 4.3 c). To estimate the systematic uncertainty resulting from the template choice, the fit is repeated using the uncorrected templates and half of the difference is used as an estimate of the systematic uncertainty.

To study the track match efficiency as a function of the muon p_T and η, at least one muon with a track match in the event is required. Events with a di-muon mass of the central and local track in the signal regions are used to plot the efficiency as a function of the local p_T and η. The efficiency as a function of η drops for values beyond the CFT coverage as expected. This can be seen in Fig. 4.3 d). In addition, there is a decrease in efficiency towards $|\eta|$=0 after a maximum around $|\eta|$=1.0. Central particles cross less sensitive material in the fiber tracker for smaller $|\eta|$, thus producing less photo-electrons translating into less efficient hit finding. The efficiency has been measured in two samples with very different p_T spectra for the muons. The track matching efficiency as a function of η agrees between both samples as well as the tracking efficiency integrated over η. For a range in η for which the tracking efficiency is to first order constant, the efficiency as a function of the p_T as measured in the local muon system is constant. The average value using the test-tag muon method is indicated by the dashed line, where the line-width indicates the statistical error. The gray band shows the efficiency measured using the template fit method, the width corresponds to the combined statistical and systematic error. The track match efficiency is measured to be 0.830 ± 0.004(stat) ± 0.007(sys) in the J/ψ sample. The measurement using the Z^0 resonance is considered as cross check and the track match efficiency is measured to be 0.817 ± 0.012(stat), in good agreement with the value from the J/ψ.

In the final cross section measurement, the tracking efficiency as function of η of the local muon will be applied. As a cross check, an average number will be used for the efficiency. The effect due to the dependence of the track match efficiency on η will be the same in $Z^0 \rightarrow \tau\overline{\tau}$ and $Z^0 \rightarrow \mu^-\mu^+$ events, thus the measurement using the template fit can be used as efficiency for the muons coming from di-τ events. This number is also the basis of the track matching efficiency for tau leptons as will be discussed in 4.4.3.

4.3.4 Muon Trigger Efficiency

To measure the efficiency for a muon of medium quality to pass the trigger requirements, an event sample triggered by a calorimeter only term is used. The presence of one medium muon inside the fiducial region with a matched central track is required and additional loose muons are vetoed.

To extract the L1 muon efficiency, the L1 And/Or terms for the different regions are checked. The global L2 muon trigger efficiency is determined by looking at the L2 bits that fired for events passing the L1 requirement. This efficiency is checked using global L2 muons matched to the

offline muon using an $\eta - \phi$ cone of 0.5. Both numbers agree if the efficiency of the L2-offline muon matching is taken into account.

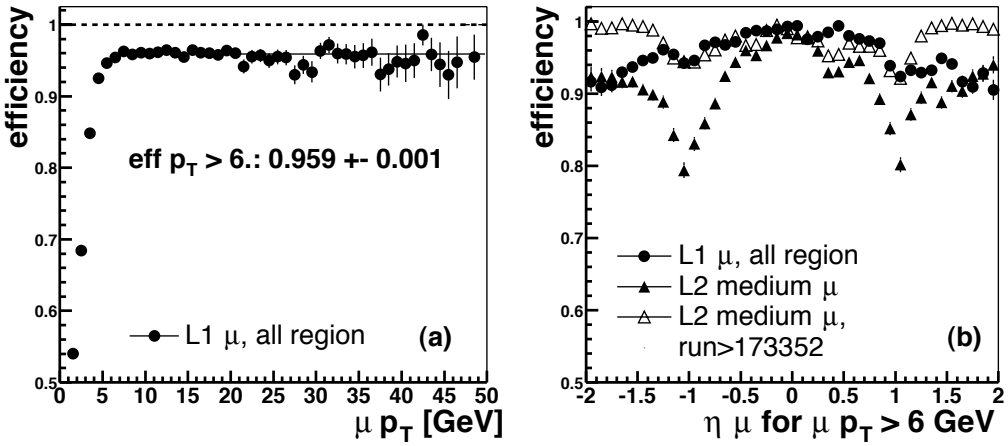

Figure 4.4: a) L1 efficiencies for local muons of medium quality; b) L1 and L2 muon trigger efficiency as a function of η.

The L1 efficiency is independent of p_T for the range considered in this analysis. For the muon trigger using the whole acceptance region ("all"), the L1 η dependence is not very strong. In contrast to this, the trigger efficiency at L2 drops strongly in the overlap region between the forward and central muon chambers as can be seen by the solid triangles in Fig. 4.4 b).
This efficiency problem for the L2 muon trigger was addressed by changes to the code running on the FPGAs active from run 173352 onwards. The efficiency for runs after these changes is shown in Fig. 4.4 b) by the open triangles.

Similar to the treatment of the tracking efficiency with its strong dependence on the pseudorapidity η, the trigger efficiency will also be taken into account as a function of η. To assess the size of this number and as a cross check, the efficiencies will be obtained by folding the L1 and L2 efficiencies as a function of η with the number of muons expected in the $Z^0 \rightarrow \tau\overline{\tau}$ decays from MC after reconstruction and track matching efficiencies. These numbers are summarized in Table 4.3. The trigger efficiencies are (96.0±0.8)% at L1, (91.5±0.1)% at L2 for a medium muon for runs before 173352 and (97.4±0.6)% after the FPGA code change. The

Efficiency in %	before 173352	after 173352
L1	0.960±0.007	0.960±0.007
L2	0.915±0.009	0.975±0.005
L1×L2	0.879±0.010	0.931±0.007

Table 4.3: Trigger efficiencies at level 1 and 2 for muons.

errors are combined statistical and systematic and are dominated by the limited statistics in data and MC. The systematic uncertainty due to selection of events of 0.4% used for the trigger efficiency measurement is estimated by dropping the track match on the test muon and adding the requirement of a "fast-z" trigger.

4.3.5 Timing Requirement

The time of a scintillator hit is measured with respect to the beam crossing time, corrected for the time the muon is expected to need to reach the detector. Figure 4.5 a) shows the timing of muons crossing the A-layer for muons with a central track match to reduce the contribution from cosmic muons. The distributions for all muons and for muons from Z^0decays are shown separately. In-time muons must have an A-layer scintillator time of $|t_{scint,A}| < 10$ ns and an

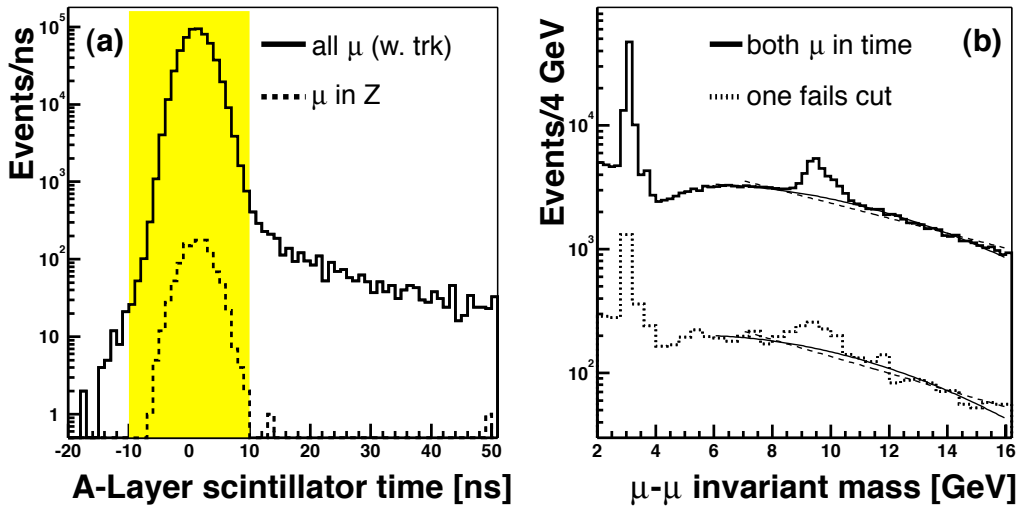

Figure 4.5: a) A-layer times for all muons with central track match on the right, the dashed line are muons from Z^0bosons. The gray region indicates the "in-time" region. The J/ψ-peak for both or one muon being inside of the timing window is shown in b). The full and dashed lines in b) are two different assumptions on the slope of the background.

outer scintillator time -15 ns $< |t_{scint,BC}| < 10$ ns. The tail of events with high values for the A scintillator time stems from cosmic muons. The efficiency of this requirement is measured using J/ψ, Υ(1S) and Z^0 di-muon events where both or one of the muons pass the timing requirements. The data is a "skimmed" subsample of all data requiring a medium muon, passing the timing cuts.
The invariant mass in the J/ψ peak region for di-muon pairs failing or passing the timing cut is shown in Fig. 4.5. The events are required to contain two medium muons with matched central tracks and to have fired the L1 di-muon trigger. The efficiency of the timing cut for each sample and the total number is given in Table 4.4.

Sample	Efficiency
J/ψ	0.9802 ± 0.0006
Υ(1S)	0.9718 ± 0.0014
Z^0	0.9836 ± 0.0029
total	0.9786 ± 0.0005

Table 4.4: Efficiency for the timing cut.

Using all three resonances the efficiency is measured as 0.979 ± 0.0005(stat) ± 0.006(sys) where the systematic uncertainty is estimated by varying the shape of the subtracted background (c.f. the full and dashed lines in Fig.4.5 b). As a cross check, the numbers from the three resonances are compared and half of the largest deviation is added in quadrature to the systematic uncertainty.

4.3.6 Summary of Muon Tagging Efficiencies

For the analysis presented in this chapter, the requirements on the muon are tight in order to suppress the large background present in this channel. The muon is required to pass cuts for a medium local muon with a central matched track. Events outside of the timing window are rejected. The efficiencies for those requirements and their uncertainty are summarized in Table 4.5.

Requirement	Efficiency ± (stat) ± (sys)
fiducial + p_T cut (10 GeV)	0.340 ± 0.002 ± 0.002
reconstruction	0.840 ± 0.008 ± 0.028
track match	0.830 ± 0.004 ± 0.007
L1×L2 trigger$_{<173352}$	0.879 ± 0.010 ± 0.004
L1×L2 trigger$_{\geq 173352}$	0.931 ± 0.008 ± 0.004
timing	0.979 ± 0.0005 ± 0.006
total$_{\text{accep,reco,time}}$	0.279 ±0.010
total$_{<173352}$	0.204 ± 0.008
total$_{\geq 173352}$	0.216 ± 0.008

Table 4.5: Efficiencies in the muon identification. The numbers are with respect to muons passing the preceeding requirements. The total efficiencies are obtained by folding the η dependent efficiencies with the η distributions of muons in signal MC.

The total efficiency for tagging the muon is 0.279 ±0.010, where the error is the combined statistical and systematic error. Including the average track matching and trigger efficiencies in the total efficiency, the overall efficiency is 0.204 ± 0.008 for runs before 173352 and 0.216 ± 0.008 thereafter. About 75% of the data sample considered here has been taken before run 173352.

4.4 Tau Identification

The efficiency to trigger, reconstruct and select hadronic taus can be separated into the following factors, in the order in which they will be determined:

- ϵ(geom): the fraction inside of the chosen geometrical acceptance,
- ϵ(reco): the fraction of taus leading to reconstructed tau clusters with an uncorrected $E_T > 10$ GeV in the calorimeter,

- ϵ(track): the fraction of reconstructed calorimeter tau cluster with a matched central track,
- ϵ(selection): the fraction passing the tau selection criteria, and
- ϵ(L1/3): the fraction passing the trigger requirements at level 1 and level 3.

The total efficiency can then be written

$$\begin{aligned}\epsilon = \epsilon(\text{L1} * \text{L3}|\text{selection}, \text{track}, \text{reco}, \text{geom}) \\ \times \epsilon(\text{selection}|\text{track}, \text{reco}, \text{geom}) \\ \times \epsilon(\text{track}|\text{reco}, \text{geom}) \\ \times \epsilon(\text{reco}|\text{geom}) \\ \times \epsilon(\text{geom}).\end{aligned} \tag{4.5}$$

Each of these factors will be treated in the following subsections. As taus are separated into different types, where "true" type and reconstructed type may differ, care must be taken to get the correct result when converting raw event yields into a cross sections.
The τ_π candidates passing both trigger and selection criteria can come from either true τ_π tau decays or from τ_ρ decays which were reconstructed without an EM3 sub-cluster. This can be expressed as:

$$\begin{aligned}N^{\pi}_{\pi,\text{measured}} = \sum_{p_T}(\epsilon^{\pi}_{\text{trigger}} * \epsilon^{\pi}_{\text{selection}} * (N_\pi * \epsilon_{acc} * \epsilon^{\pi}_{\text{reco,trk}} * f^{\pi}_{DY} * f(\pi \to \pi) + \\ N_\rho * \epsilon_{acc} * \epsilon^{\rho}_{\text{reco,trk}} * f^{\rho}_{DY} * f(\rho \to \pi))),\end{aligned} \tag{4.6}$$

$$\begin{aligned}N^{\rho}_{\rho,\text{measured}} = \sum_{p_T}(\epsilon^{\rho}_{\text{trigger}} * \epsilon^{\rho}_{\text{selection}} * (N_\rho * \epsilon_{acc} * \epsilon^{\pi}_{\text{reco,trk}} * f^{\pi}_{DY} * f(\pi \to \rho) + \\ N_\rho * \epsilon_{acc} * \epsilon^{\rho}_{\text{reco,trk}} * f^{\rho}_{DY} * f(\rho \to \rho))),\end{aligned} \tag{4.7}$$

where $\epsilon_{selection}$ and $\epsilon_{trigger}$ denote the efficiencies with which reconstructed tau candidates pass the selection and trigger criteria for its reconstructed type. The fraction of taus with true decay x to be reconstructed as type y is $f(x \to y)$. The correction to convert the number of Z^0 events to the number of di-tau pairs produced by Z^0/γ decays is denoted by f^x_{DY}, $\epsilon^x_{reco,trk}$ is the reconstruction efficiency, ϵ_{acc} the geometrical acceptance and N_x the number of taus of true type x.

As most of the factors in equations 4.6 and 4.7 depend on the momentum of the tau lepton, the final number of expected candidates for τ_π or τ_ρ are calculated using a summation over 10 p_T bins from 10 GeV to 60 GeV. The methods to acquire the efficiencies used in formulae 4.6 and 4.7 are presented below, the numbers quoted for each step are averaged over the p_T distribution from simulated signal events and are given to indicate the range of numerical values for these parameters.

4.4.1 Tau Acceptance

To eliminate taus that suffer from noise in the precision readout of the calorimeter, a match in $\eta\phi$ of the reconstructed offline tau and a L1 trigger tower above 5 GeV is required. The acceptance of the L1 calorimeter trigger for most of the data considered extends to $\eta = 2.4$. Since the

tracking efficiency drops for larger values of η and the effective tracking efficiency used here has been determined using muons with $|\eta|$ <2.0, the acceptance is further restricted to $|\eta|$ <2.0 to eliminate the dependence on unknown tracking efficiencies at large η.

Both the efficiencies for reconstruction, triggering and selection of tau candidates are lower in the ICD region. The description of the energy scale in the MC is poorer in this pseudo-rapidity region than for the central and endcap calorimeters. The acceptances for both $|\eta|$ <2.0 and $|\eta|$ <2.0 with the exclusion of 1.0< $|\eta|$ <1.4 are extracted from generator level Z^0 Monte Carlo events, in which a muon above 10 GeV transverse momentum is required. Table 4.6 lists the acceptances of the $|\eta| < 2$ cut with and without the ICD region for each tau type separately.

τ-type	$\|\eta\| < 2.$	$\|\eta\| < 1.$ or $1.4 < \|\eta\| < 2.$
τ_π	0.8398 ± 0.0059 ± 0.0036	0.6776 ± 0.0075 ± 0.0019
τ_ρ	0.8405 ± 0.0036 ± 0.0019	0.6800 ± 0.0046 ± 0.0013
τ_{3pr}	0.8428 ± 0.0051 ± 0.0047	0.6883 ± 0.0065 ± 0.0092

Table 4.6: Acceptances for hadronic taus in di-tau events with a muon above 10 GeV transverse momentum for two different acceptance regions in η.

The systematic error is a result of two sources. First the calorimeter position was shifted by ±2 cm in z with respect to the nominal position. The second and dominant part of the error results from the parton density function (pdf) uncertainties. Half of the difference in acceptances using two different sets of pdfs is used as an estimate for this.

4.4.2 Tau Reconstruction Efficiency

The reconstruction efficiency for taus is estimated using MC, since not enough data is available to measure this number from data alone. The transverse momentum distribution of hadronic taus inside the acceptance region in simulated $Z^0 \rightarrow \tau\tau$ events with a high p_T muon ($p_T > 10$ GeV) is folded with the efficiency of a tau to be reconstructed as a tau candidate with an uncorrected transverse energy above 10 GeV. This efficiency is plotted as a function of the true transverse momentum in Fig.3.2 in section 3.7. The energy scale for taus measured with the calorimeter is not well known at this time. It will ultimately be determined using data when larger tau datasets are available. To estimate the uncertainty on the reconstruction efficiency introduced by using the energy from the MC, the response is varied by $^{+5}_{-10}$% with a larger uncertainty of ±30% for taus in the ICD region. This uncertainty is derived from a comparison of the jet-energy response function in data and MC-events. It is conservative as differences in out-of-cone corrections will play much less of a role in the narrow showers produced by taus. The efficiency to reconstruct a tau with an uncorrected transverse momentum above 10 GeV and its errors are summarized in Table 4.7. The first error is the statistical error, the second, asymmetric error is the uncertainty resulting from the energy scale.

τ-type	all	$\|\eta\|$ <1. or 1.4 < $\|\eta\|$ <2.
τ_π	$0.643 \pm 0.009^{+0.016}_{-0.048}$	$0.648 \pm 0.009^{+0.016}_{-0.038}$
τ_ρ	$0.837 \pm 0.004^{+0.014}_{-0.051}$	$0.848 \pm 0.004^{+0.013}_{-0.038}$
τ_{3pr}	$0.908 \pm 0.004^{+0.014}_{-0.026}$	$0.914 \pm 0.005^{+0.014}_{-0.027}$

Table 4.7: Reconstruction efficiencies for hadronic tau decays. The efficiencies are quoted separately for each tau decay type and for different acceptance regions in η. The systematic error is due to the uncertainty of the energy response.

4.4.3 Tau Track Matching

As it is not yet possible to derive the track matching efficiency for taus from data, we will use the track matching efficiency measured in di-muon events, corrected for the matching efficiencies for muons and hadronic tau decay products. For muons, data are used and for taus the matching efficiency is measured in MC events.

The matching efficiency for tracks to local muons is obtained looking at $Z^0 \to \mu^- \mu^+$ events where no track match was found, but a high p_T track is found in an 0.5 cone around the muon [99]. In total, 52 out of 1228 muons without a track match in $Z^0 \to \mu^- \mu^+$ events have a track above 20 GeV in a cone of 0.5 around the muon. Using the track matching efficiency of (83.0±0.8)% measured before, this corresponds to a matching inefficiency of (0.7±0.04)%. The resulting tracking efficiency in data for η <2 is (83.7±0.8)%. This efficiency is lower than the tracking efficiency of (94.8±0.1)% found in simulated events. The effects of the matching cone and the minimal p_T requirement are taken from the MC and are illustrated in Fig.3.3 in section 3.7. This matching efficiency of nearly 100% has to be multiplied by the tracking efficiency.

In simulation, the dependence of the tracking efficiency on the hit pattern leads to a lower per-track efficiency in three prong tau decays than for isolated tracks. In contrast to the case of isolated tracks, where di-muon events can be used to measure the tracking efficiency in data independent from MC, no such means is available for three prong decays. This effect will lead to a large, difficult to estimate systematic uncertainty of the efficiency with which three prong decays can be identified, hence only one-prong decays will be used for the measurement of the $Z^0 \to \tau\bar{\tau}$ cross-section.

The fraction of three prong events being reconstructed as one prong and vice versa are estimated from the MC and corrected for the lower tracking efficiency in data. Most notably, about 10% of τ_ρ-type tau decays pick up an additional track from conversions. To account for the difference of the conversion rate in data and MC, this fraction has been varied by −5% and +25%. Both the efficiency of the tau to produce a track with a p_T above 1.5 GeV and the probabilities of taus to cross from *one prong* taus into the group of then disregarded *three prong* and vice versa depend on the p_T of the tau. This is taken into account by equations 4.6 and 4.7. The numbers given in Table 4.8 are given as illustration of the size of this effect and have been averaged over the expected p_T distributions of hadronic taus in di-tau events where the other tau decays into a muon with p_T above 10 GeV. The efficiency for each tau to be reconstructed as a tau cluster with an E_T above 10 GeV is included as well.

Efficiency in %	π	ρ
track matching efficiency (MC) (Δ R (MC), $p_T > 1.5$ GeV) tracking efficiency (data)	99.3±0.2 83.7±0.8	95.6±0.2 83.7±0.8
track match for τ	83.1±0.8	80.0±0.8
misidentification correction (MC+data)	0.5±0.7	$-5.2^{+0.6}_{-1.9}$
total	83.6±0.9	$74.8^{+0.9}_{-2.0}$

Table 4.8: Track-matching efficiency separated into the different sources. The 'misidentification correction is the net effect of 1-prong tau candidates having an accidental track matched to them and three prong taus with two lost tracks. The difference of the tracking efficiency in data and MC is taken into account. The uncertainty is the quadratic sum of the statistical and systematic uncertainty.

4.4.4 Drell-Yan Correction

The production of a lepton pair in the collision of two hadrons is a Drell-Yan process [100]. The intermediate boson can be either a photon or a Z^0-boson. As both processes have the same final state, the cross section has to be calculated using the sum of both matrix elements, giving rise to three contributions: the photon contribution, the Z^0 exchange contribution and the interference of both.

We are interested in the Z^0 exchange contribution only and in the following the correction factor to convert the number of measured di-lepton pairs into the Z^0 only cross section will be called "Drell-Yan" correction factor.
The size of this correction factor is estimated using generator level MC produced using Pythia. There, one can choose to generate the full Drell-Yan process for the production of tau pairs or only the Z^0 boson exchange. The distribution of the di-tau invariant mass in both cases is shown in Fig.1.2. The correction factor is 1.00±0.02±0.01 for τ_π taus and 1.02±0.01±0.02 for τ_ρ taus. The systematic error is estimated by varying the parton distribution functions.

4.4.5 $\pi \leftrightarrow \rho$ Confusion

As explained in section 3.7, taus decaying into a single charged pion can be reconstructed as a τ_ρ type tau candidate if they shower early in the calorimeter and leave enough energy so that a subcluster above 0.8 GeV in the third layer of the calorimeter can be reconstructed. Similarly, if a tau decays into a charged pion accompanied by one or more neutral pions, and there is not enough energy left in the EM layers of the calorimeter, they can get reconstructed as τ_π tau. This is often the case for taus in the ICD region.

The efficiencies discussed up to this point are treated with respect to the true tau decay. The trigger efficiency will be deduced from data, thus separated according to the reconstructed tau type. The selection cuts are defined considering the reconstructed tau type and not the "true" decay which is unknown in data. To obtain the correct efficiency for taus reconstructed as τ_π taus, the effect of the type mis-identification has to be taken into account. This is done in equations 4.6 and 4.7. The *confusion* or *mis-identification* factor depends on both the transverse

energy of the tau and the acceptance region as illustrated in Fig.4.6. The factors $f(\pi \to \rho)$ and $f(\rho \to \pi)$ are the complements of $f(\pi \to \pi)$ and $f(\rho \to \rho)$, respectively.

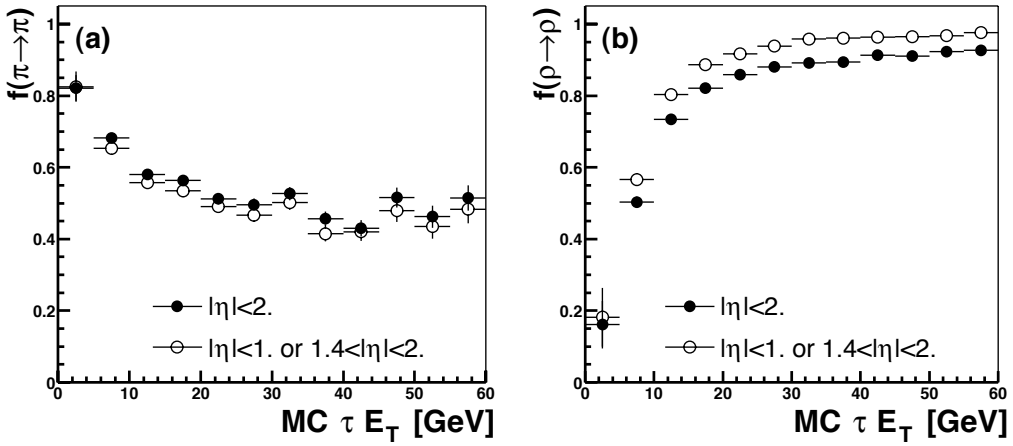

Figure 4.6: $f(\pi \to \pi)$ non-confusion factor for MC τ_π taus in (a) and $f(\rho \to \rho)$ MC τ_ρ taus in (b) as a function of the MC visible transverse energy.

A source of systematic uncertainty for the $\pi \leftrightarrow \rho$ confusion factors is the energy scale for electromagnetic objects as a subcluster must pass an E_T threshold of 0.8 GeV. The electron energy in MC must be re-smeared with the equation

$$E_{MC}^{\text{smeared}}(E_{MC}) = (A \cdot E_{MC}) \cdot \left(1 + e^{-E_{MC}^2/2B^2)}\right), \tag{4.8}$$

with A = 1.0 and B= 0.047 for electrons outside of the cracks between the calorimeter modules and A = 0.95 and B= 0.05 for electrons outside of the fiducial region [101]. This will only have an effect on subclusters just around the E_T threshold. From simulated $Z^0 \to \tau\overline{\tau}$ events, this energy correction has an effect of less than 0.1% on the τ_π confusion fraction and 0.03% on the τ_ρ confusion fraction. To be conservative, a systematic uncertainty of 0.2% is used.

4.4.6 Offline Tau Selection Efficiency

For this analysis, simple cuts on a number of variables are used. These variables have been described in section 3.7. Cuts to select loose and tight tau candidates have been determined for all three tau types and are described in [102]. For the selection of hadronic taus from the $Z^0 \to \tau\overline{\tau}$ process, the background is large. Hence the tight selection of tau candidates as in [102] will be used as a starting point to optimize the cuts. The cuts and efficiencies of the tight tau candidate selection will be described here, the optimization of the cuts will be discussed later in 4.8. For the tight selection, all variables mentioned in section 3.7 are used. Plots where all cuts but the one illustrated are applied are shown in Fig.4.7 for τ_π and in Fig.4.8 for τ_ρ types. The τ_{3pr} tau decays will not be used here, for the selection of this type of tau decay, the reader is referred to reference [102].

The efficiencies for each tight selection cut in a sample where all other cuts have been applied are summarized in Table 4.9. The cut on the E_T/p_T-like variables has been applied only after all other cuts. The most powerful cut is the track isolation requirement. This cut has

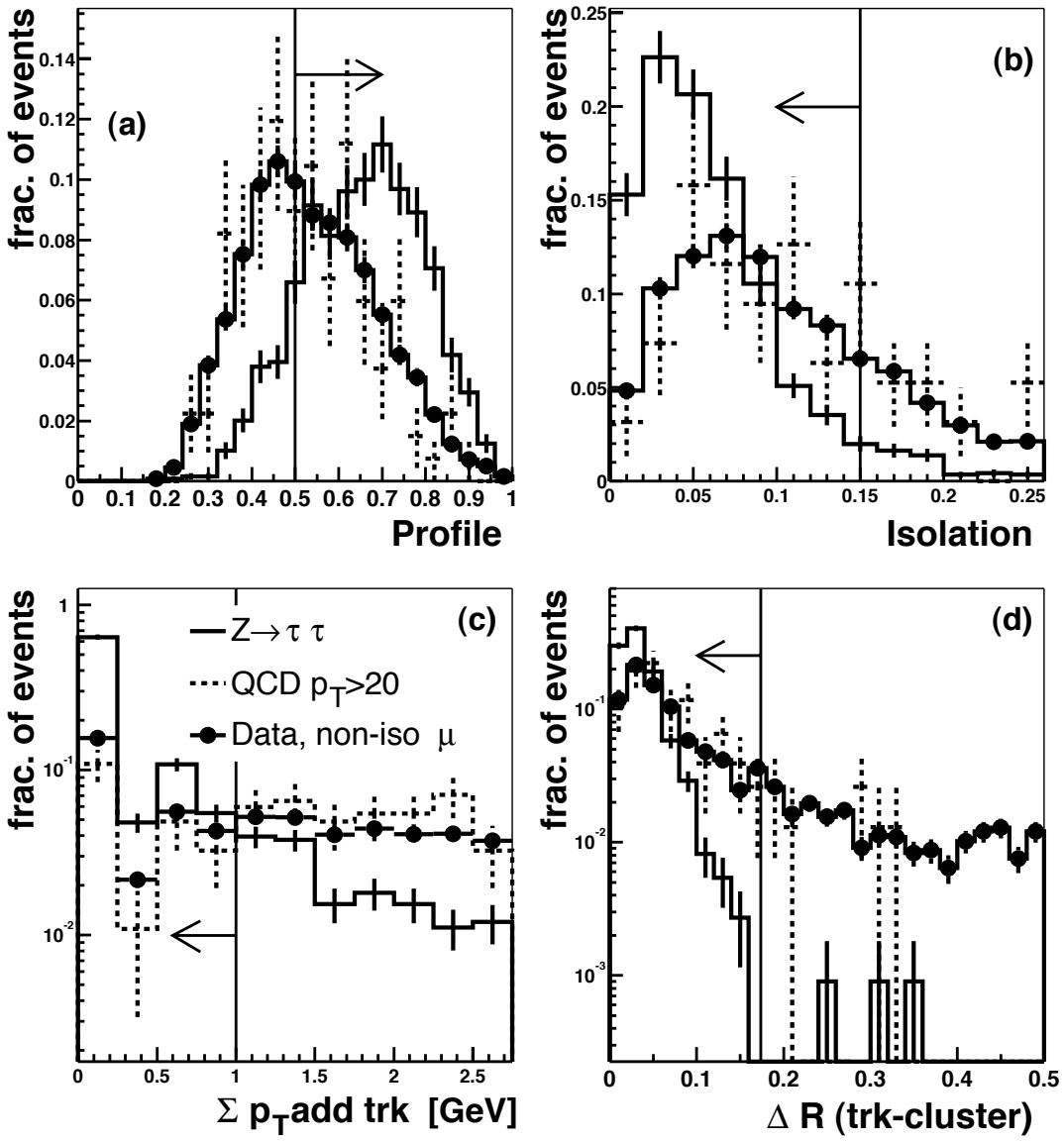

Figure 4.7: Tight selection cuts for τ_π-type taus. All cuts except for the one illustrated have been applied. Signal MC is indicated by the full line, the dashed error bars show QCD MC and the full dots are data. Plot a) shows the profile, b) the isolation, c) the track isolation and d) the angle between track and tau cluster. The curves are normalized to unity.

an efficiency of above 90% and rejects more than 50% of the background, even after all other cuts have been applied. The largest source of inefficiency is due to the cut on the profile and the E_T/p_T cut in the τ_π case. These cuts also have a high rejection rate on the order of 50%. This fact in combination with the shape of the profile distribution makes this variable a natural indicator for signal presence in a sample after all other selection cuts have been applied. The total efficiencies for the tight selection with and without a cut on an E_T/p_T-like variable can be found in Table 4.10.

The systematic error on the final tau selection efficiency separates into three components.

Cut N-1	$Z^0 \to \tau\bar{\tau}$ MC	QCD MC	Data, non-isolated μ
π			
$\sum p_T$ add trk	0.90	0.38	0.37
Isolation	0.93	0.73	0.73
Profile	0.85	0.51	0.56
ΔR trk-cluster	1.00	0.90	0.81
E_T/p_T	0.84	0.48	0.42
ρ			
$\sum p_T$ add trk	0.98	0.43	0.43
Isolation	0.96	0.80	0.80
Profile	0.93	0.57	0.53
ΔR trk-had. cluster	0.99	0.88	0.82
EM3 isolation	0.98	0.91	0.88
inv. mass (em cluster-trk)	0.97	0.99	0.965
$(E_T^{EM} + p_T^{trk})/p_T^{trk}$	0.98	0.88	0.78

Table 4.9: Efficiency of the selection cut after all other cuts have been applied. These numbers are illustrative, hence no uncertainties have been determined.

	Selection	$Z^0 \to \tau\bar{\tau}$ MC	QCD MC	Data, non-isolated μ
	π			
τ_π	Tight cuts	0.661 ± 0.011	0.051 ± 0.006	0.055 ± 0.002
cand.	+ E_T/p_T	0.546 ± 0.011	0.024 ± 0.004	0.024 ± 0.001
all	Tight cuts (all)	0.0952 ± 0.0026	0.0029 ± 0.0004	0.0039 ± 0.0002
τ	+ E_T/p_T	0.0787 ± 0.0024	0.0014 ± 0.0002	0.0017 ± 0.0001
	ρ			
τ_ρ	Tight	0.676 ± 0.006	0.054 ± 0.003	0.045 ± 0.001
cand.	+ $(E_T^{EM} + pT^{trk})/pT^{trk}$	0.664 ± 0.006	0.047 ± 0.003	0.035 ± 0.001
all	Tight (of all)	0.337 ± 0.004	0.011 ± 0.001	0.011 ± 0.001
τ	+ $(E_T^{EM} + pT^{trk})/pT^{trk}$	0.331 ± 0.004	0.010 ± 0.001	0.008 ± 0.000

Table 4.10: Efficiencies for the certified, tight selection of tau candidates. The efficiencies are given as fraction of the candidates of the specific type and of all tau candidates.

One is the uncertainty from the difference between tracking efficiency in data and MC, which may change the efficiency of the track isolation cut. To estimate this, the track isolation cut is studied in Z^0 decays into muons in data and simulated events. The efficiency for a cut at 1 GeV is found to be 0.910±0.007 and 0.918±0.004 in data and MC, respectively. A second effect comes from the energy scale. The jet energy scale correction in data is about 10% higher than in MC, i.e. cuts on E_T/p_T-like variables requiring E_T/p_T to be below the chosen cut value are more efficient for data than for MC. This effect is taken into account by varying the

energy scale in MC by 10% and using the difference of both efficiencies as error. After applying all π-type selection criteria with the exception of E_T/p_T, the efficiency in MC is 0.911±0.009 and 0.845±0.012 with and without the scale variation respectively. The effect of modeling of the transverse shower shape in the Monte Carlo is more difficult to determine. Comparing the shapes for tau candidates from QCD in data and MC and the fake rates in both data and MC indicate that this effect is small. As a cross check, the number of background-subtracted events ("opposite sign(os)−same sign(ss)") in data are plotted versus the profile cuts for three different isolation cuts in Fig.4.9. In the left plot, the profile distributions and their integral for the three isolation cuts are shown. The integrated number of signal events corrected for the efficiency expected from MC is shown in the right plot. The curves for the three different isolation cuts agree with each other and are flat within errors. Thus with the available statistics in data, there is no visible systematic effect resulting from MC-data discrepancies concerning the lateral shower shape.
The total systematic uncertainty on the selection efficiency is assumed to be 6.7% for the π-type candidates and 0.9% for the ρ-candidates. The latter systematic uncertainty is smaller since the selection does not cut on the energy scale dependent E_T/p_T variable.

4.4.7 Tau Trigger Efficiency

Tau triggers exist at trigger levels 1 and 3. At L1, a trigger tower is required to have a transverse energy above 5 GeV. The L3 tau tool requires a 0.7 cone jet with E_T above 10 GeV that passes loose requirements on the shower shape. At the presently collected integrated luminosity, there are not enough taus present in data to determine the trigger efficiency using only these objects. The chosen strategy is to create a sample of "tau-like" jets from background events. Events are selected with a non-isolated muon passing a W$\rightarrow \mu\nu_\mu$ trigger which requires a muon at L1 and L2 as well as a L3 track. The data is thus unbiased for triggers requiring calorimeter terms at L1 and L3.
The tau trigger for the data period considered only uses calorimeter information. To obtain a sample of jets that are "tau-like", a reweighting method has been chosen. The events are given a weight based on their profile and cluster width (rms) value:

$$wt = \frac{\mathrm{N}_{MC\tau}(\text{profile, width})}{\mathrm{N}_{data}(\text{profile, width})}. \tag{4.9}$$

Figure 4.10(a) shows the profile versus the cluster width for signal $Z^0\rightarrow\tau\bar{\tau}$ and (b) for background QCD MC events. Figure 4.10(c) shows the profile distributions for both MC samples and data, both with and without re-weighting. The QCD MC describes the un-reweighted data very well. The reweighted distribution matches the expectation from signal. The same is true for the cluster width.

- **L1 CJT(1,5)** : The L1 calorimeter trigger for taus should have a sharper energy turn-on than for jets, since the energy is concentrated in a few towers for taus while the energy deposition of jets is more diffuse.
  Figure 4.10(d) shows the trigger turn-on curves for the level 1 tau trigger for events with a neutral sub-cluster. The turn-on for background is slower than the curve obtained using the re-weighted events. Figure 4.10(e) shows the trigger efficiency versus η_{det} for taus

with p_T above 15 GeV. For τ_π, the efficiency drops for clusters that are reconstructed in the ICD region. This is expected as the ICD energy readout is not used in the L1 calorimeter trigger. The τ_ρ in the same region have by definition a fraction of their energy deposited in the electromagnetic calorimeter which reduces their energy fraction sampled in the intercryostat detector.

- **L3** τ : The trigger efficiency for the L3 tau tool is measured using the same sample as for the L1 trigger efficiency. In Fig.4.10 (f), the efficiency is plotted versus the reconstructed tau p_T for events passing the L1 requirement. The plateau efficiency for both data (background) and the re-weighted sample are considerably below one. This is due to the shape cuts at level 3. As the cuts have been loose, the plateau efficiency of signal-like data and the background are not very different.

The efficiencies, as summarized in Table 4.11, are determined by folding the τ_π-p_T distribution in events with requiring a muon above 10 GeV. To estimate the effect of the trigger efficiency, equations 4.6 and 4.7 have been used. When the summation over p_T is performed, the number of π candidates expected from MC and the efficiencies as measured from MC are given as a function of the true visible pion E_T. In contrast to that, the tau trigger efficiency is measured from reconstructed tau candidates and is thus given as a function of the reconstructed tau E_T. From a study of the tau resolution performed on MC in section 3.7.4, a shift of -2.5 GeV is expected from the true visible E_T to the reconstructed E_T. This shift is taken into account in the application of equations 4.6 and 4.7. The systematic uncertainty of the shift value is assumed to be the same as its magnitude, 2.5 GeV. Its effect on the trigger efficiency is estimated by shifting the trigger efficiency curve by -5 GeV and 0 GeV.

The quoted error is the sum of the statistical error from data and the systematic uncertainty. The statistical errors are of $O(10^{-5})$, hence the total error on the tau trigger efficiency is dominated by the systematic uncertainty from the energy scale.

τ type	L1	L3	L1*L3
τ_π	$0.88^{+0.04}_{-0.06}$	$0.72^{+0.04}_{-0.06}$	$0.65^{+0.05}_{-0.07}$
τ_ρ	$0.95^{0.01}_{0.02}$	$0.72^{+0.02}_{-0.04}$	$0.69^{+0.04}_{-0.03}$

Table 4.11: Trigger efficiencies and their uncertainty, separately for tau candidates with and without EM3 sub-cluster.

4.4.8 Tau Reconstruction and Selection Summary

The various efficiencies for tau reconstruction are summarized in Table 4.12. For the numbers quoted in this table, the selection cuts were optimized for the cross section measurement. The cut optimization will be explained in section 4.8. The efficiencies are given with respect to the number of expected events after all preceding requirements. The statistical errors are obtained by varying the efficiency by $\pm 1\sigma$ in each of the 10 bins in p_T from 10-60 GeV separately. The variance of these 10 variations is used as estimator for the uncertainty caused by the statistical uncertainty of the given efficiency. To account for the systematic uncertainties of the measured

efficiencies, the efficiencies in all bins are varied by $\pm 1\sigma$ at once and the shift for the efficiency is used as estimate for the systematic uncertainty. The uncertainty resulting from the measurement of the tau trigger efficiency is treated as explained in section 4.4.7. The effect of the energy scale uncertainty is estimated using the reconstruction efficiency as function of p_T assuming a shift in the energy scale of $^{+5}_{-10}$% with special treatment of the ICD region. The systematic error from the MC statistics is estimated by dividing the sample into ten subsamples of equal size. The variance of the efficiencies divided by $\sqrt{10}$ is used as estimate for the uncertainty.

The efficiencies given in the last line of Table 4.12 are the efficiencies to select a $Z^0 \to \tau\overline{\tau}$ event with a muon above 10 GeV as a τ_π or τ_ρ tau event, respectively.

	τ_π	τ_ρ
$\epsilon_{\text{total}}, \lvert\eta\rvert < 2.$	$0.840\ ^{+0.0072}_{-0.0058} \pm 0.0002$	$0.841\ ^{+0.0055}_{-0.0044} \pm 0.0005$
$\epsilon_{\text{reco}}^{\text{pT>10GeV}}$	$0.639 \pm 0.05^{+0.008}_{-0.029}$	$0.838 \pm 0.005^{+0.006}_{-0.025}$
one prong	$0.835 \pm 0.002^{+0.008}_{-0.011}$	$0.748 \pm 0.002^{+0.007}_{-0.013}$
Drell-Yan correction	$1.018 \pm 0.014 \pm 0.010$	$1.021 \pm 0.009 \pm 0.02$
fraction $\tau_x \to \tau_x$	$0.969 \pm 0.002^{+0.0}_{-0.11}$	$1.010 \pm 0.0006^{+0.0}_{-0.003}$
$\epsilon_{\text{selection}}$	$0.801 \pm 0.017 \pm 0.066$	$0.676 \pm 0.009 \pm 0.009$
$\epsilon_{\text{trigger}}$	$0.643 \pm 0.00002^{+0.046}_{-0.061}$	$0.686 \pm 0.00005^{+0.02}_{-0.033}$
$\epsilon_{\text{reco,sel}}$	$0.228\ ^{+0.032}_{-0.026}$	$0.256\ ^{+0.017}_{0.010}$
BF (rel. hadronic)	0.181 ± 0.002	0.570 ± 0.002
ϵ_{total}	$0.041^{+0.006}_{-0.005}$	$0.146\ ^{+0.010}_{0.006}$

Table 4.12: Summary table of efficiencies for tau reconstruction and selection.

4.5 L3 Track Trigger Efficiency

The only remaining efficiency which has not been discussed in the muon or tau selection sections is the trigger efficiency connected to the track trigger at level 3, where a track with a transverse momentum above 5 GeV is required.

To measure the L3 tracking efficiency, a sample of $Z^0 \to \mu^-\mu^+$ events has been selected and the response of the L3 track trigger has been simulated. The efficiency of a central muon track to be reconstructed as track at L3 is shown as a function of η and p_T in Fig. 4.11. Shown in addition is the probability with which the tracks in the underlying event can lead to a L3 track above 5 GeV. The L3 track efficiency drops with p_T of the considered track. The efficiency for central muon tracks above 25 GeV, where the bulk of $Z^0 \to \mu^-\mu^+$ muons lies, is (74.3±0.011)% and drops to about 60% for lower p_T tracks. For this analysis, the medium quality muon is required to have a central track with p_T above 10 GeV. Both the muon and the tau are restricted to $|\eta| < 2$, while the acceptance for L3 tracks extends only to $|\eta| < 1.6$. For a subset of events, there will be an additional track above the L3 threshold from the tau. In addition, the underlying event can produce a L3 track above threshold.

The efficiency for the event to satisfy the L3 track trigger condition is estimated using signal MC events, taking the probabilities for the muon and the tau to fire the trigger correctly into account considering their η and p_T values and adding the probability that the underlying event produces a 5 GeV L3 track. The efficiency for the L3 track trigger to fire is $0.80\pm0.02^{+0.05}_{-0.00}$ for τ_π taus and $0.78\pm0.02^{+0.05}_{-0.00}$ for τ_ρ taus.
The sample of lower p_T tracks in a $Z^0\rightarrow\mu^-\mu^+$ event can have contributions from fake tracks and thus, the L3 track efficiency for real tracks can be underestimated. To estimate the size of this effect, the efficiency for high p_T muon tracks is used for all tracks and half of the difference is used as estimate of the systematic uncertainty.

4.6 Muon Isolation

In signal events, the muon is generally isolated. Hence, a sample with non-isolated muons contains dominantly fake τ. These events can come from $b\bar{b}$ production with at least one b decaying semi-leptonically into a muon. A second possibility is production of light quarks, where one of the $\pi^\pm$ or $K^\pm$ produced in the fragmentation decays into a muon. As the separation of the signal and background samples relies on the μ isolation, this variable is crucial. There are two systems that independently measure the μ isolation: the calorimeter measures the MIP trace of the muon and the energy of all particles from an accompanying jet, and the tracking system which determines the momenta of the muon and the other charged particles in the jet.

Naively, isolation could be defined as the distance to a jet passing the jet selection criteria, but that fails to account for low energy jets that do not pass the reconstruction threshold and muons where the calorimetric energy fluctuates up so that the muon trace creates a jet. A variable taking the muon energy better into account can be constructed using the energy summed in different cones around the muon direction. The energy deposition of the muon is mostly contained within an inner cone of small radius. The best discrimination between signal and background is achieved when cutting on the transverse energy in a cone around the muon with radius R=0.4 in $(\eta-\phi)$ space after subtracting the core energy contained in an inner cone of radius R=0.1. For details of this optimization, the reader is referred to reference [103]. Tracks can be treated similarly. In this case the size of the inner cone does not need to be optimized as the central track belonging to the muon is determined by the best track match. The transverse momentum of all other tracks in a 0.5 cone are summed up to give an isolation variable based on tracks.

To determine which variables provide the best separation between truly isolated muons from the decay of electroweak bosons and those coming from QCD, a signal sample of isolated muons is taken from Z^0 decays into muons in data, requiring two muons of medium quality with matched central tracks and an invariant mass of those tracks between 65 and 115 GeV. An inclusive sample of muons in events with missing E_T below 10 GeV is used as background sample. This sample is completely dominated by events with muons in jets. Looking at the energies in cones around the muon, no sign of signal contamination is observed. Figure 4.12(d) shows the fraction of events with single muons passing the isolation requirement of (max(trkiso, E_T^{Halo}) <2.5 GeV) as a function of $\not\!\!E_T$. For high values of $\not\!\!E_T$ the sample is dominated by W decays into muons, which is reflected is the high fraction of isolated muons. The isolated muon fraction drops with $\not\!\!E_T$, becoming constant below 15 GeV.

Figure 4.12(a) shows the distribution of the track-based isolation variable and the calorimeter isolation is shown in Fig.4.12(b). The efficiency versus rejection curves for the track isolation and combinations of both are plotted in Fig. 4.12(c). Using the maximum of both isolation variables is clearly closer to optimal.

For a lower muon p_T threshold, the fraction of background events passing the cut rises since the muon momentum is correlated with the jet energy. Choosing the cut to require both track and calorimeter isolation to be below 2.5 GeV leads to a signal efficiency of 0.902±0.006. Of the background events, 0.242±0.001 pass this cut for a muon with transverse momentum above 10 GeV. Signal efficiencies for the four cut values considered in the final cut optimization are given in Table 4.13.

max(trkiso, E_T^{Halo})	Signal efficiency	QCD efficiency
2.5	0.902 ±0.006	0.242±0.001
2.0	0.872 ±0.006	0.199±0.001
1.5	0.825 ±0.008	0.136±0.001
1.0	0.799 ±0.009	0.095±0.001
0.5	0.370 ±0.010	0.039±0.001

Table 4.13: Signal efficiencies for various cuts on the combined muon isolation.

4.7 Di-Muon Rejection

If muons deposit more than 2 GeV of transverse energy in the calorimeter, they will be reconstructed as tau-candidates if their central track is reconstructed with a transverse momentum above 4 GeV (see section 3.7). Thus a preselection of events with a muon and a tau with at least one central track will contain di-muon events where the muon and the "tau" track are of opposite charge. As this is the signature of signal events, veto cuts are applied to reduce this background. The number of remaining $Z^0 \rightarrow \mu^- \mu^+$ events is estimated from data.

First, events with a second reconstructed local muon μ_{add} inside the fiducial region are rejected if $|\Delta\phi(\mu_{tag} - \mu_{add})| > 1$. Second, to reject events where one of the two muons is lying inside of the ϕ-hole in the A-layer and thus does not leave a local muon track, the invariant mass of central track matched to the tag-muon and a second track outside of the fiducial region is calculated. The second track is required to be isolated, of opposite charge, have a transverse momentum above 15 GeV and be in the non-fiducial region for muons. The event is rejected if the invariant mass of the muon and the track is inside a Z^0 mass window of ($60 < M(\mu - trk) < 120$) GeV. The invariant mass distribution of the two loose muons is shown on the left of Fig.4.13, using the preselected signal sample before trigger requirements and tau selection. In total 8761 di-muon events are rejected by this cut. The right plot shows the invariant mass of the muon and the track for all remaining events and the events with one track in the non-fiducial region for the muon. There are 672 Z^0 events within the Z^0 mass window.

The probabilities $\epsilon_{\mu\to\tau}^{sel,trig}$ that the second muon creates a tau object above 10 GeV which passes the selection and trigger requirements are given in Table 4.14. The remaining events fall

into two classes: those with muons either inside or outside of the muon fiducial region. The number of di-muon events in the final selection samples is then given as:

$$N_{\mu\mu}^{fid} = N_{\mu\mu}^{presel,fid} * \epsilon_{\mu\to\tau}^{sel,trig} * \frac{1-\epsilon_{\mu^{Loose}}}{\epsilon_{\mu^{Loose}}} \tag{4.10}$$

$$N_{\mu\mu}^{non-fid} = N_{\mu\mu}^{presel,non-fid,Z} * \left(\epsilon_{\mu\to\tau}^{sel,trig,Z} * (1-\epsilon_{60.<M<120.}) + \frac{N_{\mu\mu}^{fid,non-Z,\eta<1.3}}{N_{\mu\mu}^{fid,Z,\eta<1.3}} * \epsilon_{\mu\to\tau}^{sel,trig,non-Z} \right),$$

with $N_{\mu\mu}^{presel,fid} = 5932$, $N_{\mu\mu}^{presel,non-fid} = 2829$, $\frac{1-\epsilon_{\mu Loose}}{\epsilon_{\mu Loose}} = 0.074\pm0.008$, $\epsilon_{60.<M<120.} = 0.977 \pm 0.002$ and $\frac{N_{\mu\mu}^{fid,non-Z,\eta<1.3}}{N_{\mu\mu}^{fid,Z,\eta<1.3}} = 1.96\pm0.03$.

Table 4.14 summarizes the fraction of di-muon events where the second muon is reconstructed as tau with $E_T > 10$ GeV and passing the trigger requirements, assuming a muon isolation cut of max($E_T^{halo}, trkiso$) <2.5 GeV. For the numbers quoted in this table, no further tau selection cuts have been applied.

τ-type	τ_π	τ_ρ
$\epsilon_{\mu\to\tau}^{sel,trig}$	0.0019±0.0005	0.0038±0.0007
$\epsilon_{\mu\to\tau}^{sel,trig,Z}$	0.0021±0.0008	0.0039±0.0012
$\epsilon_{\mu\to\tau}^{sel,trig,non-Z}$	0.0010±0.0004	0.0037±0.0008

Table 4.14: Fraction of muons being reconstructed as tau candidates

The fractions of signal events remaining are (96.2±0.4)% for τ_π taus and (96.4±0.2)% for τ_ρ taus. This number is taken from signal MC.

4.8 Cut Optimization

To obtain the best measurement of the cross section, $\frac{S}{\sqrt{(S+B)}}$ is optimized. The three variables that are varied are

- muon isolation (max($trkiso, E_T^{Halo}$)): 2.5 GeV, 2.0 GeV, 1.5 GeV and 1.0 GeV,
- tau calorimeter isolation: no cut, 0.3, 0.2, 0.15, 0.1, 0.075 and 0.05,
- tau track isolation: no cut, 1.5 GeV, 1.0 GeV, 0.5 GeV and 0.01 GeV, and
- the profile is left to vary freely.

Due to the lower cross section, the signal significance in the τ_π channel is expected to be lower than for the τ_ρ-case. In order to get the most significant signal in this channel, the optimal set of cuts for the highest signal significance is determined as well. In this case, $\frac{S}{\sqrt{B}}$ is optimized.

The number of expected signal events S is taken from MC which has been scaled to expectation where 270 pb is used as cross section for $Z^0 \to \tau\bar{\tau}$. Only hadronic tau decays are considered. The background will be treated in detail in section 5.3. For the cut optimization, the background

model uses the following components to obtain the expected number of background events B: same-sign events in data as model for the background from QCD; W$\rightarrow \mu\nu_\mu$ events with a recoiling jet; di-muon events, scaled to the expected number of events as described in section 4.7; W-pairs and $t\bar{t}$ events where one W-boson decays into a muon with $p_T > 10$ GeV and the second W boson decays into a tau or an electron. Generator level MC events are used and the reconstruction and selection efficiencies are applied on an event-by-event basis as explained in section 5.3.

For each set of (muon isolation, tau calorimeter isolation, track isolation), the optimal value of $\frac{S}{\sqrt{(S+B)}}$ is given in Tables 4.15 and 4.16. Table 4.17 is an analogous table for the best signal significance for the τ_π channel. The sets of cuts are summarized in Table 4.18. As additional check Tables 4.15, 4.16 and 4.17 were also generated with a cut on E_T/p_T <1.5. This did not yield better significances, hence no E_T/p_T cut is applied.

τ_π, $S/\sqrt{S+B}$		τ calorimeter isolation						
μ iso (GeV)	τ track iso (GeV)	-	0.3	0.2	0.15	0.1	0.075	0.05
2.5	-	1.426	1.444	1.499	1.563	1.601	1.622	1.352
	1.5	1.780	1.787	1.830	1.911	1.897	1.825	1.496
	1.0	1.839	1.843	1.879	1.974	1.923	1.790	1.465
	0.5	1.872	1.881	1.913	1.971	1.917	1.754	1.422
	0.001	1.766	1.777	1.812	1.853	1.798	1.648	1.330
2.0	-	1.643	1.653	1.705	1.756	1.773	1.753	1.445
	1.5	2.023	2.026	2.058	2.104	2.080	1.955	1.621
	1.0	2.089	2.088	2.116	2.180	2.098	1.918	1.580
	0.5	2.116	2.128	2.122	2.139	2.063	1.882	1.548
	0.001	1.991	2.004	2.000	1.996	1.941	1.779	1.456
1.5	-	1.860	1.859	1.917	1.938	1.976	1.906	1.525
	1.5	2.252	2.254	2.251	2.271	2.241	2.077	1.679
	1.5	2.306	2.304	2.296	2.324	2.264	2.056	1.646
	0.0	2.245	2.252	2.233	2.250	2.181	1.993	1.589
	0.001	2.114	2.124	2.108	2.094	2.044	1.874	1.500
1.0	-	2.029	2.028	2.092	2.100	2.182	2.105	1.740
	1.5	2.493	2.485	2.505	2.503	2.449	2.351	2.023
	1.0	2.548	2.526	2.560	2.543	2.534	2.333	1.993
	0.5	2.485	2.469	2.476	2.474	2.397	2.234	1.905
	0.001	2.334	2.321	2.329	2.298	2.240	2.090	1.785
0.5	-	1.577	1.584	1.634	1.606	1.597	1.531	1.253
	1.5	1.912	1.930	1.919	1.846	1.832	1.745	1.481
	1.0	1.988	1.973	1.963	1.904	1.877	1.753	1.505
	0.5	1.990	1.978	1.943	1.900	1.775	1.706	1.395
	0.001	1.856	1.846	1.812	1.768	1.659	1.597	1.307

Table 4.15: Optimized $S/\sqrt{(S+B)}$ values for each set of cuts for τ_π taus. For each bin the $S/\sqrt{S+B}$ value corresponds to the optimal profile cut.

τ_ρ, $S/\sqrt{S+B}$		τ calorimeter isolation						
μ iso (GeV)	τ track iso (GeV)	-	0.3	0.2	0.15	0.1	0.075	0.05
2.5	-	4.672	4.696	4.763	4.842	5.015	4.975	4.688
	1.5	5.270	5.301	5.418	5.503	5.553	5.483	5.039
	1.0	5.485	5.527	5.658	5.776	5.790	5.728	5.203
	0.5	5.443	5.477	5.615	5.704	5.795	5.732	5.135
	0.001	5.253	5.299	5.427	5.537	5.623	5.581	4.989
2.0	-	4.955	4.973	5.041	5.121	5.256	5.195	4.813
	1.5	5.605	5.635	5.752	5.853	5.823	5.692	5.282
	1.0	5.800	5.840	5.959	6.062	5.990	5.869	5.345
	0.5	5.743	5.777	5.930	5.988	6.003	5.915	5.277
	0.001	5.616	5.656	5.752	5.830	5.827	5.753	5.097
1.5	-	5.400	5.396	5.524	5.658	5.721	5.606	5.002
	1.5	6.252	6.256	6.437	6.579	6.392	6.136	5.471
	1.0	6.392	6.382	6.548	6.707	6.494	6.302	5.521
	0.5	6.233	6.221	6.394	6.506	6.371	6.162	5.533
	0.001	6.124	6.115	6.192	6.298	6.203	6.043	5.366
1.0	-	5.556	5.551	5.665	5.710	5.690	5.539	4.840
	1.5	6.271	6.283	6.384	6.423	6.209	5.881	5.162
	1.0	6.293	6.309	6.434	6.449	6.259	5.973	5.184
	0.5	6.067	6.055	6.153	6.144	5.981	5.719	5.063
	0.	5.877	5.866	5.904	5.908	5.758	5.572	4.910
0.5	-	4.636	4.656	4.711	4.693	4.597	4.410	3.973
	1.5	5.004	4.995	5.048	5.033	4.977	4.652	4.187
	1.0	4.843	4.835	4.893	4.887	4.848	4.554	4.071
	0.5	4.667	4.658	4.741	4.655	4.657	4.427	4.044
	0.001	4.599	4.591	4.567	4.488	4.504	4.307	3.899

Table 4.16: Optimized $S/\sqrt{(S+B)}$ values for each set of cuts for τ_ρ taus. For each bin the $S/\sqrt{S+B}$ value corresponds to the optimal profile cut.

The efficiencies for signal of the selection optimized for the cross section measurement are 0.801±0.017±0.066 for the τ_π channel and 0.676±0.009±0.009 for the τ_ρ channel. The rate of QCD jets surviving these cuts as measured in events with non-isolated muons is 0.121±0.002 for τ_π taus and 0.0465±0.0007 for τ_ρ taus.
A candidate event is shown in Fig. 4.14. The candidate shows a muon in the upper right direction in (a). The amount of energy in the electromagnetic calorimeter may be a final state photon that accompanies the muon. On the other side of the event a single hadron is detected, both as a track and as a hadronic energy deposition in the calorimeter.

τ_π, $S/\sqrt{B}$		τ calorimeter isolation						
μ iso (GeV)	τ track iso (GeV)	-	0.3	0.2	0.15	0.1	0.075	0.05
2.5	-	1.486	1.507	1.566	1.643	1.703	1.753	1.463
	1.5	1.893	1.900	1.956	2.058	2.083	2.026	1.657
	1.0	1.963	1.970	2.019	2.148	2.127	1.989	1.621
	0.5	2.035	2.048	2.097	2.185	2.158	1.982	1.593
	0.001	1.916	1.932	1.981	2.047	2.012	1.853	1.481
2.0	-	1.740	1.753	1.816	1.876	1.921	1.928	1.589
	1.5	2.201	2.201	2.248	2.318	2.343	2.218	1.841
	1.0	2.284	2.289	2.333	2.432	2.369	2.181	1.799
	0.5	2.371	2.390	2.390	2.432	2.377	2.185	1.795
	0.001	2.222	2.243	2.244	2.254	2.224	2.057	1.688
1.5	-	2.014	2.011	2.076	2.115	2.202	2.154	1.842
	1.5	2.501	2.511	2.518	2.560	2.606	2.426	1.945
	1.0	2.597	2.597	2.596	2.659	2.649	2.414	1.972
	0.5	2.579	2.599	2.585	2.626	2.590	2.392	2.068
	0.001	2.417	2.441	2.429	2.421	2.408	2.233	1.856
1.0	-	2.256	2.256	2.353	2.380	2.571	2.538	2.102
	1.5	2.926	2.920	2.968	3.002	3.060	3.042	2.697
	1.0	3.054	3.024	3.115	3.115	3.247	3.045	2.679
	0.5	3.104	3.079	3.114	3.137	3.136	3.023	2.651
	0.001	2.888	2.868	2.902	2.867	2.881	2.776	2.436
0.5	-	1.782	1.794	1.875	1.838	1.885	1.844	1.629
	1.5	2.322	2.357	2.352	2.236	2.318	2.271	1.969
	1.0	2.478	2.456	2.455	2.366	2.433	2.315	2.061
	0.5	2.646	2.625	2.567	2.495	2.349	2.360	1.995
	0.001	2.422	2.405	2.351	2.281	2.158	2.168	1.807

Table 4.17: Optimized $S/\sqrt{B}$ values for each set of cuts for τ_π taus. For each bin the $S/\sqrt{B}$ value corresponds to the optimal profile cut.

Optimization	cross section measurement		signal significance
τ-type	τ_π	τ_ρ	τ_π
muon isolation < (GeV)	1.0	1.5	1.0
τ calorimeter isolation <	0.2	0.15	0.1
τ track isolation < (GeV)	1.0	1.0	1.0
profile >	0.35	0.55	0.0

Table 4.18: Sets of optimized cuts.

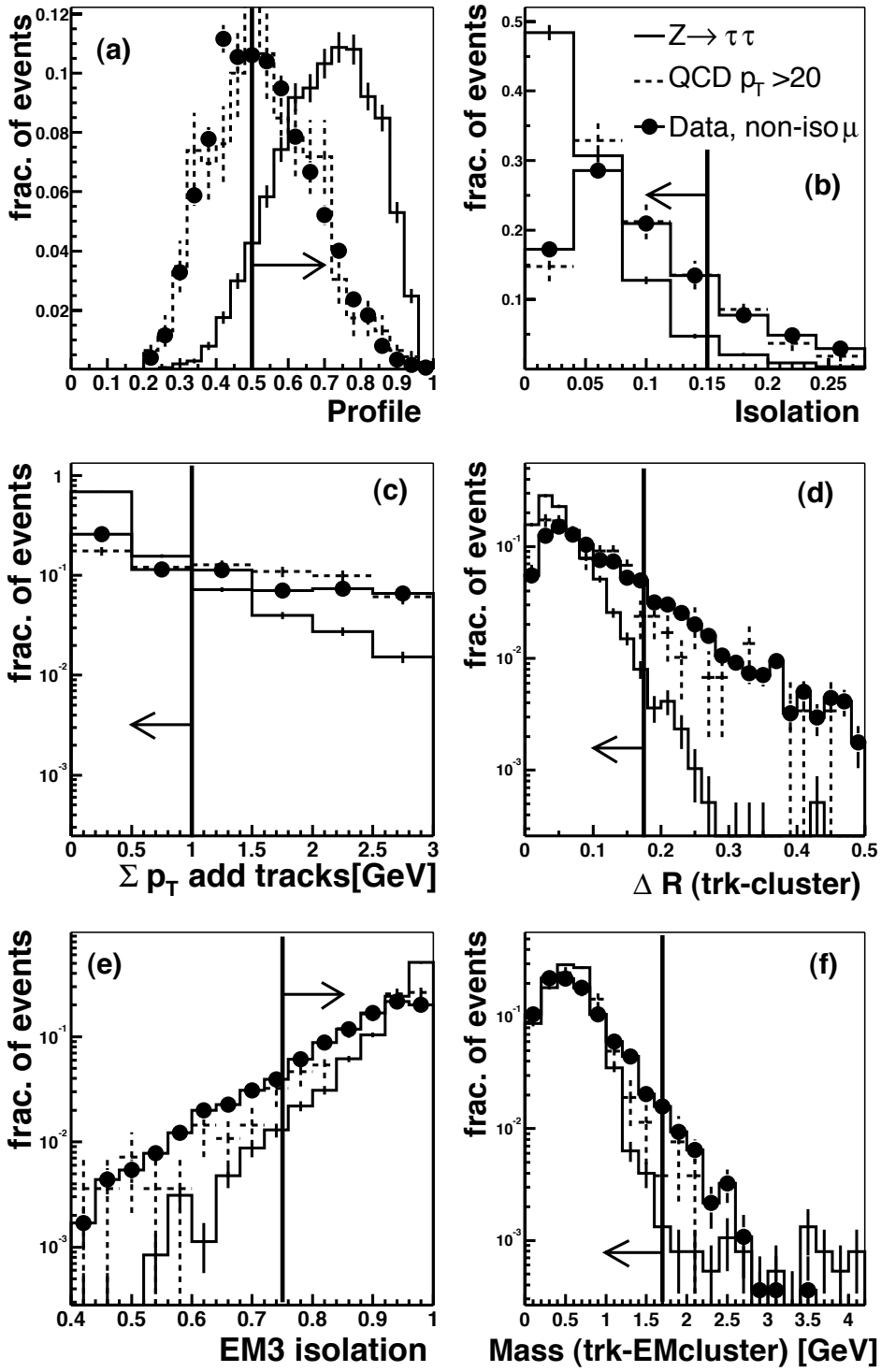

Figure 4.8: Tight selection cuts for $\rho\nu$-type taus. All cuts except for the one illustrated have been applied. Signal MC is indicated by the full line, the dashed error bars show QCD MC and the full dots are data. Plot a) shows the profile, b) the isolation, c) the track isolation, d) the angle between track and hadronic tau cluster, e) the isolation in the third EM layer, and f) the mass of the tau track and the EM cluster.

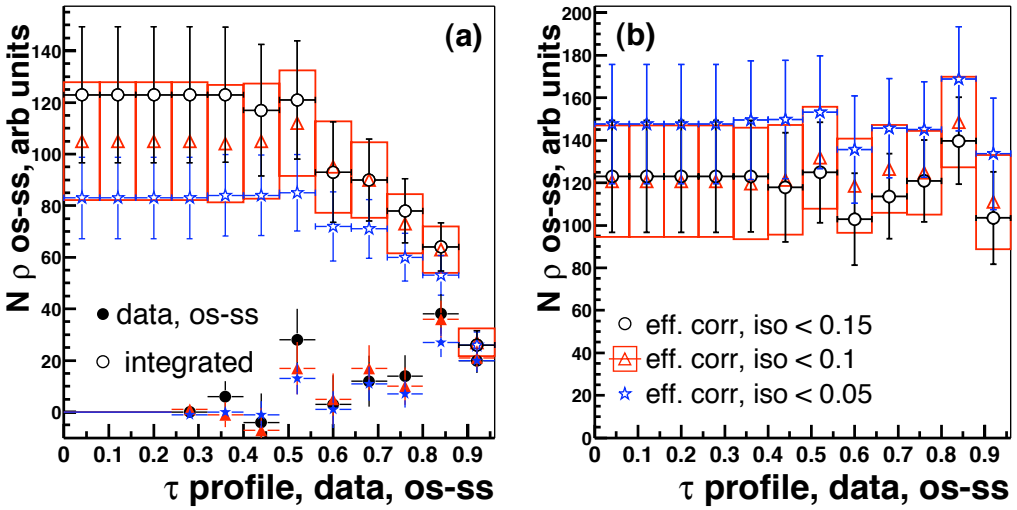

Figure 4.9: Number of signal events versus the profile value in data for three cuts in the isolation (dots for isolation<0.15, triangle for 0.1 and stars for a cut at 0.05). The number of events is background subtracted (i.e. “opposite sign−same sign”). The filled markers in a) show the data, the outlined markers are the integrated number of events above the profile value. The curves in b) are the integrated number of signal events, corrected for the MC efficiency of the profile and isolation cuts.

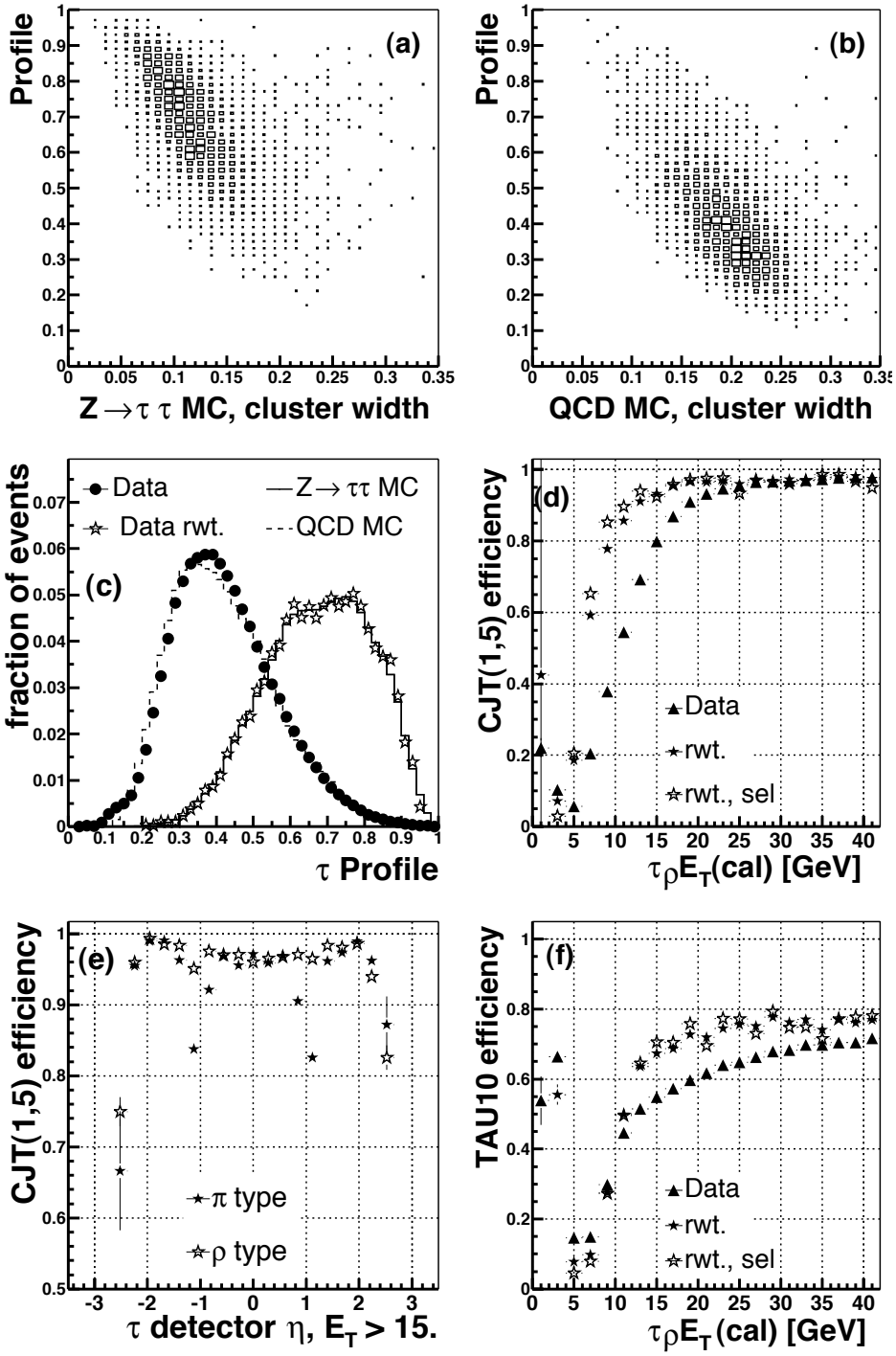

Figure 4.10: the tau profile versus cluster width for $Z^0 \rightarrow \tau\overline{\tau}$ signal MC (a) and QCD background MC (b); (c) profile distribution for data (solid points), re-weighted data (stars) and signal/background MC (solid/dashed lines); (d) L1 trigger turn-on curves for τ_ρ, triangles are data, stars re-weighted data, the empty stars are re-weighted data passing the selection cuts described in 4.4.6. The level 1 tau trigger efficiency versus η_{det} is shown in (e); (f) shows the turn-on curve for the level 3 tau trigger.

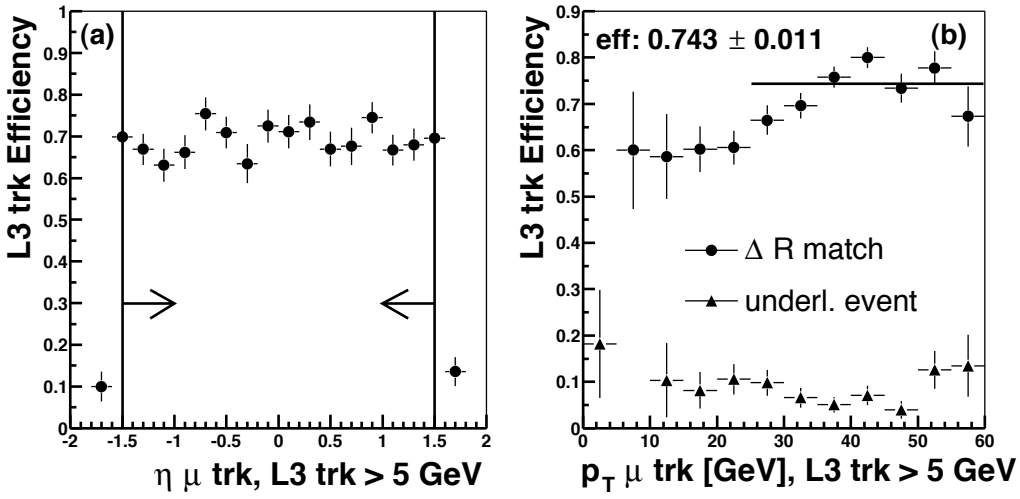

Figure 4.11: (a): the efficiency for a muon track with > 5 GeV to be reconstructed as L3 track as a function of η. The L3 track efficiency as a function of p_T for $|\eta|$ <1.5 is shown in (b), together with the probability that a non-muon track is reconstructed as a L3 track above 5 GeV. Between 5 and 10 GeV there were no non-muon tracks with a L3 track above 5 GeV p_T.

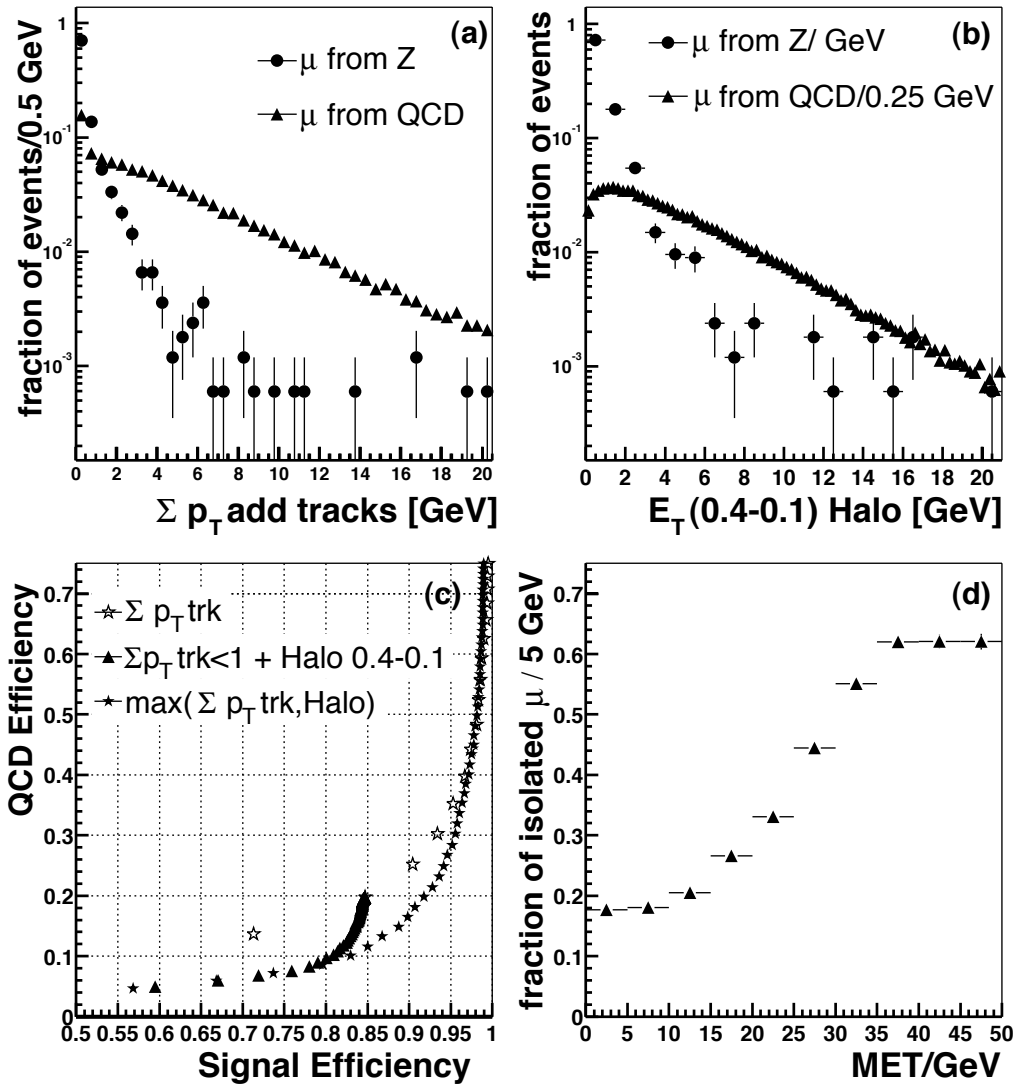

Figure 4.12: The distribution of the sum of the p_T of tracks in a 0.5 cone around muons from Z decays and in QCD background events are shown in (a). The same is plotted in (b) for the transverse energy in a cone between 0.1 and 0.4 in $\eta\phi$-space muon. Signal versus background efficiency for the track isolation and the combination of both cuts are shown in figure (c). Figure (d) shows the fraction of muons passing the isolation cuts versus the missing E_T.

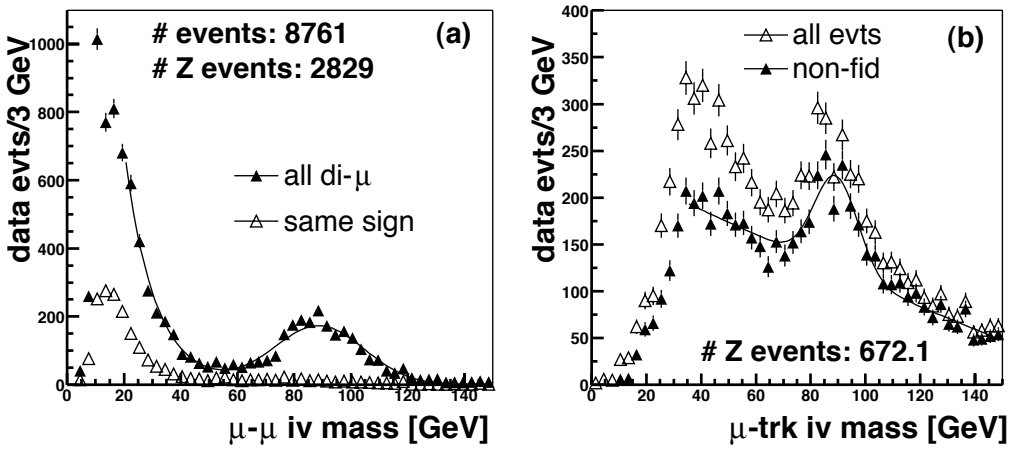

Figure 4.13: The invariant mass of the tagging muon and the additional local muon in the preselected signal sample is plotted in (a). The second di-muon rejection cut using central tracks in the signal sample passing the first di-muon rejection cut is illustrated in (b). The open triangles denote all events with a second isolated track above 15 GeV. The full triangles denote events in the non-fiducial region.

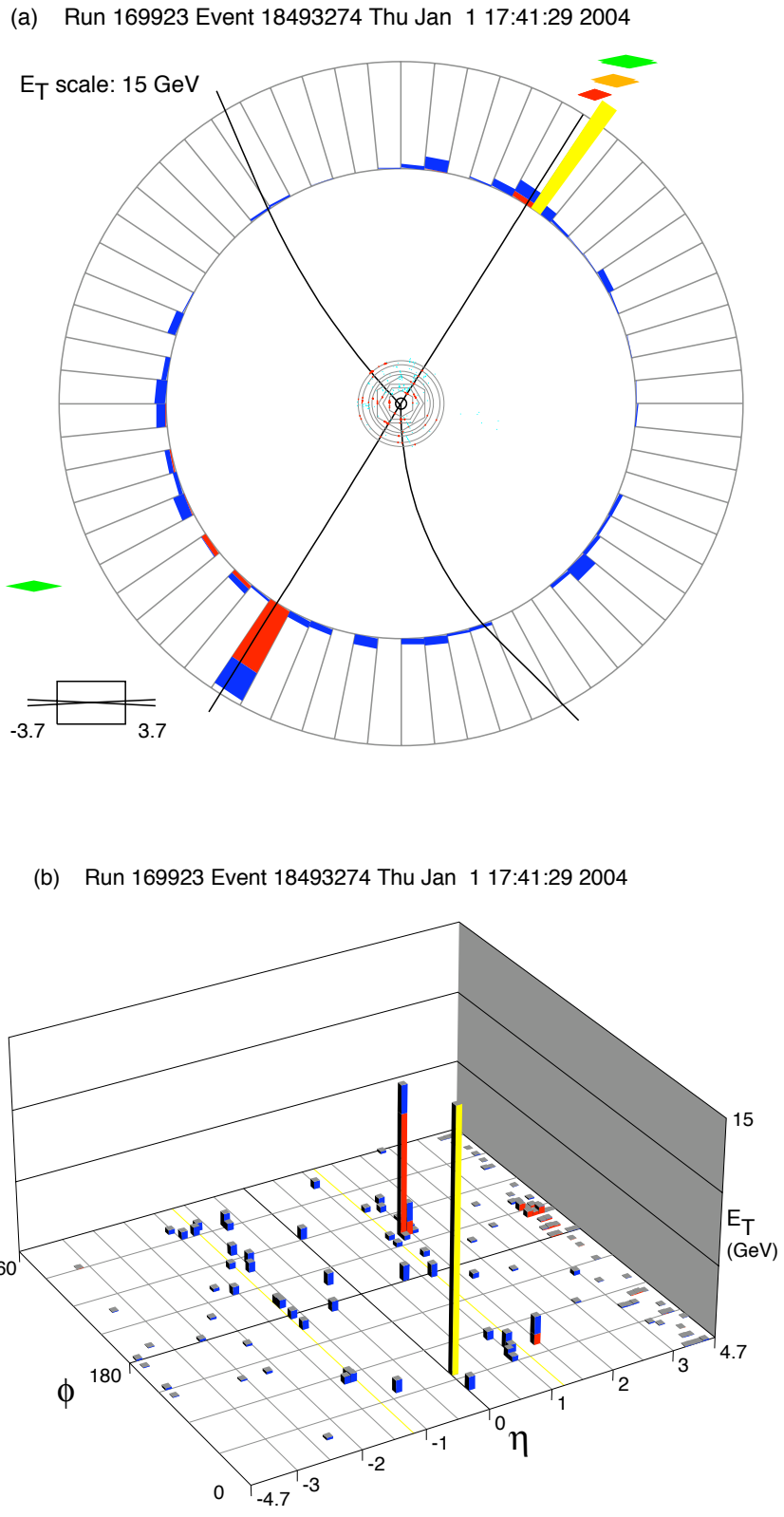

Figure 4.14: Candidate event: (a) an XY-view, (b) a lego display of the calorimetric energy deposits.

Chapter 5

The $Z^0 \to \tau\overline{\tau}$ Cross Section

The selection efficiency for $Z^0 \to \tau\overline{\tau}$ events in the muon-hadronic tau final state has been discussed in the preceding chapter. This chapter is concerned with converting the number of selected events into a cross section. First, the presence of electron-muon events in the final candidate sample is discussed. The most important backgrounds are studied in section 5.3. The treatment of the two largest sources of background, QCD and $W \to \mu\nu_\mu$ events, is based on the assumption that the hadronic tau candidates in these events are fakes for which the charge of the leading track is random. To calculate the number of signal events, the number of events where the muon and the track of the hadronic tau candidate have the same sign is subtracted from the number of events with oppositely charged muon and hadronic tau track. This chapter concludes with the calculation of the $Z^0 \to \tau\overline{\tau}$ cross section in the $\mu\tau_\pi$ and $\mu\tau_\rho$ channels. This calculation will be done in two ways: "Reweighted", referring to a cross section measurement where the events are given a weight according to the expected muon trigger and tracking efficiency as function of η_μ and "Counted" referring to the background for the cross section measurement where the events which pass the final selection cut are counted with a weight of one.

5.1 Electron Contamination

Since electrons appear as narrow objects in the calorimeter, they pass the tau selection with a non-negligible efficiency. Mostly they fake τ_ρ taus, but in the ICD region they can also be reconstructed as τ_π. To reject electrons, hadronic tau candidates with an EM fraction above 0.8 and a ratio of E_T/p_T between 0.6 and 1.4 can be rejected, as illustrated in Fig. 5.1. This rejects most electrons in the τ_ρ-case, but is inefficient for τ_π taus where most of the misidentified electrons lie in the ICD region and can only be rejected by a fiducial cut.
Most electron-muon events are decays of $Z^0 \to \tau\overline{\tau}$. They are not rejected for this cross section measurement, and their contribution is taken into account using a scale factor to convert the "hadronic only" efficiency into an effective efficiency. As a cross-check, the cross section will be calculated using the electron rejection cut. This factor depends on the exact selection, e.g. the tighter the profile cut, the higher the fraction of electrons in the τ_ρ sample, as electrons tend to have high profile values. The scale factors are estimated from $Z^0/\gamma^* \to \tau\tau$ MC events. The efficiencies of the electron rejection cuts and the electron contamination factor are listed in Table 5.1.

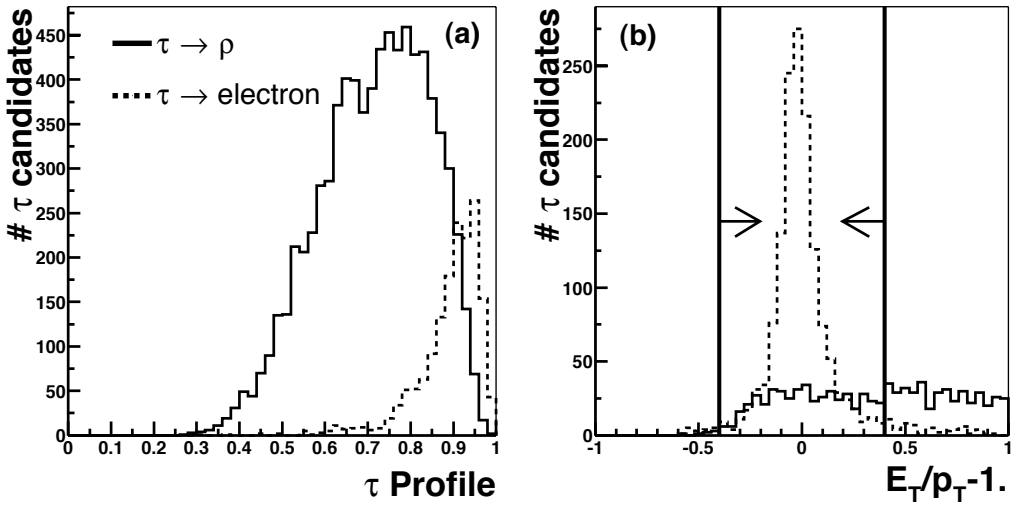

Figure 5.1: The profile distribution after all other selection cuts for true τ_ρ candidates and electrons in (a). The relative scale corresponds to the tau branching fraction. The second of the suggested electron rejection cuts is illustrated in (b).

	τ_π	τ_ρ	τ_π, after e cut	τ_ρ, after e cut
Efficiency	1.	1.	0.998±0.001	0.932 ±0.004
electron factor	1.07±0.02	1.32±0.01	1.07± 0.02	1.04±0.01

Table 5.1: Electrons selected as hadronic taus for the cross section optimized cuts (see section 4.8). The right columns give the numbers after applying the electron rejection cut. The numbers are estimated from di-tau Monte Carlo events.

5.2 Charge Mis-measurement

The method to correct for the presence of QCD and W$\rightarrow \mu\nu_\mu$ events in the selected sample of events is to subtract opposite sign events from same sign events. If the charge of either the muon or the tau is mis-reconstructed, the events will incorrectly be labeled "same sign" and subtracted from the correctly identified "opposite sign" events.

The fraction of tracks with a mis-reconstructed charge for the data considered here is determined from the $Z^0 \rightarrow \mu^-\mu^+$ cross section measurement [99]. There, two oppositely charged muons are required and the in-efficiency of this cut is measured to be 0.6±0.6%. This translates into a fraction of 0.3±0.3% of muons having an incorrectly reconstructed charge. In this measurement of the $Z^0 \rightarrow \tau\bar{\tau}$ cross section, the tracks are of lower momentum which will result in a better charge determination. A distribution of the invariant mass of two same sign muons between 1 and 6 GeV did not show any sign of a J/ψ peak. This cross check is compatible with no charge confusion for these lower energetic muons. The mean value of the charge confusion as measured in $Z^0 \rightarrow \mu^-\mu^+$ decays will be used as upper limit with a mean value of the charge mis-measurement of zero. A rate of $(0.0^{+0.3}_{-0.0})$% of mis-reconstructed charges will result in an effect of $(0.0^{+1.2}_{-0.0})$% on the cross section assuming background subtraction of "same sign" events

from “opposite sign” events.

5.3 Background Estimate

The background is dominated by the following sources, in order of importance:

- QCD with muons from b quarks or prompt π and K decay,
- $W \rightarrow \mu\nu_\mu$ (with an additional jet) and $W \rightarrow \tau\nu_\mu$ (with an additional jet and the τ decaying into a muon),
- $Z^0 \rightarrow \mu^-\mu^+$,
- WW with one W decaying into a muon or into a tau decaying into a muon and the other into an electron or tau, and
- $t\bar{t}$ with the same combination of W decays as for W-pair events.

The cross section of the first three backgrounds is higher than or similar to the tau-pair production cross section. The latter two have a smaller rate. The contribution of the first two sources of background will be estimated from data by subtracting events where the muon has the same charge as the tau (“like-sign”) from events where both tracks have opposite charge. A systematic effect results if there is a charge bias in one of the backgrounds. This is the case for the $Z^0 \rightarrow \mu^-\mu^+$ background, for which rejection cuts have been designed in section 4.7. The number of events remaining in the signal sample will be calculated as described in the following subsection. A charge correlation exists as well for background events from W-pair production and $t\bar{t}$ decays. These backgrounds have a relatively small cross section and are estimated from Monte Carlo simulation.

We will begin to discuss the number of background events expected from dimuon events. Then the estimates of the WW and $t\bar{t}$ backgrounds are discussed, followed by an analysis of the most important backgrounds, $W \rightarrow \mu\nu_\mu$ and QCD.

5.3.1 Di-muon Events

The background from dimuon events and its rejection was treated in section 4.7. Rejected are events with

- a second loose muon in the fiducial region with $|\Delta\phi(\mu_{tag} - \mu_{add})| > 1$, or
- an isolated track with $p_T > 15$ GeV which has an invariant mass with the muon between 60 and 120 GeV.

The number of dimuon events remaining in the sample after the rejection cuts is estimated from data using equation 4.10. The dimuon background to be subtracted from the number of signal candidates is the excess of events where the muon and the tau have opposite charge. The size of the di-muon background is given in Table 5.2 in both the τ_π and the τ_ρ channel.

Sample	τ_π	τ_ρ
counting events	0.52±0.20	1.44±0.51
muon reweighted $_{<173352}$	0.63±0.24	1.04±0.37
muon reweighted $_{\geq 173352}$	0.09±0.03	0.88±0.31

Table 5.2: Number of di-muon events remaining in the final event sample after subtraction of the same sign events. "Counting events" refers to the background for the cross section measurement where the events which pass the final selection cut are counted with a weight of one. "Reweighting" in contrast refers to cross section measurement where the events are given a weight according to the expected muon trigger and tracking efficiency as function of η_μ.

5.3.2 W-pair and $t\bar{t}$ Events

Generator level W-pair and $t\bar{t}$ events are used to estimate the background from these sources. One of the W bosons is required to decay into a muon with a transverse momentum above 10 GeV within the fiducial region. Events where the other W-boson decays either into a tau or an electron have to be considered as backgrounds as the charges of this hadronic tau candidate and the muon are opposite. The probability of the electron or tau to pass the selection cuts is calculated using equations 4.6 and 4.7. For electrons, they are modified to:

$$N^{\pi}_{\text{measured}} = \sum_{p_T} \epsilon^{\pi}_{\text{trigger}} * \epsilon^{\pi}_{\text{selection}} * N_{\text{e}} * \epsilon_{acc} * \epsilon^{\text{e}}_{\text{reco,trk}} * f(\text{e} \rightarrow \pi), \tag{5.1}$$

$$N^{\rho}_{\text{measured}} = \sum_{p_T} \epsilon^{\rho}_{\text{trigger}} * \epsilon^{\rho}_{\text{selection}} * N_{\text{e}} * \epsilon_{acc} * \epsilon^{\text{e}}_{\text{reco,trk}} * f(\text{e} \rightarrow \rho), \tag{5.2}$$

where $f(\text{e} \rightarrow \pi)$ and $f(\text{e} \rightarrow \rho)$ are the fractions of e classified as τ_π and τ_ρ, respectively. The number of W-pair events passing the selection criteria for the muon and the tau candidate is estimated using the NNLO W-pair cross-section of 13.25 pb [104]. The top-pair production cross section used is 6.5±0.8 pb [105]. Table 5.3 lists the expected backgrounds for each source separately, not taking into account events where the electron or muon is produced by a decaying tau.

Background source	τ_π	τ_ρ
WW$\rightarrow \mu\tau_{\text{had}}$	0.16	0.60
WW$\rightarrow \mu$e	0.13	2.32
$t\bar{t} \rightarrow \mu\tau_{\text{had}}$	0.08	0.16
$t\bar{t} \rightarrow \mu$e	0.07	0.99

Table 5.3: Number of background events from W-pair and $t\bar{t}$ production, not including $\tau\rightarrow\mu$ or $\tau\rightarrow$e contributions.

The numbers in Table 5.3 are the expected background from events where the muon, electron and hadronic tau are direct decay products of the W boson. Taking events into account where the direct W-daughter is a tau decaying into a muon and/or an electron results in an ≈20% higher number of background events. The L3 track trigger efficiency for these W-pair events

is 0.92±0.02. Top events have many more tracks than W or Z^0 events and thus a higher event trigger probability. An efficiency of 0.95±0.05 is used as an estimate in this case, the higher uncertainty reflecting the missing measurement of this number from data.

The method used to estimate the number of background events is the same as used for the determination of the signal efficiency, hence the systematic uncertainty on the number of background events is the sum of the uncertainties on the muon and tau reconstruction, of the L3 track trigger efficiency and on the Standard Model cross section.
The total number of background events from W-pairs and $t\bar{t}$ expected in the final event sample is given in Table 5.4.

Selection	τ_π	τ_ρ
counting events	0.47±0.08	4.62±0.52
muon reweighted$_{<177352}$	0.49±0.08	4.75±0.54
muon reweighted$_{\geq 177352}$	0.17±0.03	1.60±0.18

Table 5.4: Total number of background events from W-pair and $t\bar{t}$ production.

The distributions of $\Delta\phi$ and the invariant mass of the muon and the tau track for the WW and $t\bar{t}$ backgrounds are shown in Fig. 5.2.

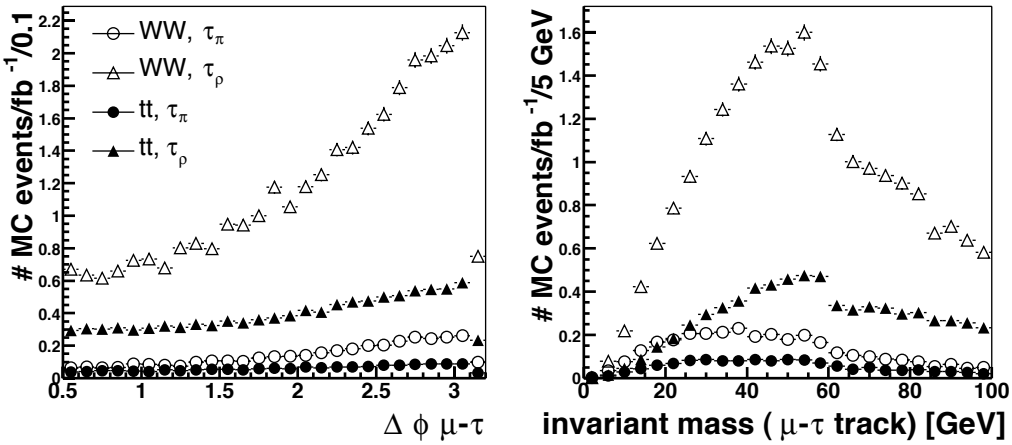

Figure 5.2: Number of events from W-pair and $t\bar{t}$ production as a function of the angle between the muon and the tau in (a) and as a function of the invariant mass of the muon and the tau track (b). The dimuon rejection cut introduces a discontinuity in the invariant mass distribution for the τ_ρ type. Used are events where one of the W bosons decays into a muon and the other W decays into an electron or hadronic tau.

5.3.3 QCD Events

QCD events contain muons as decay products of either b quarks or decay in flight of pions and Kaons. These muons are usually embedded in jets. As explained in section 4.6, these events pass the muon isolation cuts with a non-negligible efficiency and lead to a contribution to the

signal event sample if an additional jet is reconstructed as a tau candidate with a single matched track. The tau candidate will have the charge of the leading track in this jet. In general, one would expect this to be equally often of opposite sign with respect to the muon as of same sign. A charge correlation between the muon and the tau candidate could arise from $b\bar{b}$ if the leading track in the non-muon b decay on average reflects the charge of the quark.

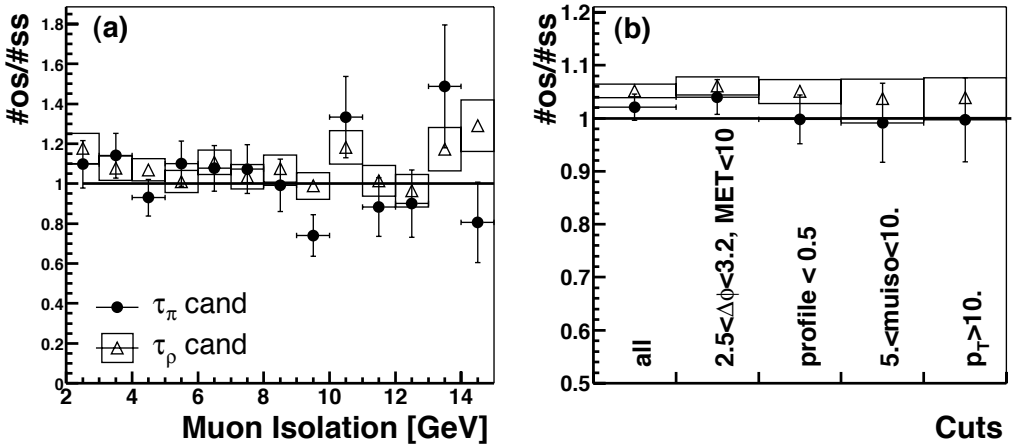

Figure 5.3: (a) shows the ratio of opposite sign and same sign events as a function of the muon combined isolation. (b) shows the same ratio for different selection steps to get a clean QCD sample. Full circles are for τ_π candidates, open triangles with boxes indicating the error are for τ_ρ candidates.

To measure the charge correlation factor in QCD background events, a sample of events with non-isolated muons is used. The ratio of opposite sign events and same sign events as a function of the combined muon isolation is plotted in Fig.5.3(a). Figure 5.3(b) shows this ration for a number of selection steps to improve the purity of the QCD sample. QCD events are mostly back-to-back in ϕ and the tau objects have low profile values. Requiring the muon isolation to be between 5 and 10 GeV minimizes the number of events from $Z^0 \rightarrow \tau\bar{\tau}$ and $W \rightarrow \mu\nu_\mu$ decays. The last check is to see whether the requirement to have a tau p_T above 10 GeV introduces an additional bias. Within errors, the charge correlation factor for both τ_π and τ_ρ taus is the same for all selection steps. The charge correlation factor used is the number measured in the complete QCD sample and is 1.02±0.02 for τ_π taus and 1.05±0.01 for τ_ρ taus. This charge correlation factor and the one for $W \rightarrow \mu\nu_\mu$ events is used to extract the charge correlation existing in background events. This factor is needed for the background subtraction using same sign events.

5.3.4 $W \rightarrow \mu\nu_\mu$ Events

The second largest source of background events next to QCD events are $W \rightarrow \mu\nu_\mu$ decays. The cross section of this process is about 50 times higher than for $Z^0 \rightarrow \tau\bar{\tau}$ decays with one tau decaying into a muon and the other decaying hadronically. The tau candidate in this type of events is produced by the hadronic system recoiling against the W-boson. The requirement of 10 GeV on the hadronic tau candidate, in this case the recoiling system, reduces this source

of background. Looking at the event from the perspective of the involved quarks, the total charge of the underlying event is opposite to the W charge and hence to the muon charge. Similar to the case of QCD events, one would expect the same number of opposite sign and same sign events if the tau track is picked at random and there is no bias to the highest p_T track carrying the charge of the recoiling system. As this is difficult to model in Monte Carlo, the charge correlation factor in W events is measured from data, using events with an isolated muon (max(track isolation, calorimeter isolation)<2.5 GeV). Most of the energy in the hard scatter is carried by the W boson and its decay products, the muon and the muon neutrino, are back-to-back in ϕ. To first order, the ϕ-direction of the recoiling system is uncorrelated with the muon. The distribution in $\Delta\phi$ between the muon and the recoiling system is shown in Fig. 5.4(a) together with $\Delta\phi$ of the muon and tau (candidate) in $Z^0 \to \tau\bar{\tau}$ events and data. The lines indicate the region 1.0< $\Delta\phi$ <2.0 which is selected to reduce the number of $Z^0 \to \tau\bar{\tau}$ signal events and remaining QCD events as well.

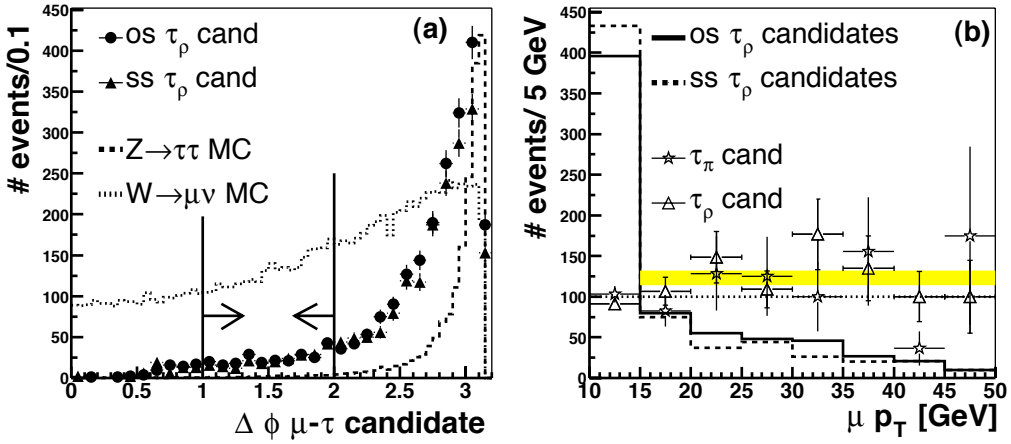

Figure 5.4: (a) shows $\Delta\phi$ between the muon and the tau candidate in data for opposite sign (dots) and same sign events (triangles) as well as for $Z^0 \to \tau\bar{\tau}$ MC (dashed line) and W→ $\mu\nu_\mu$ MC events (dotted line). The latter two curves are arbitrarily scaled. (b) the transverse muon momentum in the τ_ρ tau case for opposite sign (full line) and same sign (dashed line) events after the $1 < \Delta\phi < 2$ cut. The ratio of opposite sign and same sign events multiplied by 100 as a function of the muon p_T for τ_ρ (open triangles) and τ_π (open stars) taus is also shown in (b). The gray area indicates the average ratio for muon p_T value above 15 GeV.

The number of opposite sign and same sign events in this $\Delta\phi$ range are plotted versus the muon p_T in Fig. 5.4 (b). The ratio of opposite and same sign events multiplied by 100 is shown as well. Muons in W→ $\mu\nu_\mu$ events have large transverse momenta. The peak of events with muon p_T values between 10 and 15 GeV indicates the presence of QCD events in the sample. The charge correlation factor for W→ $\mu\nu_\mu$ events is measured using events with 1.0< $\Delta\phi(\mu - \tau)$ <2.0 and muon p_T > 15 GeV and has a value of 1.01±0.14 for τ_π and 1.23±0.09 for τ_ρ.
For W→ $\tau\nu_\tau$ events, one expects the same $\Delta\phi$ distributions as for W→ $\mu\nu_\mu$ events. Thus they will contribute to the muons with lower p_T in the sample that the charge correlation factor is measured in. The charge correlation factor in both W→ $\mu\nu_\mu$ and W→ $\tau\nu_\tau$ should be the same

as the behavior of the recoil is not influenced by the decay of the W. Hence the W$\rightarrow \tau\nu_\tau$ contribution is taken care of automatically.

5.3.5 Background Summary

The number of background events from WW, $t\bar{t}$ and dimuon events are given in Table 5.5. This table is the sum of Table 5.2 and Table 5.4

Selection	τ_π	τ_ρ
counting events	0.99±0.22	6.06±0.71
muon reweighted$_{<177352}$	1.12±0.25	5.79±0.64
muon reweighted$_{\geq 177352}$	0.26±0.04	2.48±0.35

Table 5.5: Number of background events from WW, $t\bar{t}$ and dimuon events.

To estimate the charge correlation factor for background from QCD and W$\rightarrow \mu\nu_\mu$ events, the relative contribution of both backgrounds has to be determined. This is done by fitting the $\Delta\phi(\mu - \tau)$ distribution in same sign events with templates from MC in the W$\rightarrow \mu\nu_\mu$ case and from non-isolated muon events for QCD events. As a check, the same distributions on opposite sign events is used. The results are compatible when excluding the very back-to-back range for opposite sign events where a contribution of the $Z^0 \rightarrow \tau\bar{\tau}$ signal is expected. QCD events contribute 0.72±0.02±0.02 to the background. The first error is the statistical error resulting from the fit, the second number is the systematic uncertainty estimate using the opposite sign distributions and varying the fit range. The total charge correlation factor is determined to be 1.01±0.02 for τ_π and 1.10±0.03 for τ_ρ events.

5.4 Properties of the Selected Events

The final criteria for event selection are:

- a medium muon with a matched central, 3-D track above 10 GeV p_T,
- a tau candidate with a single matched track and a cluster E_T above 10 GeV,
- the trigger MU_TAU10_L2M0 is required to have fired,
- the offline tau candidate has to be matched to the L1 calorimeter tower and the L3 tau candidate,
- the muon has to be isolated: max(trkiso, E_T^{Halo})<1.0 GeV (τ_π) or <1.5 GeV(τ_ρ),
- the tau candidate has to pass the optimized selection criteria for its reconstructed type (either τ_π of τ_ρ),
- no second loose muon in the fiducial region with $|\Delta\phi(\mu_{tag} - \mu_{add})| > 1$, and

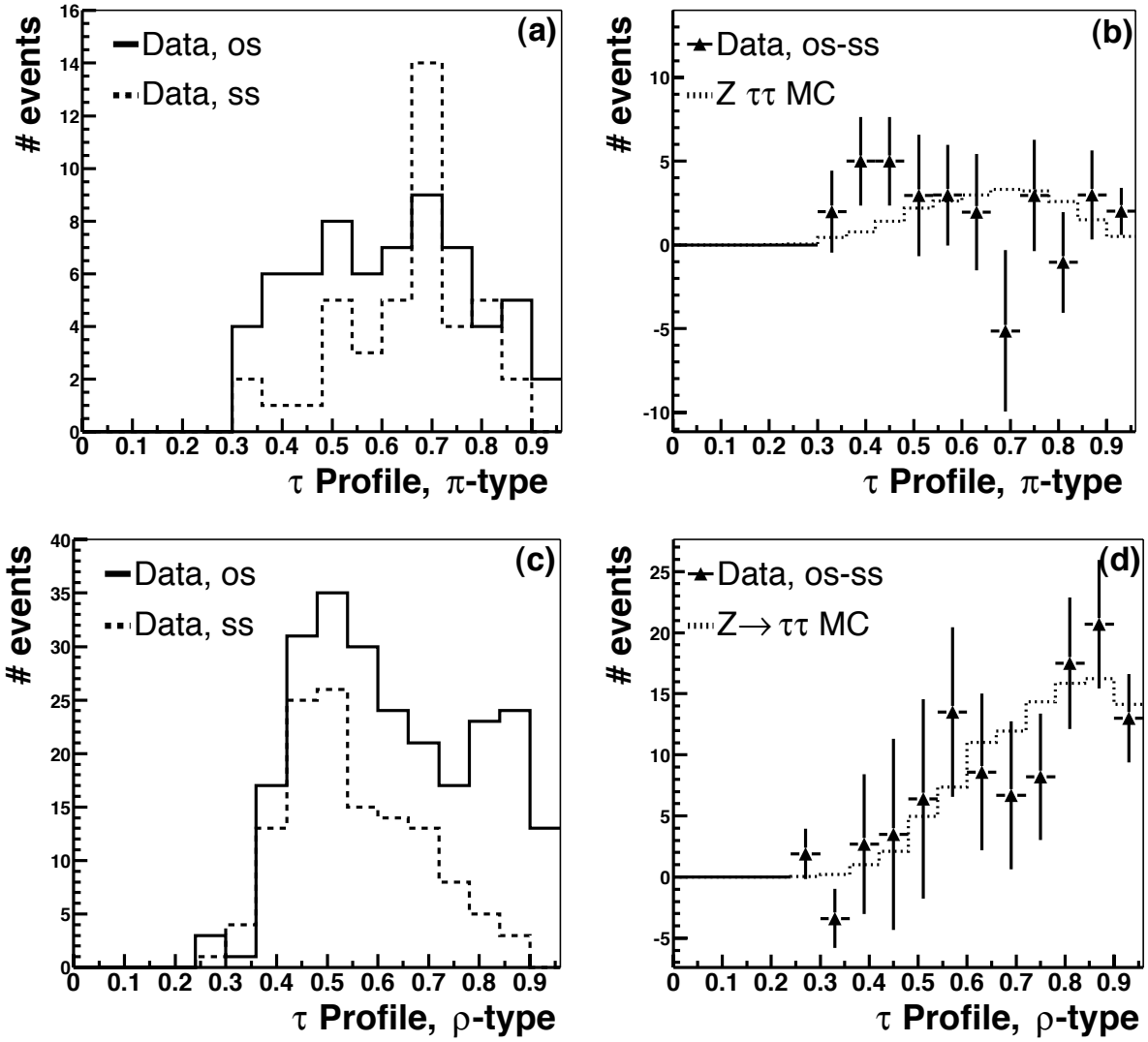

Figure 5.5: The tau profile for events with opposite charge of the muon and the hadronic tau and same sign events for (a) τ_π and (c) τ_ρ. All cuts but the tau profile cut are applied. (b) and (d) show the same variable for background subtracted data and $Z^0 \to \tau\bar{\tau}$ MC with the same normalization for shape comparisons.

- no isolated track with $p_T > 15$ GeV which has an invariant mass with the muon between 60 and 120 GeV.

For events passing all selection criteria except for the profile cut, this variable has been plotted in Fig. 5.5. Plots (a) and (c) show the profile for both the opposite and same sign sample, (b) and (d) show the background subtracted plot with the MC expectation for shape comparison. For τ_ρ taus, the shape of the profile distribution of the background subtracted data is well described by the prediction for $Z^0 \to \tau\bar{\tau}$ signal from MC. For τ_π taus, the statistics are too poor to draw any conclusions.

For events passing all the selection cuts, the angle between the muon and the hadronic tau candidate and the invariant mass of the muon and the hadronic tau track are plotted in Fig. 5.6. In both the τ_π and τ_ρ cases, the data events are mostly back-to-back as expected for Z^0-decay products. The mass of the muon and the tau track in the τ_ρ events is very well described by the $Z^0 \rightarrow \tau\bar{\tau}$ MC. Here again, for τ_π the available statistics does not allow to draw significant conclusions about matching of data and MC distributions.

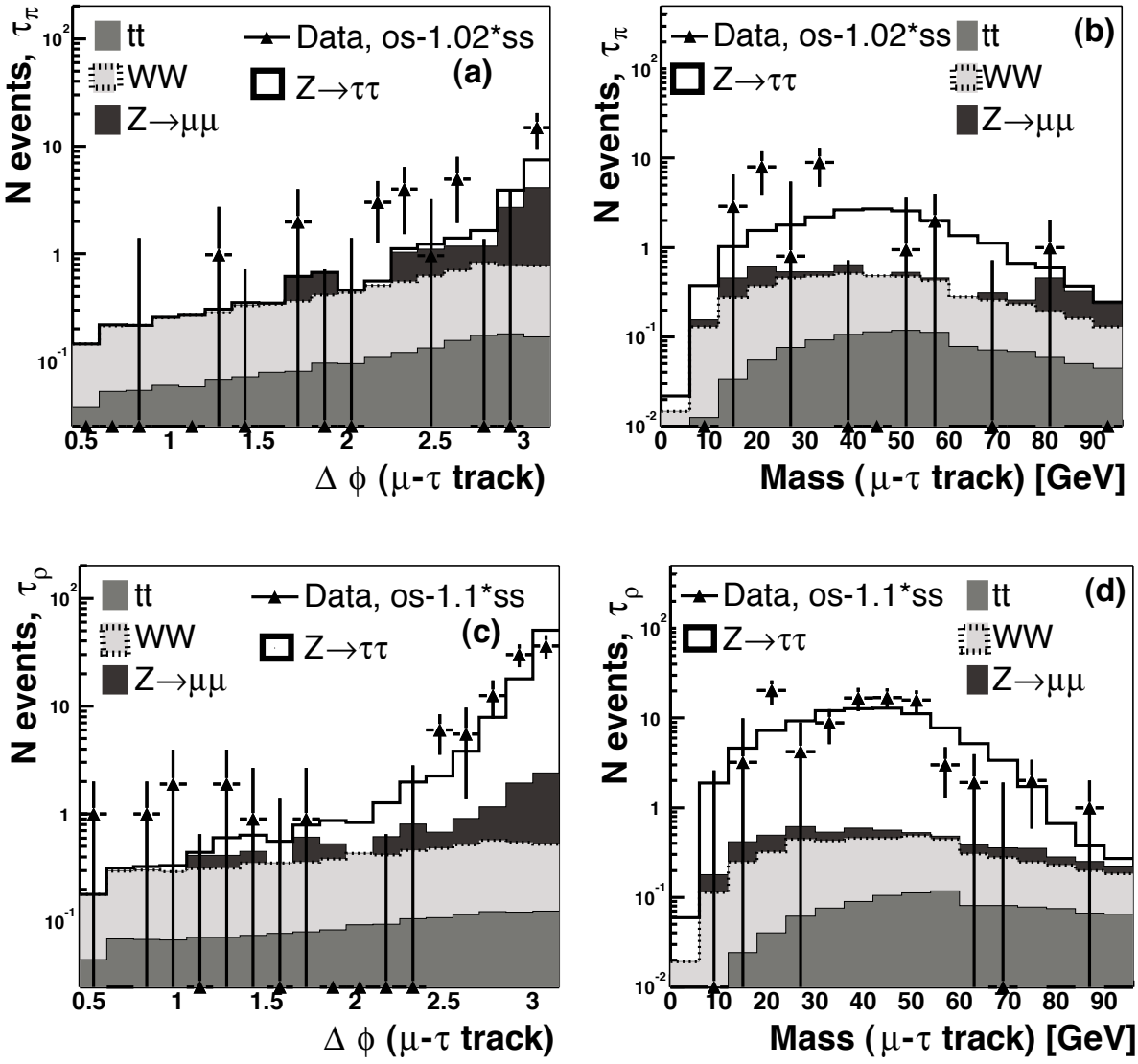

Figure 5.6: (a) $\Delta\phi$ and (b) invariant mass of the muon and tau track for τ_π events in data (triangles), background ($Z^0 \rightarrow \mu^-\mu^+$ in gray, WW as dashed line and $t\bar{t}$ in light grey) and signal MC (black solid line). (c) and (d) show the same distributions for τ_ρ events.

5.5 Cross Section Measurement

The necessary inputs for a cross section measurement are the integrated luminosity $\mathcal{L}$ corresponding to the data sample, the selection efficiency for signal events ϵ_{signal}, the estimated background contribution N_{bkg} and the number of selected events in data N_{sel}. The cross section $\sigma \times BF_{Z^0 \to \tau\tau}$ can then be expressed as:

$$\sigma \times BF_{Z^0 \to \tau\tau} = \frac{N_{sel} - N_{bkg}}{\mathcal{L} * \epsilon_{signal}}, \tag{5.3}$$

where $N_{sel} = N_{ev}^{os} - N_{ev}^{ss} * f_c$, with f_c being the charge correlation factor. The number of selected signal events is hence $N_{ev}^{Signal} \equiv (N_{ev}^{os} - N_{ev}^{ss}) * f_c - N_{bkg}$, where N_{bkg} is the number of expected background events with oppositely charged muon and tau tracks.

5.5.1 Luminosity

The luminosity is determined separately for each reconstruction version. As each luminosity block belongs to a single run, "bad runs" can be taken out of the luminosity calculation. The luminosity is given per trigger as the prescale for each trigger may be different.

Table 5.6 gives the luminosity for the trigger MU_TAU10_L2M0 which was used for this cross section measurement, separated per reconstruction version and given for different data quality requirements. Here, all subsystems were required to be of good quality, leading to a total luminosity of 57.8±5.8 pb^{-1}. An error of 10% is assumed for all integrated luminosity numbers (see section 2.4).

Quality requirement	p13.05	r13.06	p13.06	sum
all	27.36	15.28	37.63	80.27±8.0
Muon	22.76	9.02	37.12	68.90±6.7
Muon+Cal+Tracking	21.39	8.84	36.48	66.71±6.7
Muon+Cal+Tracking+JetMet	17.92	6.94	32.96	57.82±5.8
N_{Run} >= 173352	-	-	17.33	17.33±1.7

Table 5.6: Estimated luminosities in pb^{-1} for the MU_TAU10_L2M0 trigger and the effect of data quality requirements.

5.5.2 Summary of Efficiencies and Backgrounds

The various efficiencies connected to the muon and hadronic tau selection have been discussed in the previous chapter and are summarized in Table 5.7, together with the number of events selected in data. The efficiencies for the muons include the average trigger and tracking inefficiencies.

As explained in section 4.8, the cuts for τ_π events have been optimized from two different viewpoints: first the expected statistical error of the cross section was optimized, as was done for τ_ρ events also. Due to the branching fractions, the signal yield for τ_π events is expected to be

	τ_π	τ_ρ	τ_π signal significance optimized
Muon efficiency	0.207 ± 0.008	0.207 ± 0.008	0.207 ± 0.008
Tau efficiency	$0.041\ ^{+0.006}_{-0.005}$	$0.146^{+0.010}_{-0.006}$	$0.034\ ^{+0.005}_{-0.004}$
L3 track efficiency	$0.80\ ^{+0.05}_{-0.02}$	$0.78\ \pm^{+0.05}_{-0.02}$	$0.80\ ^{+0.05}_{-0.02}$
Muon isolation	0.799 ± 0.009	0.825 ± 0.008	0.799 ± 0.009
electron factor	1.07 ± 0.02	1.32 ± 0.01	1.07 ± 0.02
charge confusion	$1.0\ ^{+0.0}_{-0.012}$	$1.0\ ^{+0.0}_{-0.012}$	$1.0\ ^{+0.0}_{-0.012}$
$\mu\mu$ rejection	0.962 ± 0.004	0.964 ± 0.002	0.962 ± 0.004
ϵ_{signal}	$0.0056^{+0.0007}_{-0.0005}$	$0.025^{+0.003}_{-0.002}$	$0.0046^{+0.0008}_{-0.0006}$
N_{ev} opposite sign	62	153	49
N_{ev} same sign	40	56	24
N_{bkg} events	0.99 ± 0.22	6.06 ± 0.71	0.88 ± 0.08
charge correlation	1.01 ± 0.02	1.10 ± 0.03	1.01 ± 0.02
N_{ev}^{Signal}	20.6 ± 10.2	85.3 ± 14.9	23.9 ± 8.6
BF ($Z^0 \to \tau\bar{\tau} \to \mu\tau_{had}$)	0.225 ± 0.001	0.225 ± 0.001	0.225 ± 0.001
Luminosity [pb^{-1}]	57.8 ± 5.8	57.8 ± 5.8	57.8 ± 5.8
$Z^0 \to \tau\bar{\tau}$ cross section [pb]	$282 \pm 138^{+30}_{-33} \pm 28$	$262 \pm 45^{+23}_{-29} \pm 26$	$399 \pm 142^{+49}_{-53} \pm 40$

Table 5.7: Summary of efficiencies and event yields of the optimized selection. The first error of the cross section measurement is the statistical error, the second the systematic error and the third error is due to the luminosity uncertainty.

lower, thus a second optimization with the aim to achieve the best signal significance was performed for τ_π events. The numbers for these two τ_π selections differ by more than the attributed systematic error and the statistical error is correlated. The main difference between the two selections lies in the isolation cut which changes from 0.2 for the cross section optimization to 0.1 for the selection optimized for the signal significance. The difference of the two cross section numbers is about twice the statistical error. Figure 5.7 shows the distribution of the calorimeter isolation of τ_π candidates for both background subtracted data and MC. The cut positions are indicated by the dashed lines. The number of events with an isolation value between 0.1 and 0.15 shows a downward fluctuation of about 2σ which coincides approximately with the difference of the cross section measured using the two different selections. The remaining bins are compatible with a flat line after the efficiency correction is applied. From this, the conclusion is drawn that the difference of the two cross section measurements in the τ_π channel is due to a statistical fluctuation and not due to a systematic error.

As additional cross check, the number of events after rejecting electron events using the E_T/p_T cut as described in section 5.1 are shown in Table 5.8. For the τ_π case, there are no substantial changes as expected. For the τ_ρ case the cross sections are compatible within the expected precision.

Table 5.9 gives the numbers for the analysis where the selected events are reweighted to account for the muon trigger and track matching efficiencies. In this table, the data sample is

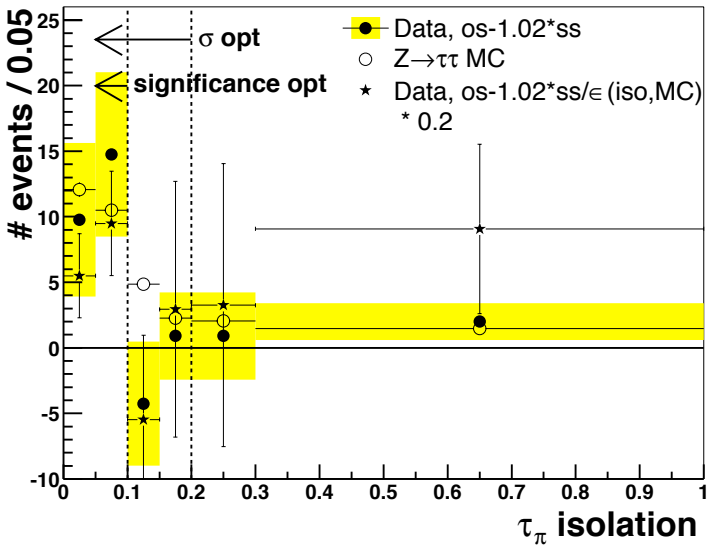

Figure 5.7: The calorimeter isolation of τ_π candidate. The solid dots represent the background subtracted data with the gray area indication the size of the statistical errors and the empty dots show the distributions for $Z^0 \to \tau\overline{\tau}$ MC events. The solid stars indicate the number of data events, corrected for the efficiency expected from MC. The cut positions for both selections are indicated by the dashed lines and arrows.

divided into two sets, before and after run 173352, which is the run where the muon trigger efficiencies at L2 changed. The events are weighted by $1/\epsilon(\eta)$ to take the effect of the muon trigger and track matching efficiency into account that vary with η. The statistical and systematic error due to the muon trigger and track matching efficiency is quoted as second error on the number of events. The last lines give the combined numbers and constitute the final cross section measurement presented in this thesis.

The cross sections obtained using slightly different cuts or techniques are in good agreement with the final number of Table 5.9. The cross section for $Z^0 \to \tau\overline{\tau}$ production in $p\overline{p}$ collisions at 1.96 TeV was measured to be:

$$274 \pm 130 \text{ pb from the } \mu\tau_\pi \text{ channel,}$$

$$273^{+44}_{-46} \text{ pb from the } \mu\tau_\rho \text{ channel.}$$

The most important systematic errors aside from the uncertainty on the luminosity measurement is the systematic effect on the tau selection efficiency which in turn is dominated by the uncertainty of the energy scale. The second large source of uncertainty is the determination of the L3 tracking efficiency. A combination of these numbers results in a measurement of

$$\sigma(p\overline{p} \to Z^0 \to \tau\overline{\tau}) = 273 \pm 38^{+19}_{-24} \pm 27 \text{ pb} \qquad \text{at } \sqrt{s} = 1.96 \text{ TeV},$$

where the systematic errors of the two separate tau type measurements are assumed to be fully correlated.

	π	ρ
Muon efficiency	0.207 ± 0.008	0.207± 0.008
Tau efficiency	$0.041\ ^{+0.006}_{-0.005}$	$0.146^{+0.010}_{-0.006}$
L3 track efficiency	$0.80\ ^{+0.05}_{-0.02}$	$0.78\ ^{+0.05}_{-0.02}$
Muon isolation	0.799 ±0.009	0.825±0.008
electron rejection	0.998 ±0.001	0.932±0.004
electron factor	1.07 ±0.02	1.04 ±0.01
charge confusion	$1.0\ ^{+0.0}_{-0.012}$	$1.0\ ^{+0.0}_{-0.012}$
$\mu\mu$ rejection	0.962 ±0.004	0.964±0.002
ϵ_{signal}	$0.0056^{+0.0009}_{-0.0007}$	$0.018^{+0.002}_{-0.001}$
N_{ev} os	62	126
N_{ev} ss	40	51
N background events	0.99 ±0.22	2.83 ±0.58
charge correlation	1.01 ±0.02	1.10 ±0.03
N_{ev}^{Signal}	20.6 ±10.2	67.1 ±13.3
BF($Z^0 \to \tau\overline{\tau} \to \mu\tau_{had}$)	0.225 ±0.001	0.225±0.001
Luminosity [pb^{-1}]	57.8 ±5.8	57.8 ±5.8
$Z^0 \to \tau\overline{\tau}$ cross section [pb]	$282\ \pm 138^{+30}_{-33} \pm 28$	$286\ \pm 57^{+18}_{-29} \pm 29$

Table 5.8: Summary of efficiencies and event yields of the selection optimized for the cross section measurement, including the electron rejection cut. The first error on the cross section measurement is the statistical error, the second the systematic error and the third component is due to the luminosity uncertainty.

	τ_π	τ_ρ
Muon efficiency	0.279 ± 0.010	0.279± 0.010
Tau efficiency	$0.041\ ^{+0.006}_{-0.005}$	$0.146^{+0.010}_{-0.006}$
L3 track efficiency	$0.80\ ^{+0.05}_{-0.02}$	$0.78\ ^{+0.05}_{-0.02}$
Muon isolation	0.799 ±0.009	0.825±0.008
electron rejection	0.998 ±0.001	0.932±0.004
electron factor	1.07 ±0.02	1.04 ±0.01
charge confusion	$1.0\ ^{+0.0}_{-0.012}$	$1.0\ ^{+0.0}_{-0.012}$
$\mu\mu$ rejection	0.962 ±0.004	0.964±0.002
ϵ_{signal}	$0.0075^{+0.0012}_{-0.0010}$	$0.033^{+0.003}_{-0.002}$
Run # < 173352		
N_{ev} os	72.0 ±8.4±0.7	185.7±13.6±1.8
N_{ev} ss	51.4 ±7.2±0.5	65.1 ±8.1±0.7
N background events	1.12 ±0.12	5.79 ±0.64
charge correlation	1.01 ±0.02	1.10 ±0.03
N_{ev}^{Signal}	19.0 ±11.2	108.3±15.9
BF ($Z^0 \to \tau\overline{\tau} \to \mu\tau_{had}$)	0.225 ±0.001	0.225±0.001
Luminosity [pb^{-1}]	40.4 ±5.0	40.4 ±5.0
cross section [pb]	277 $\pm 163^{+42}_{-43} \pm 28$	$360.0 \pm 52.7^{+25}_{-31} \pm 36$
Run # ≥ 173352		
N_{ev} os	12.7 ±3.6±0.1	25.28±5.0±0.3
N_{ev} ss	4.6 ±2.1±0.0	12.48±3.5±0.1
N background events	0.26 ±0.04	2.48 ±0.35
charge correlation	1.01 ±0.02	1.10 ±0.03
N_{ev}^{Signal}	7.8 ±4.2	9.1 ±6.2
BF ($Z^0 \to \tau\overline{\tau} \to \mu\tau_{had}$)	0.225 ±0.001	0.225±0.001
Luminosity [pb^{-1}]	17.3 ±1.7	17.3 ±1.7
cross section [pb]	266 ±142 ± 37±26.6	70 $\pm 48^{+6}_{-7} \pm 7$
all Runs		
Luminosity [pb^{-1}]	57.8 ±5.8	57.8 ±5.8
cross section [pb]	274 ±121 ± 40±27	273 $\pm 40^{+18}_{-23} \pm 27$

Table 5.9: Summary of efficiencies and event yields of the selection optimized for the cross section measurement. The events have been reweighted to account for the muon trigger and track matching efficiency that depend on η and are divided into two run ranges, separated by a change in the muon trigger. The first error on the number of events is statistical, the second is the systematic error due to the uncertainty on the muon trigger and track matching efficiency. The first error on the cross section measurement is the statistical error, the second the systematic error and the third error is due to the luminosity uncertainty.

5.6 Comparison to the SM and the $Z^0 \to \mu^-\mu^+$ and $Z^0 \to e^-e^+$ channels

The measurement of $\sigma(Z^0) \times BF(Z^0 \to \tau\bar{\tau})$ in the two final state $\mu\pi$ and $\mu\rho$ has been described in the sections above. Lepton universality states that the couplings of electroweak bosons to leptons is independent of the lepton flavor. This feature of the SM has been tested to great precision at LEP and the Tevatron, hence the presented measurement of the Z^0 cross section using the decay into tau leptons presented here can directly be compared to the preliminary results of the cross section of the Z^0-boson into electrons [106] and muons [99] presented at the Lepton Photon conference at Fermilab in August 2003. Figure 5.8 shows these numbers and their errors. The inner error bars show the measurement and its combined statistical and

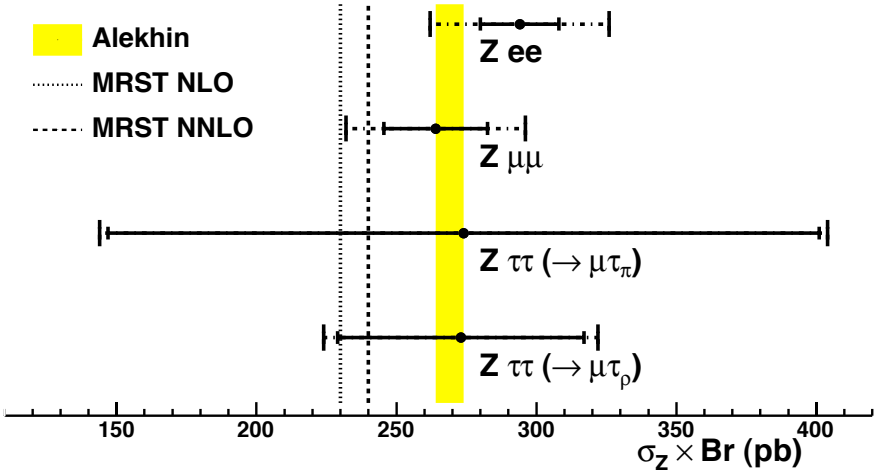

Figure 5.8: The Z^0 cross section at $\sqrt{s}$=1.96 TeV, DØ preliminary results only.

systematic error, the outer error bars indicate the additional uncertainty due to the luminosity uncertainty. This error is correlated between all the measurements. The light gray band indicates the SM prediction for the Z^0 cross section from Alekhin [107], the dashed and dotted lines are the predictions from MRST [108].

As a test for lepton universality, the ratio of the $Z^0 \to \tau\bar{\tau}$ and $Z^0 \to e^-e^+$ and $Z^0 \to \mu^-\mu^+$ cross section is calculated:

$$\frac{\sigma(p\bar{p} \to Z^0 \to \tau\tau)}{\sigma(p\bar{p} \to Z^0 \to ee)} = 0.93 \pm 0.16, \tag{5.4}$$

$$\frac{\sigma(p\bar{p} \to Z^0 \to \tau\tau)}{\sigma(p\bar{p} \to Z^0 \to \mu\mu)} = 1.03 \pm 0.18. \tag{5.5}$$

For this ratio, the luminosity error and Z^0 production cross section are fully correlated and thus divides out. The statistical and systematic errors of the cross section measurements in the three channels are assumed to be uncorrelated. These results are compatible within errors with the

LEP measurement of

$$\frac{\sigma(Z^0 \to \tau\tau)}{\sigma(Z^0 \to ee)} = 1.002 \pm 0.003, \tag{5.6}$$

$$\frac{\sigma(Z^0 \to \tau\tau)}{\sigma(Z^0 \to \mu\mu)} = 1.001 \pm 0.003. \tag{5.7}$$

from reference [34].

The results for the cross section measurements of Z^0 and W-boson production at hadron colliders as a function of the center-of-mass energy is shown in Fig.5.9. This figure contains

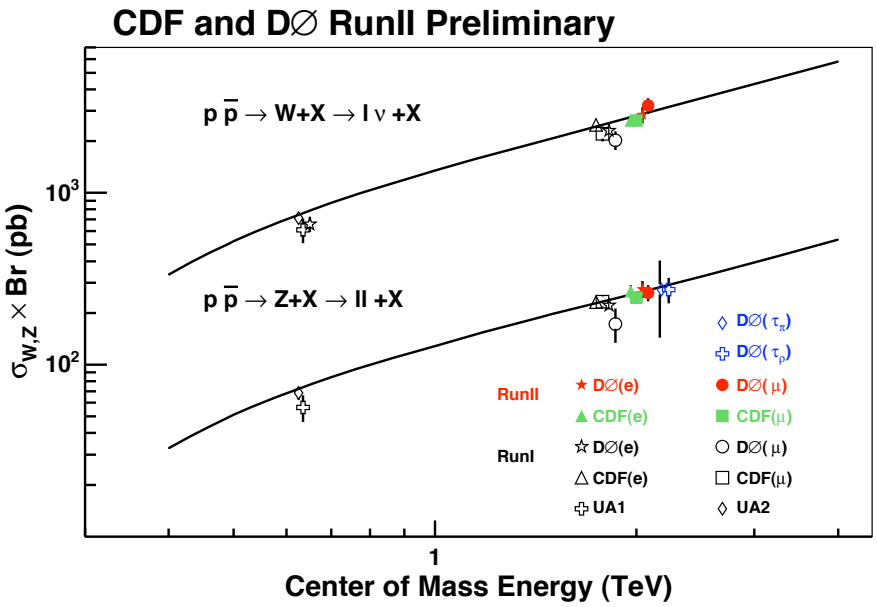

Figure 5.9: The Z^0 and W cross sections as measured in hadron colliders as a function of $\sqrt{s}$. The points are the measurements at 1.96 TeV are drawn at slightly different energies for clarity of presentation.

published results from UA1 and UA2 as well as measurements from DØ and CDF from Run I. The Run II results from the two Tevatron experiments are preliminary. The measurement presented in this thesis is added for comparison and the results are compatible within errors to the other measurements and the trend indicated by the line.

5.7 Conclusion and Outlook

The cross section of $Z^0 \to \tau\bar{\tau}$ in $p\bar{p}$ collisions has been measured to be $273 \pm 38^{+19}_{-23} \pm 23$ pb. The uncertainty in this result is dominated by the statistical error, so the future higher integrated luminosity will reduce this error significantly.

In addition, also the systematic error will improve from higher available statistics. For this analysis, the energy scale of hadronic taus was one of the large sources of systematic uncertainty as the value was taken from Monte Carlo simulation leading to a large systematic uncertainty.

More data will allow to measure the energy scale from data using the momentum measurement of the central tracks compared to the energy measurement of the calorimeter. The measurement of the L3 track trigger efficiency will also improve with a larger sample of Z^0 bosons and also by adding a clean sample of $\Upsilon \to \mu\mu$ events.
The higher tracking efficiency of more recent reconstruction versions than used in this thesis will not only increase the reconstruction efficiency for both the muon and the hadronic tau, but also make the track isolation a more powerful selection variable. Also the measurement using "three prong" tau decays will become feasible with improved two-track resolution and tracking efficiency.

Other improvements will be the addition of channels such as $Z^0 \to \tau\bar{\tau} \to e\nu_\tau\bar{\nu}_e\tau_{had}\nu_\tau$ or the fully hadronic channel. The latter will become a possibility with the use of the recently installed track trigger terms at L1. The analysis will improve by using multi-variate methods like Neural Nets (NN) for tau identification instead of the approach using simple cuts which has been chosen here. Neural Nets are especially powerful when two samples (as tau leptons and QCD jets here) are separated by many correlated variables. For this thesis, it was explicitly chosen to use a "simple cut" approach as the experiment is in the process of understanding the responses of all sub-detectors. In a "simple cut" analysis, the influence of every single input variable and its systematic errors can be evaluated in a straightforward way. An analysis employing a Neural Network or any other multi-variate technique should reproduce and hopefully improve the result of the more straightforward approach taken here.

This first measurement using tau leptons at DØ in Run II is also the "proof of principle" that it is possible to do physics with tau leptons at DØ. There are many topics, notably in searches for the Higgs and "Physics Beyond the Standard Model" where tau leptons play an important role (see section 1.4.2). The way is now open to pursue these tau analyses in DØ at the Tevatron, the current energy frontier.

Bibliography

[1] WMAP Collaboration. First Year Wilkinson Microwave Anisotropy Probe (WMAP) Observations: Determination of Cosmological Parameters. http://arXiv.org/abs/astro-ph/0302209, February 2003.

[2] S. Perlmutter and B. P. Schmidt. Measuring Cosmology with Supernovae. http://arXiv.org/abs/astro-ph/0303428, March 2003.

[3] M. L. Perl *et al.* Evidence for anomalous lepton production in e^+e^- annihilation. *Phys. Rev. Lett.*, 35:1489, 1975.

[4] F. Abe *et al.* Observation of Top Quark Production in p anti-p Collisions with the Collider Detector at Fermilab. *Phys. Rev. Lett.*, (74):2626, 1995.

[5] S. Abachi *et al.* Observation of the Top Quark. *Phys. Rev. Lett.*, (74):2632, 1995.

[6] K. Kodama *et al.* Observation of Tau Neutrino Interactions. *Phys. Lett.*, B(504):218–224, 2001.

[7] S. L. Glashow. Partial Symmetries of Weak Interactions. *Nucl. Phys.*, 22:579–588, 1961.

[8] A. Salam. in Elementary Particle Theory. ed. N. Svartholm, 1961.

[9] S. Weinberg. A Model of Leptons. *Phys. Rev. Lett.*, 16:1264–1266, 1967.

[10] M. Veltman. Perturbation Theory of Massive Yang-Mills fields. *Nucl. Phys.*, B(35):637–650, 1968.

[11] G. 't Hooft. Renormalizable Lagrangians for Massive Yang-Mills Fields. *Nucl. Phys.*, B(35):167–188, 1971.

[12] G. 't Hooft and M. Veltman. Combinatorics of Gauge Fields. *Nucl. Phys.*, B(50):318–353, 1972.

[13] UA1 collaboration. Experimental Observation of Isolated Large Transverse Energy Electrons with Associated Missing Energy at $\sqrt{s} = 540$ GeV. *Phys. Lett.*, B122(1):103, 1983.

[14] UA1 collaboration. Experimental observation of Lepton pairs of Invariant Mass Around 95 GeV/c^2 at the CERN SPS Collider. *Phys. Lett.*, B(216):398–410, 1983.

[15] UA2 collaboration. Observation of Single Isolated Electrons Of High Transverse Momentum in Events wit Missing Transverse Energy at the CERN $p\bar{p}$ Collider. *Phys. Lett.*, B122(5-6):476, 1983.

[16] UA2 collaboration. Evidence for $Z^0 \rightarrow e^- e^+$ at the CERN anti-p p Collider. *Phys. Lett.*, B122:130–140, 1983.

[17] P. W. Higgs. Broken Symmetries, Massless Particles and Gauge Fields. *Phys. Lett.*, 12:132–133, 1964.

[18] F. Englert and R. Brout. Broken Symmetry and the Mass of Gauge Boson Vectors. *Phys. Rev. Lett.*, 13:321–322, 1964.

[19] M. Gell-Mann. A Schematic Model of Baryons and Mesons. *Phys. Lett.*, 8:214, 1964.

[20] G. Zweig. An SU(3) Model for Strong Interaction Symmetry and its Breaking I. CERN-8182-TH-401, 1964.

[21] G. Zweig. An SU(3) Model for Strong Interaction Symmetry and its Breaking II. CERN-8419-TH-412, 1964.

[22] R. P. Feynman. In C. N. Yang *et al*, editor, *High Energy Collisions, Proceedings of the Third International Conference, Stony Brook, New York*, 1969.

[23] H. Fritzsch, M. Gell-Mann, and H. Leutwyles. Phys. Lett., 1973.

[24] D. J. Gross and F. Wilczek. Phys. Rev. Lett., 1973.

[25] H. D. Politzer. Phys. Rev. Lett., 1973.

[26] S.Weinberg. Phys. Rev. Lett., 1973.

[27] G. Altarelli and G. Parisi. Asymptotic Freedom in Parton Language. *Nucl. Phys.*, 126:297, 1977.

[28] V. N. Gribov and L. N. Lipatov. Deep Inelastic ep Scattering in Perturbation Theory. *Sov. J. Nucl. Phys.*, 15:438–450, 1972.

[29] Yu. L. Dokshitzer. Calculation of the Stucture Functions for Deep Inelastic Scattering and e^+e^- Annihilation by Perturbation Theory in Quantum Chromodynamics. *Sov. Phys. JETP*, 46:641, 1977.

[30] U. Baur *et al*. Report of the Working Group on Photon and Weak Boson Production. hep-ph/0005226.

[31] N. Tuning. *Proton structure functions at HERA*. PhD thesis, University of Amsterdam, 2001.

[32] J. Pumplin, D. R. Stump, J. Huston, H. L. Lai, P. Nadolsky, and W. K. Tung. New Generation of Parton Distributions with Uncertainties from Global QCD Analysis. hep-ph/0201195, January 2002.

[33] R. S. Thorne, A. D. Martin, R. G. Roberts, and W. J. Stirling. Update of MRST Parton Distributions. hep-ph/0207067, July 2002.

[34] The LEP Collaborations ALEPH, DELPHI, L3, OPAL and the LEP Electroweak Working Group, the SLD Electroweak and Heavy Flavour Groups. A Combination of Preliminary Electroaek Measurements and Constraints on the Standard Model. hex.ex/0312023.

[35] The LEP Electroweak Working Group. A Combination of Preliminary Electroweak Measurements and Constraints on the Standard Model. hep-ex/0212036, December 2002.

[36] The LEP Working Group for Higgs Boson Search. Search for the Standard Model Higgs Boson at LEP, 2002.

[37] M. Carena *et al*. Report of the Tevatron Higgs Working Group. hep-ph/0010338.

[38] J. Ellis. Suspersymmetry for Alp Hikers. In N. Ellis and J. March-Russel, editors, *2001 European School of High Energy Physics*, volume 002 of *Yellow Report*, pages 157–204. CERN, 2002.

[39] SUGRA Working Group Collaboration (S. Abel et al.). Report of the Sugra Working Group for Run II of the Tevatron. hep-ph/0003154, March 2000.

[40] SUSY Working Group Collaboration (Ray Culbertson et al.). Low Scale and Gauge Mediated Supersymmetry Breaking at the Fermilab Tevatron Run II. hep-ph/0008070, August 2000.

[41] H. P. Niles. *Phys. Rept.*, (110), 1984.

[42] H. Baer, T. Krupovnickas, and X. Tata. Reach of the Fermilab Tevatron for minimal supergravity in the region of large scalar masses. *JHEP*, 0307(020), 2003.

[43] K. W. Edwards *et al*. Search for Baryons in the Radiative Penguin Decay b $\rightarrow$ s gamma. hep-ex/0305005, submitted to Phys. Rev. D, Rapid Communication, May 2003.

[44] J. Marriner. Stochastic Cooling Overview. Fermilab_CONF-03-158, August 2003.

[45] F. Lehner. The Phenomenology of the Micro Discharge Effects on DØ Silicon Modules. DØ note 3804.

[46] S. N. Ahmed *et al.* DØ SMT Radiation Protection System. DØ note 3915, October 2001.

[47] S. N. Ahmed *et al.* DØ SMT Radiation Monitoring System. DØ note 4022, September 2002.

[48] MVME2600 Series VME Processor Modules data sheet. http://mcg.motorola.com/us/ds/pdf/ds0003.pdf.

[49] VxWorks real time operating system. http://www.windriver.com/products/vxworks5/index.html.

[50] Experimental Physics and Industrial Control System. http://www.aps.anl.gov/epics/.

[51] B. Warnaar. Work on the Radiation Monitoring at DØ. DØ note 3941, February 2002.

[52] D. Adams *et al.* The DØ Upgrade: Central Fiber Tracker, Technical Design Report. DØ note 4164, June 2003.

[53] D. Lincoln (for the SciFi Detector Group). A large statistics study of the performance and yields of generation-6 VLPCs (HISTE-VI). In *Conference proceedings for Como 98*.

[54] M. Adams *et al.* Design Report of the Central Preshower Detector for the DØ Upgrade, 1996. DØ note 3014.

[55] M. Bhattachargee *et al.* Technical Design Report of the Forward Preshower Detector for the DØ Upgrade, 1998. DØ note 3445.

[56] P. Baringer *et al.* Cosmic ray data analysis for the DØ preshower detector. D0 note 3765, July 2000.

[57] L. Groer. DØ Calorimeter Upgrades for Tevatron Run II. Frascati Physics, 2000.

[58] Calorimeter Electronics Upgrade TDR. http://www-d0.fnal.gov/hardware/cal/intro/tdr/tdrformat.htm.

[59] R. Zitoun. Study of the non linearity of the DØ calorimeter readount chain, July 2002. DØ note 3997.

[60] L. Sawyer *et al.* Technical Design Report for the Upgrade of the ICD for DØ Run 2. DØ note 2686, June 1997.

[61] D. Denisov *et al.* A Comparison of the Magnetic Field Programs TOSCA and GFUND3D for the Run II DØ Detector Magnet System, 2001. DØ note 3874.

[62] J. Hauptman *et al.*

[63] M. Begel *et al.* Luminosity and Performance of DØ during the First Year of Run 2. DØ note 3973.

[64] D. Edmunds *et al.* Level 1 Trigger OR's with Pseudo AND/OR Terms. DØ note 3683, September 1999.

[65] CTT Design Group. Technical Design Report for the Upgrade L1/L2 Tracking Trigger - TDR for the CTT. DØ note 3551, November 1998.

[66] R. Hirosky. In *Proceedings of the 11th IEEE Real Time Conference 99*, Santa Fe, New Mexico, 14-18 June 1999, 1999.

[67] T. Christiansen. The DØ L2-Muon Trigger Performance in P11, 2002. DØ note 4053.

[68] M. Adams *et al.* Level 2 Calorimeter Preprocessor Technical Design Report. DØ note 3651, May 1999.

[69] Y. Codou. The Level 3 Tau Tool. DØ Note 4132, May 2003.

[70] D. Whiteson. Global Track Finding at Level 3. DØ note 3808, December 2000. 3808.

[71] M. Begel . DØ Luminosity in RunII: Recorded. DØ note 3972.

[72] C. Miao *for the DØ Collaboration.* The DØ Run II Luminosity Monitor. DØ note 3573.

[73] T. Sjöstrand and L. Lönnbald. Pythia 6.2. LU PT 01-21 [hep-ph/0108264], 2001.

[74] G. Corcella *et al.* Herwig 6.5. JHEP 0101 (2001) 01 [hep-hp/0011363].

[75] S. Jadach *et al.* TAUOLA Library: Version 2.5. *Comp. Phys. Comm.*, (76):361, 1993.

[76] D. Adams. Finding Tracks. DØ Note 2958, 1998.

[77] A. Khanov. HTF: histogramming method for finding tracks. The algorithm description. DØ Note 3778, 2000.

[78] A. Schwartzman and M. Narain. Primary Vertex Selection. DØ Note 3907, 2001.

[79] B. Olivier *et al*. NADA, A New Event by Event Hot Cell Killer. DØ note 3687, 2000.

[80] D. E. Soper S. D. Ellis. Successive Combination Jet Algorithm for Hadron Collisions. *Phys. Rev.*, D(48):3160, 1993.

[81] Yu. L. Dokschitzer S. Catani and B. R. Webber. The k_T Clustering Algorithm for Jets in Deep Inelastig Scattering and Hadron Colliders. *Phys. Rev.*, D(48):291, 1992.

[82] M. H. Seymour S. Catani, Yu. L. Dokschitzer and B. R. Webber. Longitudinal Invariant k_T Clustering Algorithm for Hadron-Hadron Collisions. *Phys. Rev.*, B(406):187, 1993.

[83] D. Soper *et al*. Recommendation from Les Houches 1999 Jet Definition Group. Letter to J. Blazey; http://niuhep.pyscis.niu.edu/ blazey/jet_alg/les_houches.ps.

[84] S. Protopopecu. EMReco Algorithms. http://www-d0.fnal.gov/d0dist/dist/releases/current/emreco/doc/EMReco.ps.

[85] L. Duflot and M. Ridel. The CellNN algorithm: cell level clustering in the D0 calorimeter. DØ note 3923, 2001.

[86] F. Beaudette and J.-F. Grivaz. The Road Method (an algorithm for the identification of electrons in jets). DØ note 3976, 2002.

[87] R. Raja. H-matrix Analysis for top→lepton+jets. DØ note 1192, 1992.

[88] M. Narain. Electron Identification in the DØ Detector, 1992.

[89] D. Whiteson. Muon Tracking in the Calorimeter. DØ Note 3996, 2002.

[90] Muon ID Group. Muon ID version 2.0, 2002.

[91] K. Hagiwara *et al.*. The Review of Particle Physics. *Physical Review*, D(66), 2002.

[92] B. Abbot *et al.* Determination of the absolute jet energy scale in the DØ calorimeters. *Nucl. Instr. Meth.*, A424:352–394, 1999.

[93] F. Canelli *et al.* Jet Energy Scale at DØ in Run II. DØ note 4110, 2002.

[94] M. Pettini. *Measuring the Jet Response and the Search for the Higgs Boson in the Channel ZH*$\rightarrow e^+e^-b\bar{b}$. PhD thesis, Imperial College London, 2003.

[95] V. M. Abazov H. T. Diehl and R. McCroskey. Good and Bad Muon Global Runs Early in Run II. DØ note 3938, 2002.

[96] Jet/Met ID-group. Run Selection version 3.0. http://www-d0.fnal.gov/ d0upgrad/d0_private/software/jetid/jetid-certif.html, 2003.

[97] M. Agelou *et al.* Measurement of the Inclusive W to mu nu Cross-Section in p pbar Collisions at $\sqrt{s}$=1.96 TeV. DØ note 4128, 2003.

[98] R. J. Hooper, G. Landsberg. Search for Heavy Resonances in the Di-Muon Channel With 100 pb^{-1} of Run II Data. DØ note 4229, 2003.

[99] E. Nurse and P. Telford. Measurement of cross-section times branching ratio for $Z\rightarrow \mu\mu$ in ppbar collisions at 1.96 TeV. DØ note 4114, 2003.

[100] S. Drell and T. M. Yan. *Phys. Rev. Lett.*, 25:316, 1970.

[101] EM id group. EM-ID certification results. http://www-d0.fnal.gov/phys_id/emid/d0_private/certification/main_v4_1.html.

[102] D. Chakraborty, Y. Coadou, S. Duensing, C. Galea, Y. Gershtein, A-C. LeBihan, C. Noeding, and S. Protopopescu. Reconstruction of Tau Leptons in Hadronic Final States at D0 in Run 2. DØ note 4210, 2003.

[103] D. Whiteson and M. Kado. Muon Isolation Studies. DØ Note 4070, 2002.

[104] J. M. Campbell and R. K. Ellis. An update on vector boson pair production at hadron colliders. *hep-ph/9905386*, 1999.

[105] M. Cacciari, S. Frixione, M. L. Mangano, P. Nason, and G. Ridolfi. The $t\bar{t}$ Cross-section at 1.8 and 1.96 TeV: a Study of the Systematics Due to Parton Densities and Scale Dependence. *hep-ph/0303085*, 2003.

[106] D. Alton, H. Fox, J. Gardner, S. Mattingly, G. Steinbrück, J. Torborg, M. Verzocchi, and J. Zhu. Measurement of $Z^0\rightarrow e^+e^-$ and $W\rightarrow e^{\pm}\nu$ Production Cross Sections at the Tevatron With the DZero Detector. DØ note 4131, 2003.

[107] S. I. Alekhin. The NNLO predictions for the rates of the WZ^0 productions in $p\bar{p}$ collisions. hep-ph/0307219, July 2003.

[108] R. S. Thorne. Global Fits of Parton Distributions. hep-ph/0211113, November 2002.

Summary

In this thesis the first measurement of $\sigma(p\bar{p} \rightarrow Z^0 \rightarrow \tau\bar{\tau})$ with the DØ detector at the Tevatron is presented. The tau pair candidates are recorded by the DØ detector using $p\bar{p}$ interactions at a center-of-mass energy of 1.96 TeV.
Events in which one tau decays into a muon and the other tau final state is hadronic with one charged particle are selected for this analysis. The selection criteria for the hadronic tau decay are based on the tau final state, hence for two channels of one-prong taus: single charged pion (τ_π) and rho decays (τ_ρ). The selection is based on simple cuts on a number of discriminating variables and the cut values have been optimized for the best cross section measurement. Of hadronic tau candidates that have been reconstructed as τ_π candidates, $0.801 \pm 0.017 \pm 0.066$ pass the selection cut; in the case of τ_ρ taus, the selection efficiency is $0.676 \pm 0.009 \pm 0.009$. Of all QCD jets that are reconstructed as hadronic tau candidates, 0.0093 ± 0.0002 pass the τ_π selection cuts and 0.0122 ± 0.0002 the τ_ρ cuts.

The cross section has been measured to be $274 \pm 121 \pm 40 \pm 27$ pb in the $\mu\tau_\pi$ channel and $273 \pm 40^{+18}_{-23} \pm 27$ pb in the $\mu\tau_\rho$ channel, resulting in a combined measurement of
$\sigma(p\bar{p} \rightarrow Z^0 \rightarrow \tau\bar{\tau}) = 273 \pm 38^{+19}_{-23} \pm 27$ pb which agrees with the SM prediction within errors. The errors are dominated by the statistical error as only the first data taken with the DØ detector in Run II was used. Due to the small set of tau candidates, the calorimeter energy scale could not yet be determined using data and this uncertainty is the largest systematic effect on the measurement. Another large contribution arises from the uncertainty of 10% on the luminosity measurement. This is expected to decrease significantly in the future.

It was demonstrated that the currently available tools are sufficient to use tau leptons in the measurement of a SM process. This opens the door to the use of hadronic tau decays in the search for new particles, like SUSY particles, that decay preferentially to tau leptons in a number of models or the Higgs boson of either the SM or extended model. Doing physics at the Tevatron as the accelerator at the current energy frontier is our current best hope to find the yet elusive Higgs boson and will allow to either find proof of physics beyond the Standard Model or tighten the constraints on these models.

Samenvatting

Dit proefschrift presenteert de eerste meting van $\sigma(p\bar{p} \rightarrow Z^0 \rightarrow \tau\bar{\tau})$ met de DØ detector bij de Tevatron botser. De tau paren worden geregistreerd door de DØ detector in $p\bar{p}$ interacties bij een zwaartepuntsenergie van 1.96 TeV.

Gevallen waarbij een tau in een muon vervalt en de andere tau in een hadronische eindtoestand worden voor deze analyse geselecteerd. De selectiecriteria voor het hadronisch tau verval zijn gebaseerd op de eindtoestand. De twee hierbij beschouwde vervalskanalen zijn: tau vervallen in één geladen spoor (τ_π) en vervallen in een ρ-meson (τ_ρ). De selectie bestaat uit een aantal snedes op variabelen die een onderscheid maken tussen de genoemde tau vervallen en de achtergrond. De snedes zijn geoptimaliseerd voor de best mogelijke meting van de werkzame doorsnede. Van de hadronische tau vervallen die als τ_π zijn gereconstrueerd passeren $0.801 \pm 0.017 \pm 0.066$ de selectiesnedes. In het geval van τ_ρ is de selectieefficiëntie $0.676 \pm 0.009 \pm 0.009$. Van alle QCD jets die als hadronische tau kandidaat zijn gereconstrueerd overleven 0.0093 ± 0.0002 de τ_π snedes en 0.0122 ± 0.0002 de τ_ρ snedes.

De werkzame doorsnede van Z bosonen maal de vertakkingsverhouding van het Z verval in tau-leptonen is gemeten als $274 \pm 121 \pm 40 \pm 27$ pb in het $\mu\tau_\pi$ kanaal en $273 \pm 40^{+18}_{-23} \pm 27$ pb in het $\mu\tau_\rho$ kanaal. Het gecombineerde resultaat wordt daarmee $\sigma(p\bar{p} \rightarrow Z^0 \rightarrow \tau\bar{\tau}) = 273 \pm 38^{+19}_{-24} \pm 27$ pb. Dit komt overeen met de voorspellingen van het Standaard Model binnen de meetfouten. De meetfouten worden gedomineerd door de statistische onzekerheid, omdat alleen de eerste data zijn gebruikt die DØ in Run II van het Tevatron heeft genomen. Door de geringe hoeveelheid geselecteerde kandidaten was het onmogelijk een calorimeter energieijking vast te stellen met de data en de resulterende onzekerheid is de grootste systematische onzekerheid van de meting. Een andere grote bijdrage aan de systematische onzekerheid wordt door de meting van de luminositeit veroorzaakt, die maar tot op 10% nauwkeurig is. In de toekomst zullen deze systematische fouten drastisch afnemen.

Dit proefschrift demonstreert dat de huidig beschikbare methoden voldoende zijn om tau leptonen te detecteren en de metingen in termen van het Standaard Model te begrijpen. Dit opent de deur naar het gebruik van tau leptonen als middel in de zoektocht naar nieuwe deeltjes, zoals die bijvoorbeeld door supersymmetrische theorieën worden voorspeld. Ook kan het nog ontbrekende Standaard Model deeltje, het Higgs boson, door zijn verval in tau's mogelijk worden gevonden. Het Tevatron biedt op dit moment als hoogste energie deeltjesversneller de beste kansen om het Higgs boson te vinden of nieuwe fysica te ontdekken buiten het Standaard Model. De identificatie van tau's kan hierbij een belangrijke rol spelen.

Curriculum

Silke Duensing was born on October 4th, 1973 in Bremen. After her “Abitur” in 1993 she started to study physics in Bremen. In 1995 she switched to the Humboldt Universität zu Berlin, where she graduated in 1998 with a Diplomarbeit titled ”Measurement of the Triple Gauge Boson couplings in hadronic Wpair decays” in elementary particle physics. Next to her studies, Silke was part of the organizing committee of the first “Deutsche Physikerinnen Tagung” which took place in Berlin in 1998. She presented the results of her undergraduate work at the “Tagung der Deutschen Physikalischen Gesellschaft” in Freiburg, 1997 as well as at the “Deutsche Physikerinnen Tagung” 1998 in Hamburg.

After the completion of her undergraduate studies, she started as junior researcher at the University of Nijmegen. At the start of her contract she worked on the Silicon Diode Radiation Monitoring System of the DØ detector, which she presented at the “Tagung der Deutschen Physikalischen Gesellschaft” in Heidelberg, 1998. In the course of this work, she spent 20 months at Fermilab, close to Chicago, from April 1999 to December 2000 and returned there for a few months the following summers. During the years as a graduate student, Silke participated in a number of summer schools such as the Joint Dutch-Belgium-German summer schools in Rolduc in 1999 and Monschau 2000 as well as the CERN summer school in Beatenberg in 2001. She presented her work on tau identification at the NNV meeting in 2001 and the APS meeting in 2001 in Albuquerque. In addition she presented results of the DØ collaboration at the SUSY conference in 2003 in Tucson.
In 2001 and 2002, Silke gave tutorials for courses in elementary particle physics and quantum mechanics.

Acknowledgment

First of all I would like to thank my advisor Sijbrand de Jong for offering me his (and Nijmegen's) first DØ aio position. It has been great to work together and watch our experiment progress from building detectors to taking data and performing physics analysis. I must also thank him for reading even the very first versions of this thesis and helping me turn it into something one could give to a commission.
My analysis was greatly improved through collaboration with many of my colleagues. I want to mention the members of the DØ tau-id and WZ groups in particular for their help and discussions.
I cannot forget to thank Marjo and Annelies for helping me with many organizational issues including the arrangement of my accommodations in the Netherlands. Also I want to mention the people who made living and working in the Netherlands less solitary: Henric, Jaap, Axel, Bram, Tim, Vanessa, Cristina and Freya to mention only a few.

I am grateful to have a family that did not get sick of having me visit them, or at least did not let me know they did, and who were always encouraging for me to do what I wanted to do. Finally, of course, I cannot express how lucky I feel to have found Tim. Thank you for being with me during this time, for trying to keep me sane and for reminding me that I am a person and not just a physicist.